SIMULATION OF UPGRADED ATLAS RPC DETECTOR: BIS7/8 GEOMETRY IMPLEMENTATION

by

Havva Hasret Nur

B.S., Physics, Boğaziçi University, 2017

Submitted to the Institute for Graduate Studies in
Science and Engineering in partial fulfillment of
the requirements for the degree of
Master of Science

Graduate Program in Physics

Boğaziçi University

2020

ACKNOWLEDGEMENTS

I would like to thank my advisor for introducing me to this project and his support. I would like to thank my colleague Prof. Matteo Negrini for his insight, immensely deep knowledge and his support. Without him, this thesis would not be complete. I would like to give my greatest appreciation to my father, my mother and my sister for always holding my back. Without them, I would not be able to become who I am right now. I would like to thank Cihan Pazarbaşı for being my once in a life time, making my heart smile and for highlighting my life. I would like to thank my friends Melike Bilgin, Emre Çelebi, Alişan Karababa and Ekin Opar for always standing by me.

ABSTRACT

SIMULATION OF UPGRADED ATLAS RPC DETECTOR: BIS7/8 GEOMETRY IMPLEMENTATION

In this thesis, the new geometry for RPC detector planned for ATLAS HL-LHC Upgrade is implemented in AMDB and uploaded to the ATLAS Oracle Database in order to form the full ATLAS simulation. The simulation results have been investigated in terms of compatibility to the expectations of new geometry and physics performance. This study shows that the new geometry satisfies the expectation and physics performance.

ÖZET

YÜKSELTİLMİŞ ATLAS RPC DETEKTÖRLERİNİN SİMULASYONU: BIS7/8 GEOMETRİ İMPLEMENTASYONU

Bu tezde, ATLAS HL-LHC Yükseltilmesi için planlanan yeni geometri AMDB'de implement edildi ve ATLAS veritabanına yüklendi. Tam simülasyon oluşturuldu. Bu simülasyon fizik performansı ve yeni geometriden beklentilerimizle uyumluluğu açısından incelendi. Sonuçlar yeni geometrinin öngörülermizle uyumlu olduğu ve beklenen fizik performansını karşıladığı görüldü.

TABLE OF CONTENTS

ACKNOWLEDGEMENTS . . . iii
ABSTRACT . . . iv
ÖZET . . . v
LIST OF FIGURES . . . ix
LIST OF TABLES . . . xvi
LIST OF SYMBOLS . . . xviii
LIST OF ACRONYMS/ABBREVIATIONS . . . xix
1. INTRODUCTION . . . 1
2. THEORY . . . 3
2.1. Ionization Detectors . . . 3
2.2. Gaseous Ionization Detectors . . . 3
2.3. Gaseous Ionization Detectors . . . 4
2.4. GEANT4 . . . 6
2.4.1. How Geant Works . . . 7
2.5. Simulation of Toy Model RPC . . . 12
2.5.1. Bethe Formula . . . 12
2.5.2. Landau Distribution . . . 14
3. ATLAS . . . 16
3.1. ATLAS (A Troidal LHC ApparatuS) Experiment . . . 16
3.1.1. ATLAS Coordinate System . . . 17
3.1.2. Inner Detector . . . 17
3.1.3. Calorimeter . . . 20
3.1.4. Muon Spectrometer . . . 20
3.1.4.1. The Resistive Plate Chambers (RPC) of the ATLAS experiment . . . 22
3.1.5. ATLAS Trigger System . . . 23
3.1.5.1. Muon Trigger . . . 24
4. UPGRADE OF ATLAS FOR HL-LHC . . . 26

4.1. ATLAS Upgrade Plans . . . 26
4.1.1. Upgrades in the Muon Spectrometer . . . 27
4.1.2. BI RPC Upgrade . . . 28
4.1.3. Peformance and Physics . . . 30
4.1.3.1. Muon Reconstruction Performance . . . 30
5. PERFORMANCE STUDIES IN HL-LHC . . . 32
5.1. Reconstruction Efficiency at HL-LHC . . . 32
6. BI RPC PERFORMANCE STUDIES . . . 37
6.1. RPC Trigger Efficiency . . . 37
6.1.1. Performance Dependence on Pile-up . . . 39
7. BIS78: UPGRADED ATLAS MS SIMULATION . . . 41
7.1. BIS78 Geometry Implementation . . . 41
7.2. PERSINT . . . 41
7.3. AMDB . . . 44
7.3.1. The Axis System in AMDB . . . 44
7.3.2. Creating the Stations . . . 46
7.3.3. Cutout Description . . . 47
7.3.4. Grand Global Positioning . . . 47
7.3.5. Inner Structure Description . . . 49
7.4. New Geometry Design in AMDB . . . 49
7.5. Forming the Stations . . . 52
7.6. Forming Relative Positions of the Objects in One Station . . . 54
7.7. Global Positioning of the Chamber . . . 54
7.8. Basic Shapes in the Drawings . . . 56
7.9. Inner Structure Design of RPCs . . . 59
7.10. Uploading to the Oracle Database . . . 62
7.11. How ATLAS Simulation Works . . . 62
7.12. Importance of Detector Simulation . . . 63
7.13. Simulation for BIS78 . . . 64
7.14. Observation in Simulation . . . 65
7.15. Updates in Software . . . 67

7.15.1. Updates in MuonGeoModel 67
7.15.2. Resolving Active Area Issue 67
7.16. Redefining the Active Area in Simulation 72
7.16.1. Fixing Digits 74
8. CONCLUSION 90
REFERENCES 91
APPENDIX A: PERMISSION FOR USING FIGURES 93
APPENDIX B: INNER STRUCTURE OF RPCS IN BIS78 94
APPENDIX C: DESIGN DRAWINGS OF BIS7/8 96
APPENDIX D: RPC TOY MODEL GEANT4 SIMULATION PACKAGE . . 108

LIST OF FIGURES

Figure 2.1. A basic main() Method in Geant4 [2]. 8

Figure 2.2. Creating a world space in Geant4 and the example of creating the solid cylinder [2]. 9

Figure 2.3. Creating the logical volume and placing the physical volume [2]. . 9

Figure 2.4. Creating the liquid argon and retrieving the materials from Geant4 Material Datase [2]. 9

Figure 2.5. Producing geantino and proton [2]. 10

Figure 2.6. Electromagnetic process for gamma is shown in this example [2]. . 10

Figure 2.7. The example of Primary Generator package [2]. 11

Figure 2.8. The distribution of the energy that muons lost in 20cm thickness of copper box with 1 GeV initial energy. 12

Figure 2.9. The distribution of the energy that muons lost in 60cm thickness of copper box with 1 GeV initial energy. 13

Figure 2.10. The distribution of the energy that muons lost in 1cm thickness of copper box with 200 MeV initial energy. 13

Figure 2.11. The distribution of the energy that muons lost in 1cm thickness of copper box with 300 MeV initial energy. 14

Figure 2.12. The Landau distribution distrubution in energies that muons lost in 1cm thickness of copper box with 100 MeV initial energy. . . . 15

Figure 3.1. The Inner Detector of ATLAS [3]. 18

Figure 3.2. The axis system of ATLAS. 19

Figure 3.3. Sector and octant numbering and of Muon System of ATLAS. . . 22

Figure 3.4. Structure of a Resistive Plate Chamber of the ATLAS experiment [4]. 23

Figure 3.5. Muon Trigger Scheme [5]. 25

Figure 4.1. The design of BI RPC [4]. 29

Figure 4.2. Reconstruction and identification efficiency of muons for interaction of $Z \rightarrow \mu\mu$ decays as a function of the pseudorapidity for muons with $p_T > 10$ GeV, and as a function of the transverse momentum for muons in the region $0.1 <| \eta |< 1.3$. Three running scenarios are compared: no pile-up (blue circles), $\langle\mu\rangle = 200$ without the effect of cavern background (red squares), and $\langle\mu\rangle = 200$ with cavern background (orange triangles). A shaded area indicates the systematic uncertainty on the amount of simulated cavern background [4]. 31

Figure 5.1. p_t dependence of efficiency. 33

Figure 5.2. η and ϕ profile of muons. 34

Figure 5.3. η and ϕ residual of muons. 35

Figure 5.4. p_t residual of muons and inverse p_t residual of muons with cut. . . 36

Figure 6.1. Transverse section of a small sector in the barrel region [4]. 37

Figure 6.2. 2D colored histogram of η and ϕ versus quality values. 39

Figure 6.3. 2D colored histrogram of ThrValue versus quality and RoI muon pt and thrValue of RoI that has muon. 39

Figure 6.4. P_t dependence of trigger efficiency to the pile-up and trigger algorithms. 40

Figure 7.1. Various views of Persint [6]. 43

Figure 7.2. Upgraded cross-sectional view of Muon System [4]. 43

Figure 7.3. Three axis systems in AMDB [6]. 45

Figure 7.4. Barrel and End Caps local axis systems in AMDB [6]. 45

Figure 7.5. AMDB D entries [7]. 46

Figure 7.6. D entry parameters and the local coordinates [7]. 46

Figure 7.7. Basic shapes of the object with technology MDT, RPC, TGC, SUP, SPA and CSC [7]. 47

Figure 7.8. General scheme of creating a station with cutout description [7]. . 48

Figure 7.9. Parameters of cutout description [7]. 48

Figure 7.10. AMDB P entries [7]. 48

Figure 7.11. W entries of AMDB for RPC. 49

Figure 7.12. Longitudinal view of current BIS and new BIS chambers via Persint. 50

Figure 7.13. Drawing of BIS78 sector for the first octant side A. 51

Figure 7.14. Visualization of MDT Tubes & RPC Chambers Front View for the first octant side A in Persint. 52

Figure 7.15. Corresponding D entry parameters in the drawing. 53

Figure 7.16. AMDB D entries of one sector in the drawing. 53

Figure 7.17. Illustrations of local y and z values difference between two objects. 54

Figure 7.18. Example of one sector global positioning in Persint. 55

Figure 7.19. Implementation of position parameters into AMDB. 55

Figure 7.20. Basic shapes of RPCs in BIS78. 56

Figure 7.21. Basic shapes of Top MDTs in BIS78. 57

Figure 7.22. Illustration of formation of cut-out pieces. 58

Figure 7.23. Implementation of cut-out parameters to AMDB. 58

Figure 7.24. η and ϕ strips in BIS78 RPCs. 59

Figure 7.25. Gas gaps and strip positions of big RPC7 60

Figure 7.26. Illustration of pitch in Persint and pitch calculation in the drawing. 61

Figure 7.27. Illustration of total thickness parameter in drawings and Persint. . 61

Figure 7.28. Gas volume and Strip panel parameter in the drawings. 62

Figure 7.29. The exclusion plot on Higgs Boson [9]. 64

Figure 7.30. Example of retrieving information of AMDB in Athena framework. 64

Figure 7.31. The first version of code defining active area in Y and Z directions and the modifications made for redefining the active area. 69

Figure 7.32. the piece of code making shifts in Y and Z directions. 69

Figure 7.33. Simulation Hits for deadFrameSizeEta=0. and deadframesizeEta=500. in Z direction. 70

Figure 7.34. Simulation Hits for deadFrameSizePhi=0. and deadFrameSizePhi=500. in Y direction. Because of inclination in Y direction, the contraction amount will be different from the deadFrameSizePhi value. . 70

Figure 7.35. Simulation Hits for deadFrameSizeEta=0., tz = 450. in Z direction. 71

Figure 7.36. Simulation Hits for deadframesize=0., ty = 300. in Y direction. . 71

Figure 7.37. Strip volume position in the drawings. 73

Figure 7.38. Redefining active areas of RPC26 and RPC27. 73

Figure 7.39. Redefining active areas of RPC28 and RPC29. 74

Figure 7.40. Translation objects in the code. 74

Figure 7.41. Simulation hits in Z direction and η strips digits correspondance. Blue color is for the simulation hits and red color is for the digits. This is the first octant of RPC7. 75

Figure 7.42. Simulation hits in Y direction and ϕ strips digits correspondance. Blue color is for the simulation hits and red color is for the digits. This is the first octant of RPC7. 76

Figure A.1. The Permission from ATLAS Secretariat. 93

Figure C.1. RPC and sMDT design for octant 1 side A. 96

Figure C.2. RPC and sMDT design for octant 2 side A. 97

Figure C.3. RPC and sMDT design for octant 3 side A. 98

Figure C.4. RPC and sMDT design for octant 4 side A. 99

Figure C.5. RPC and sMDT design for octant 5 side A. 100

Figure C.6. RPC and sMDT design for octant 6 side A. 101

Figure C.7. RPC and sMDT design for octant 7 side A. 102

Figure C.8. RPC and sMDT design for octant 8 side A. 103

Figure C.9. Big RPC7 inner structure design. 104

Figure C.10. Small RPC7 inner structure design. 105

Figure C.11. Big RPC8 inner structure design. 106

Figure C.12. Small RPC8 inner structure design. 107

LIST OF TABLES

Table 6.1. Quality and their corresponding trigger schemes. 38

Table 7.1. Simulation hits coordinates in Z direction for RPC7 all sectors. . . 66

Table 7.2. Simulation hits coordinates in Z direction for RPC7 in all sectors. 77

Table 7.3. Simulation hits coordinates in Z direction for RPC8 in all sectors. 78

Table 7.4. Simulation hits coordinates in Y direction for RPC7 in all sectors. 79

Table 7.5. Simulation hits coordinates in Y direction for RPC8 in all sectors. 80

Table 7.6. Simulation hits coordinates in Y direction for RPC7 for each gas gap in all sectors. 81

Table 7.7. Simulation hits coordinates in Y direction for RPC8 for each gas gap in all sectors. 82

Table 7.8. Simulation hits coordinates in Y direction for RPC7 in all sectors for each gas gap. 83

Table 7.9. Simulation hits coordinates in Y direction for RPC7 in all sectors for each gas gap. 84

Table 7.10. Simulation hits coordinates in Y direction for RPC8 for each gas gap in all sectors. 85

Table 7.11. Simulation hits coordinates in Y direction for RPC8 in all sectors for each gas gap. 86

Table 7.12. Simulation hits coordinates in Y direction for RPC8 for each gas gap in all sectors. 87

Table 7.13. Simulation hits coordinates in Y direction for RPC8 in all sectors for each gas gap. 88

Table 7.14. Pitch Values and Number of Srips for RPC7 and RPC8 in all sectors. 89

Table B.1. General Scheme of RPC Inner Structure. 94

Table B.2. RPC Inner Structure in the code. 95

LIST OF SYMBOLS

B	B meson
E_T	Transverse Energy
e	electron
H	Higgs Boson
$\mathcal{L}$	Luminosity
p_t	Transverse momentum
$W^{\pm}$	W Boson With + Or − Electrical Charge
Z	Z boson
μ	muon particle
η	Pseudorapidity
η	eta strips
θ	Polar Angle
ϕ	Azimuthal Angle
ϕ	Phi Strips

LIST OF ACRONYMS/ABBREVIATIONS

2D	Two Dimensional
3D	Three Dimensional
ATLAS	A Toroidal LHC ApparatuS
ALICE	A Large Ion Collider Experiment
AMDB	ATLAS Muon Spectrometer Detector Describtion Database
BI	Barrel Inner
BIS	Barrel Inner Small
BM	Barrel Middle
BO	Barrel Outer
BSM	Beyond Standard Model
CERN	The European Organization For Nuclear Research
cm	centimeter
CMS	Compact Muon Solenoid
CP	Charge conjugation Parity
CSC	Cathode Strip Chamber
Cu	Copper
EM	Electromagnetic
ESD	Event Summary Data
HL-LHC	High Luminosity Large Hadron Collider
ID	Inner Detector
ITk	Inner Tracker
LAr	Liquid Argon
LHC	Large Hadron Collider
LHCb	Large Hadron Collider beauty
LS2	Long Shutdown2
LS3	Long Shutdown 3
LVL1	Level-1
LVL2	Level-2

MDT	Monitored Drift Tube
m	Meter
mm	Millimeter
MS	Muon Spectrometer
NSW	New Small Wheel
Pb	Lead
PS	Proton Synchrotron
PSB	Proton Synchrotron Booster
RPC	Resistive Plate Chamber
RoI	Region of Interest
SCT	Semi-Conductor Tracker
SM	Standard Model
sMDT	Monitored Drift Tube with small diameter
SPS	Super Proton Synchrotron
SUSY	supersymmetry
TGC	Thin Gap Chamber
TRT	Transistion Radiation Tracker
xAOD	Auxilary Analysis Object Data

1. INTRODUCTION

Since 6th century B.C., the essence of the matter has been at the core of Philosophy. The idea of smaller constituents forming the matter lies far back. Jains from the ancient India supported the idea of the matter should be consisting of smaller materials and the ancient Greek philosophers such as Democritus and Epicurus has questioned the essence of the matter as well. In the 19th century, Dalton stated that each element is formed by a particle named atom and it is the fundamental substance to the matter. However, with the discovery of electron by the works of William Crookes, Arthur Schuster and J. J. Thomson between 1879 and 1897, they showed that Dalton's atoms were actually not the end of the story but the beginning of it. This discovery has lifted the veil of mystery world of particles that is yet to be discovered and it has opened a door to an astonishing world of tiny particles that form the atom. With the increasingly discovered new particles by the experiments, Particle Physics research has gained the importance that it has deserved. After Quantum Mechanics (QM) had revealed the idea of new particles, Standard Model (SM) has been established in 1960. Hence, many big institutions has come together to build the facilities that will provide us to study subatomic particles. They built the particle accelerators and the colliders to provide high energy to the particles in order to study their interactions. One of these big facilities, Large Hadron Collider (LHC) was built by European Organization for Nuclear Research (CERN) between 1998 and 2008 in Geneva, Switzerland to allow one to search the rare interactions of particles with the high energy. Study of the particle physics and fundamental forces has a very big range of implications from the development of the early universe to the Medical Physics. Accelerators need extremely high energies in order to study the subatomic particles. Statistically, higher number of particles in a collision results in a greater chance of finding the new physics, new particles and a better measurement on the properties of the known particles. Hence, increasing the luminosity has always been the priority for the accelerators. The biggest accelerator in the world, LHC, will go under a drastic change by increasing the luminosity by the factor of four, which is High Luminosity LHC (HL-LHC). HL-LHC will

present an efficient environment for inquiring more of supersymmetry (SUSY), exotic particles and higgs boson properties as it will be bringing many challenges. In order to cope with the new environment that HL-LHC will bring, LHC experiments must do the necessary upgrades. A Toroidal LHC ApparatuS (ATLAS) as the largest detector of LHC will go through many changes. One of the most important upgrades is to add the additional Resistive Plate Chamber (RPC) into the inner barrel region (BI) of the detector, which is BIS78. This new sector will provide a better momentum and time resolution of muons and it will extend to trigger coverage. This thesis documents the simulation of new ATLAS environment with BIS78 sector. Initially the new geometry is described in ascii file named ATLAS Muon Spectrometer Detector Description Database (AMDB) in order to put it into the ATLAS Oracle Database forming the geometry that will be used in the simulation. Then, this simulation is tested in terms of physics performance. Physics performance studies such as reconstruction efficiency is directly related to the simulation hits and their matching with the digits. Hence, the active area of the detector which is responsible for the simulation hits is researched and the responsible part of Athena framework is modified in order to be sure of the new geometry is satisfying the expected physics performance.

2. THEORY

2.1. Ionization Detectors

Ionization detectors [10] are the first radiation detection instruments. These devices are based on the direct collection of ionization electrons and ions produced in a gas while passing through. In the 1900s, three basic types of detector were developed: the ionization chamber, the proportional counter and the Geiger-Muller counter. However, these devices are not used in today's Particle Physics experiments except for specific purposes. Their basic design and structure has not been changed drastically when the scintillation counter has taken the places of these devices in 1940s in nuclear search. During the late 1960s, the invention of the *multi-wire proportional chamber* has re-stimulated the interest in gas ionization instruments in particle physics. These devices were capable of localizing particle trajectories to less than a millimeter and were quickly adopted in high-energy experiments. With the encourage by this success, in the following years, the drift chamber and later, the time projection chamber were developed. These devices' basic principles are similar to the simple proportional counter, however they are different physically from their simpler predecessor. They are now used widely in particle physics experiments and require more sophisticated electronics as well as data acquisition by computer.

2.2. Gaseous Ionization Detectors

Ionization detectors [10] are the first radiation detection instruments. These devices are based on the direct collection of ionization electrons and ions produced in a gas while passing through. In the 1900s, three basic types of detector were developed: the ionization chamber, the proportional counter and the Geiger-Muller counter. However, these devices are not used in today's Particle Physics experiments except for specific purposes. Their basic design and structure has not been changed drastically when the scintillation counter has taken the places of these devices in 1940s in nuclear

search. During the late 1960s, the invention of the *multi-wire proportional chamber* has re-stimulated the interest in gas ionization instruments in particle physics. These devices were capable of localizing particle trajectories to less than a millimeter and were quickly adopted in high-energy experiments. With the encourage by this success, in the following years, the drift chamber and later, the time projection chamber were developed. These devices' basic principles are similar to the simple proportional counter, however they are different physically from their simpler predecessor. They are now used widely in particle physics experiments and require more sophisticated electronics as well as data acquisition by computer.

2.3. Gaseous Ionization Detectors

Since the electrons and ions can move easily in a gas, the gas is a good medium to collect the ionization from radiation. Ionization phenomena in gases has been studied in the detectors over the years. The three original devices of gaseous detectors that are the ionization chamber, the proportional counter and the Geiger-Muller counter represent a decent example of gas ionization. They work in same principal however operating in different parameters and exploring the different phenomena. The basic structure of a gas ionization detector consists of the container which is a conducting cylinder for simplicity and it has a thin end window. The cylinder is filled with an appropriate gas which is usually a noble gas. Along in its axis, there is a conducting wire where positive voltage $+V_0$ is applied relative to the walls. There is a radially symmetric electric field where r is radial distance from axis, b is inside radius of cylinder, a is radius of central wire.

$$E = \frac{1}{r}\frac{V_0}{ln\frac{b}{a}} \tag{2.1}$$

When the radiation penetrates through the cylinder, certain number of electron-ion pairs will be created directly if the radiation is a charged particle or as secondary reactions if the radiation is neutral. The average number of pairs is proportional to the energy deposited in the counter. Under the influence of electric field, electrons

accelerate towards the anode and ions towards the cathode where they will be collected. The current signal observed depends on the intensity of field where draws the total charge collected as a function of V. Since the ion-electron pair recombine under their own electrical attraction, at zero voltage there is no collected charge. However, as the current increases, it overcomes the recombination of electron-ion pairs and more pairs will be collected. Of course, at some point, all of the created pairs will be collected and voltage will not have any effect. A detector is called the ionization chamber when it collects the pairs produced directly as radiation passing through. Since the signal is very small, it must be measured with an electrometer. The ionization chambers are used for monitoring the large flux of radiation and measuring gamma ray exposures. When the voltage increases the current also increases at this point, electric field is strong enough to accelerate the free electrons which are able to ionize the gas molecules in the cylinder. Electrons produced in this secondary ionization will repeat this action in this way and results in avalanche effect. Since the electric field is the strongest near the anode, this effect can happen very quickly in a few radii of wire. The fact that the number of electron-ion pair is proportional to the primary electrons results in a proportional amplification of the current with a multiplication factor depending on the working voltage V. This factor can be large as 10^6 so the output signal will be much larger than that but still proportional to the primary ionization in the detector. This region is called the proportional chamber. When the voltage increases further after this moment, the total amount of ionization created is large enough to distort the electric field near the anode and the linearity is lost. This region is called as the limited proportionality. When V becomes even higher, the energy will be very high which will cause the discharge in the gas. At this point, instead of a single localized avalanche near the anode, there will be many avalanches spreading out along the whole anode, which is called as chain reaction. These secondary avalanches produced by photons in the de-excitation of the molecules cause the next ionization events. Thus, the output current will be saturated and always give the same amplitude independent from the initial energy. In order to stop the discharge, a quenching gas is used to absorb photons and drain their energy. This voltage region is known as Geiger Muller or breakdown counters. This region is characterised by a plateau where the count rates vary little.

The width of the plateau depends on the *efficacy* of the quencher gas. Generally, the working voltage of Geiger Muller is set to be in the middle of the plateau in order to minimise the changes due to voltage drift. Finally, if the voltage still increases continuous breakdowns will occur and this region must be avoided to prevent damages to the counter. In this section, the phenomena of gas ionization, multiplication and discharge can be used for radiation detection. In this section, we have seen the basic operating principal of Ionization Gaseous Detector which will be useful when studying the main object of this thesis, RPC detector which is a type of Ionization Gaseous Detector.

2.4. GEANT4

Geant4 [1] is an open source program which simulates the passage of particles through a material very accurately in terms of physics studies.

Main Capabilities of Geant4: It can define,

- the geometry of the system,
- the materials involved,
- the fundamental particles of interest,
- the generation of primary events,
- the tracking of particles through materials and electromagnetic fields,
- the physics processes governing particle interactions,
- the response of sensitive detector components,
- the generation of event data,
- the storage of events and tracks,
- the visualization of the detector and particle trajectories, and
- the capture and analysis of simulation data at different levels of detail.

2.4.1. How Geant Works

For a basic Geant simulation, one has to build a detector geometry, particle source, particle types and properties and physical interactions. In this section, we will focus on these steps.

main() Method: It is required to build simulation. It creates the G4RunManager which controls the flow of the program and this creates the objects such as ExG4DetectorConstruction01, ExG4PhysicsList00, ExG4ActionInitialization01 which respectively builds the detector geometry, defines Physics Processes and how particles should be produced.

How to Define a Detector Geometry: In order to define a geometry whether if it is simple or complex, it has to have an initial space that will hold the geometry together, which is called *World Box* in Geant (see Figure 2.2). Then, the one can create the geometry of its desire inside of it. For the detector geometry, a solid must be created in the first place, where one can define its shape, name and dimensions. The name of the volume is crucial since the further attributions can be pointed via the names. After creating the solid, the logical volume must be created where one can define the material of the detector. In order to put the logical volume in a certain place in the space, physical volume must be created. A volume inside of another volume can be created as well. In this case, the big volume is called as *Mother Volume* and the latter one is called as *Daughter Volume*. Origin of the coordinate system is the center of mass of mother volume.

How to define Material: The material information can be directly retrieved from the list of Geant4 Material Database or it can be defined manually.

How to Specify Particles: One can determine the particles in PrimaryGeneratorAction package as in Figure 2.5.

How to Specify Physics Processes: Physics processes determine how the particles interact with the material. Geant4 presents 7 main physics processes:

- electromagnetic,
- hadronic,
- transportation,
- decay,
- optical,
- photolepton-hadron,
- and parameterisation (Fast Simulation).

How to Generate a Primary Event: This is the part where one specifies the source of the particles such as particle gun and its position and the energy of the particle as well. This is one of the most important packages.

```
#include "G4RunManager.hh"
#include "G4UImanager.hh"

#include "ExG4DetectorConstruction01.hh"
#include "ExG4PhysicsList00.hh"
#include "ExG4ActionInitialization01.hh"

int main()
{
  // construct the default run manager
  G4RunManager* runManager = new G4RunManager;

  // set mandatory initialization classes
  runManager->SetUserInitialization(new ExG4DetectorConstruction01);
  runManager->SetUserInitialization(new ExG4PhysicsList00);
  runManager->SetUserInitialization(new ExG4ActionInitialization01);

  // initialize G4 kernel
  runManager->Initialize();

  // get the pointer to the UI manager and set verbosities
  G4UImanager* UI = G4UImanager::GetUIpointer();
  UI->ApplyCommand("/run/verbose 1");
  UI->ApplyCommand("/event/verbose 1");
  UI->ApplyCommand("/tracking/verbose 1");

  // start a run
  int numberOfEvent = 3;
  runManager->BeamOn(numberOfEvent);

  // job termination
  delete runManager;
  return 0;
}
```

Figure 2.1. A basic main() Method in Geant4 [2].

```
 G4double world_hx = 3.0*m;
 G4double world_hy = 1.0*m;
 G4double world_hz = 1.0*m;

 G4Box* worldBox
    = new G4Box("World", world_hx, world_hy, world_hz);
```

```
G4double innerRadius = 0.*cm;
G4double outerRadius = 60.*cm;
G4double hz = 25.*cm;
G4double startAngle = 0.*deg;
G4double spanningAngle = 360.*deg;

G4Tubs* trackerTube
  = new G4Tubs("Tracker",
               innerRadius,
               outerRadius,
               hz,
               startAngle,
               spanningAngle);
```

Figure 2.2. Creating a world space in Geant4 and the example of creating the solid cylinder [2].

```
G4LogicalVolume* trackerLog
  = new G4LogicalVolume(trackerTube, Al, "Tracker");
```

```
G4double pos_x = -1.0*meter;
G4double pos_y =  0.0*meter;
G4double pos_z =  0.0*meter;

G4VPhysicalVolume* trackerPhys
  = new G4PVPlacement(0,                        // no rotation
                      G4ThreeVector(pos_x, pos_y, pos_z),
                                                // translation position
                      trackerLog,               // its logical volume
                      "Tracker",                // its name
                      worldLog,                 // its mother (logical) volume
                      false,                    // no boolean operations
                      0);                       // its copy number
```

Figure 2.3. Creating the logical volume and placing the physical volume [2].

```
G4double z, a, density;
density = 1.390*g/cm3;
a = 39.95*g/mole;

G4Material* lAr = new G4Material(name="liquidArgon", z=18., a, density);
```

```
G4NistManager* man = G4NistManager::Instance();

G4Material* H2O  = man->FindOrBuildMaterial("G4_WATER");
G4Material* Air  = man->FindOrBuildMaterial("G4_AIR");
```

Figure 2.4. Creating the liquid argon and retrieving the materials from Geant4 Material Datase [2].

```
void MyPhysicsList::ConstructParticle()
{
  G4Proton::ProtonDefinition();
  G4Geantino::GeantinoDefinition();
}
```

Figure 2.5. Producing geantino and proton [2].

```
void MyPhysicsList::ConstructProcess()
{
  // Define transportation process
  AddTransportation();
  // electromagnetic processes
  ConstructEM();
}

void MyPhysicsList::ConstructEM()
{
  // Get pointer to G4PhysicsListHelper
  G4PhysicsListHelper* ph = G4PhysicsListHelper::GetPhysicsListHelper();

  //  Get pointer to gamma
  G4ParticleDefinition* particle = G4Gamma::GammaDefinition();

  // Construct and register processes for gamma
  ph->RegisterProcess(new G4PhotoElectricEffect(), particle);
  ph->RegisterProcess(new G4ComptonScattering(), particle);
  ph->RegisterProcess(new G4GammaConversion(), particle);
  ph->RegisterProcess(new G4RayleighScattering(), particle);
}
```

Figure 2.6. Electromagnetic process for gamma is shown in this example [2].

```
#include "G4ThreeVector.hh"
#include "globals.hh"

class G4ParticleGun;
class G4Event;

class ExG4PrimaryGeneratorAction01 : public G4VUserPrimaryGeneratorAction
{
  public:
    ExG4PrimaryGeneratorAction01(
      const G4String& particleName = "geantino",
      G4double energy = 1.*MeV,
      G4ThreeVector position= G4ThreeVector(0,0,0),
      G4ThreeVector momentumDirection = G4ThreeVector(0,0,1));
    ~ExG4PrimaryGeneratorAction01();

    // methods
    virtual void GeneratePrimaries(G4Event*);

  private:
    // data members
    G4ParticleGun*  fParticleGun; //pointer a to G4 service class
};

#endif

//////////////////////////////////
// ExG4PrimaryGeneratorAction01.cc
//////////////////////////////////

#include "ExG4PrimaryGeneratorAction01.hh"

#include "G4Event.hh"
#include "G4ParticleGun.hh"
#include "G4ParticleTable.hh"
#include "G4ParticleDefinition.hh"

//....oooOOOOOooo........oooOOOOOooo........oooOOOOOooo........oooOOOOOooo.

ExG4PrimaryGeneratorAction01::ExG4PrimaryGeneratorAction01(
                              const G4String& particleName,
                              G4double energy,
                              G4ThreeVector position,
                              G4ThreeVector momentumDirection)
  : G4VUserPrimaryGeneratorAction(),
    fParticleGun(0)
{
  G4int nofParticles = 1;
  fParticleGun  = new G4ParticleGun(nofParticles);

  // default particle kinematic
  G4ParticleTable* particleTable = G4ParticleTable::GetParticleTable();
  G4ParticleDefinition* particle
    = particleTable->FindParticle(particleName);
  fParticleGun->SetParticleDefinition(particle);
  fParticleGun->SetParticleEnergy(energy);
  fParticleGun->SetParticlePosition(position);
  fParticleGun->SetParticleMomentumDirection(momentumDirection);
}

//....oooOOOOOooo........oooOOOOOooo........oooOOOOOooo........oooOOOOOooo.

ExG4PrimaryGeneratorAction01::~ExG4PrimaryGeneratorAction01()
{
  delete fParticleGun;
}
```

Figure 2.7. The example of Primary Generator package [2].

2.5. Simulation of Toy Model RPC

In order to understand the simulation of real RPC structure in Chapter 5, it will be wise to do standalone toy model simulation of RPCs. In this model, the copper box shape with dimension of $60cm \times 100cm \times 1cm$ is created and the single muon from the particle gun is sent through z direction to the box. For this study, it is analysed that the single muon with a certain energy, how much energy deposits in different thickness; and the single muon with varying energy, how much energy deposits in a certain thickness. In this analysis, the number of events is 100.

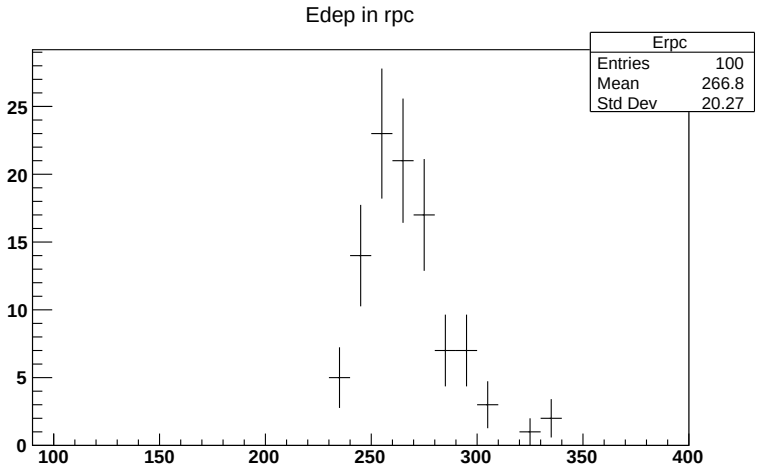

Figure 2.8. The distribution of the energy that muons lost in 20cm thickness of copper box with 1 GeV initial energy.

2.5.1. Bethe Formula

In order to describe the mean energy that particle lost traversing the material, Bethe formula [11] is used which is:

$$-\left\langle \frac{dE}{dx} \right\rangle = \frac{4\pi}{m_e c^2} \frac{nz^2}{\beta^2} \left(\frac{e^2}{4\pi\epsilon_0} \right)^2 \left[\ln \left(\frac{2m_e c^2 \beta^2}{I\left(1-\beta^2\right)} \right) - \beta^2 \right] \tag{2.2}$$

$\beta = \frac{v}{c}$, $n = \frac{N_A Z \rho}{A M_u}$ where ρ is the density of the material, Z its atomic number, A its relative atomic mass,N_A the Avogadro number and M_u the Molar mass constant. For

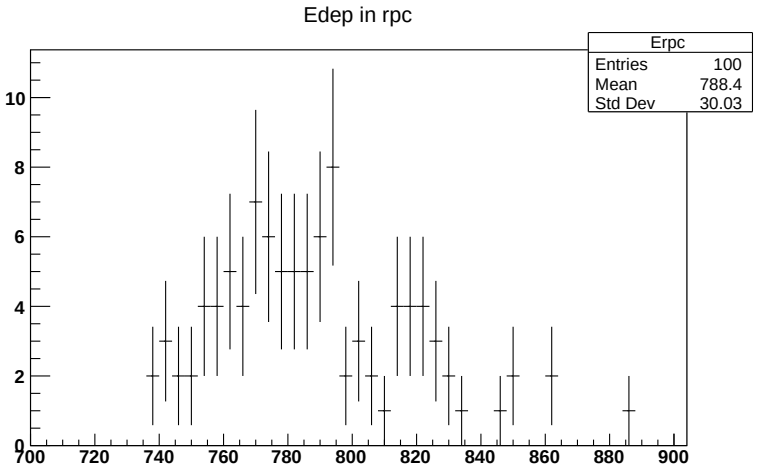

Figure 2.9. The distribution of the energy that muons lost in 60cm thickness of copper box with 1 GeV initial energy.

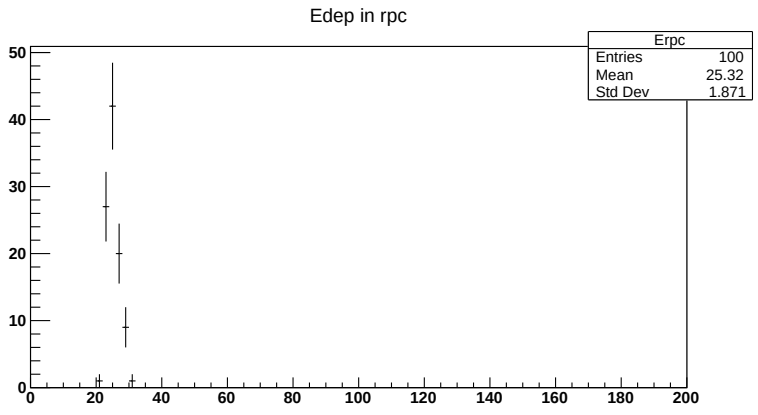

Figure 2.10. The distribution of the energy that muons lost in 1cm thickness of copper box with 200 MeV initial energy.

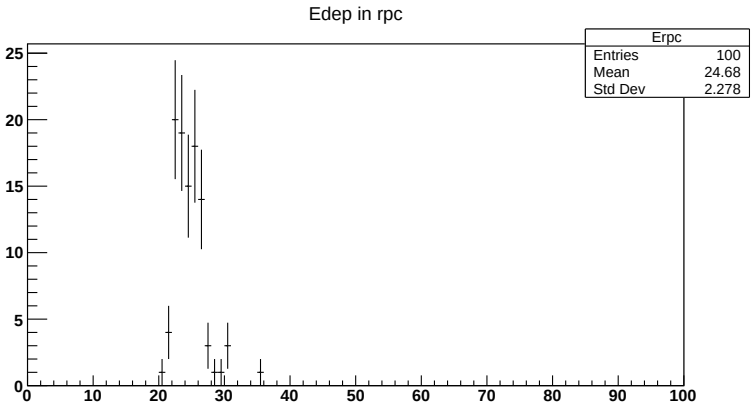

Figure 2.11. The distribution of the energy that muons lost in 1cm thickness of copper box with 300 MeV initial energy.

small velocities, $\beta << 1$, the equation becomes,

$$-\frac{dE}{dx} = \frac{4\pi}{m_e c^2}\frac{nz^2}{v^2}\left(\frac{e^2}{4\pi\epsilon_0}\right)^2\left(\frac{\ln(2m_e v^2)}{I}\right) \tag{2.3}$$

In Bethe theory, the material is completely described by a single number, the mean excitation potential I. In 1933 Felix Bloch showed that the mean ionization potential of atoms is approximately given by

$$I = (10eV)Z \tag{2.4}$$

2.5.2. Landau Distribution

The most probable energy loss of a particle traversing the material is described by Landau-Vavilov distribution [11]. The probability density is stated below where a is an arbitrary positive real number and log refers to the natural logarithm.

$$p(x) = \frac{1}{2\pi}\int_{a-i\infty}^{a+i\infty} e^{(s\ln s + xs)}ds \tag{2.5}$$

The following real integral is equivalent to the above:

$$p(x) = \frac{1}{\pi}\int_0^\infty e^{-t\ln t - xt}\sin(\pi t)dt \tag{2.6}$$

The Landau distribution with parameters α =1 and β =1, with characteristic function is stated below where $c \in (0,\infty)$ and $\mu \in (-\infty,\infty)$ and a density function:

$$\varphi(t;\mu,c) = \exp\left(it\mu - \frac{2ict}{\pi}\ln|t| - c|t|\right) \tag{2.7}$$

$$p(x;\mu,c) = \frac{1}{\pi c}\int_0^\infty e^{-t}\cos\left[t\left(\frac{x-\mu}{c}\right) + \frac{2t}{\pi}\ln\left(\frac{t}{c}\right)\right]dt, \tag{2.8}$$

Let us note that the original form of $c = \frac{\pi}{2}$, while the following is an approximation of $p(x;\mu,c)$ for $\mu = 0$ and c=1:

$$p(x) \approx \frac{1}{\sqrt{2\pi}}\exp\left(-\frac{x+e^{-x}}{2}\right) \tag{2.9}$$

We see that in Figure 2.12, Landau distribution applies to our plot.

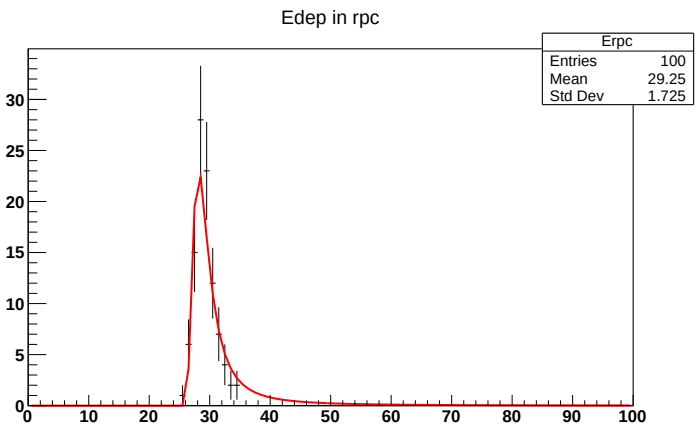

Figure 2.12. The Landau distribution distrubution in energies that muons lost in 1cm thickness of copper box with 100 MeV initial energy.

3. ATLAS

3.1. ATLAS (A Troidal LHC ApparatuS) Experiment

The Large Hadron Collider (LHC) is a two-ring-superconducting hadron accelerator and collider where two proton beams and heavy ions (Pb) are collided. Proton-Proton beams having center of mass energy with 13 TeV and with luminosity of $10^{34} cm^{-2} s^{-1}$ can cross in four point where four main experiments are located: ATLAS, CMS, ALICE and LHCb. At the crossing points, the angle between the beams is 200 microradians. Each proton beams consists of 2835 bunches of 10^{11} protons. These beams are formed in Proton Synchrotron (PS) with 26 GeV in every 25 ns and then injected in the Super Proton Synchrotron (SPS) after three PS cycles, hence, 1/3 of SPS is filled. The beam in the final state is accelerated to 450 GeV and then transmitted to the LHC. This cycle is repeated 12 times in order to fill both the LHC counter rotating beams. The ATLAS is the largest multi-purpose particle accelerator experiment in the LHC. It is designed to search the massive particles that has not been observed by the former lower energy accelerators with the enormous energy provided by the LHC. ATLAS is one of the two experiments of the LHC which has discovered the Higgs boson in 4th of July, 2012. It is formed by a group of physicist in 1992 to lead the experiment. The ATLAS is an enormous collaboration which has approximately 3000 physicists from 183 institutions in 38 countries. The ATLAS detector (see Figure 3.2) has 44 meters long and 25 meter diameter. It weighs approximately 7000 tonnes with 3000 km cables inside of it. The ATLAS experiment is searching for a very broad range of particle physics topics such as Physics beyond the Standard Model (BSM), Top quarks, CP violation, Supersymmetry and microscopic Black holes. Since it is not designed for one particular physics process, it has a layered structure and the layers have different type of detectors for different physics processes to search. The ATLAS detector is made of series of concentric cylinders around the collision point. It has 4 main subsections: the Inner Detector, calorimeters, the Muon Spectrometer and the magnet systems. The Inner Detector tracks the particles and calorimeters measure

the energy of the particle and the Muon Spectrometer measures the energy of muons. The magnet system bend the charged particles in the Inner Detector and the Muon Spectrometer to allow to measure the momenta of the particle, in a sense all parts are redundant to each other.

3.1.1. ATLAS Coordinate System

The coordinate system of ATLAS can be seen in Figure 3.2. In this axis system, collision point is taken as origin, the beam direction as Z axis, X axis towards the center of LHC and Y axis towards the surface, together they form the right handed axis system. The pseudorapidity η is defined as $\eta = -\ln\left[\tan\left(\frac{\theta}{2}\right)\right]$. Other quantities in Figure 3.2 are defined as $\phi = \tan^{-1}\left(\frac{p_y}{p_x}\right)$, $\theta = \cot^{-1}\left(\frac{p_z}{p_t}\right)$.

3.1.2. Inner Detector

The inner detector begins a few centimeters from the collision point and extends to 1.2 m radius and 6.2 m in the length along the beam pipe. Its main purpose is that detecting particle types and revealing the information of the particles. The magnetic field around the inner detector forces the charged particles to bend. By the Lorentz Law, the particles' momenta and charge can be determined through their curved track. The inner detector has three subsections: The Pixel Detector, The Semi-Conductor Tracker (SCT) and Transition Radiation Tracker (TRT).

The Pixel Detector: It is the innermost part of the inner detector. It has three co-centric layers and three disks on each end cap, containing 1744 modules. Its main material for detecting the particles is silicon which has 250 μm of thickness. The smallest unit that can be readout is pixel (50 by 400 micrometres). The *minute pixel* size is designed for good precision in tracking. There are over 80 million readout channels which corresponds to the 50% of the total readout channels in the inner detector.

The Semi-Conductor Tracker (SCT): It is positioned at the middle part of the inner detector. Its basic function is similar to the Pixel detector, however, it has long, narrow strips instead of pixels. It has four double silicon layer and 6.3 million readout channels. Each strips measures 80 micrometers by 12 centimeters. It covers larger area than the Pixel Detector and has more hits for tracking. Hence it plays a significant role in the inner detector.

Transition Radiation Tracker (TRT): It is in the outermost part of the inner detector. TRT has the properties of two detector types: Straw tracker (a type of gaseous detector) and Transition radiation detector. The detecting elements are straws which has the diameter of 4 mm and the length up to 1440 mm. The TRT has approximately 298,000 straws. The position resolution is roughly 200 μ m which is not as precise as the other subsection of the inner detector but it helps the coverage of large volumes. TRT is working in two main steps: First step is to function as a typical gaseous detector where a charged particle passes through the straw filled with gas and it ionizes the gas which is creating a signal in the wire. The signals (hits) provide the information about the particle's path. Second step is to function as a Transition radiation detector. The material between the straws, which has a varying index of refraction, cause ultra relativistic charged particles to radiate.

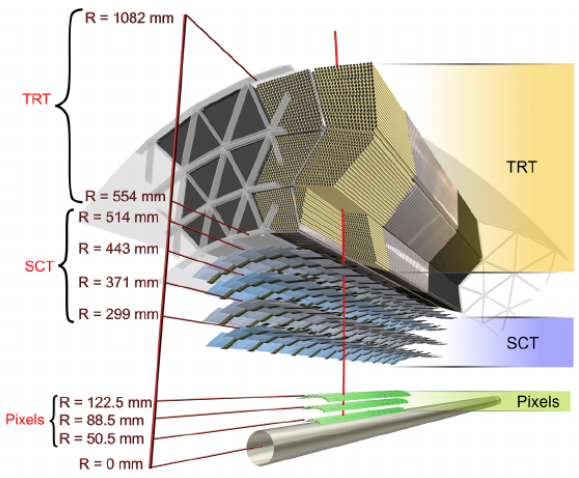

Figure 3.1. The Inner Detector of ATLAS [3].

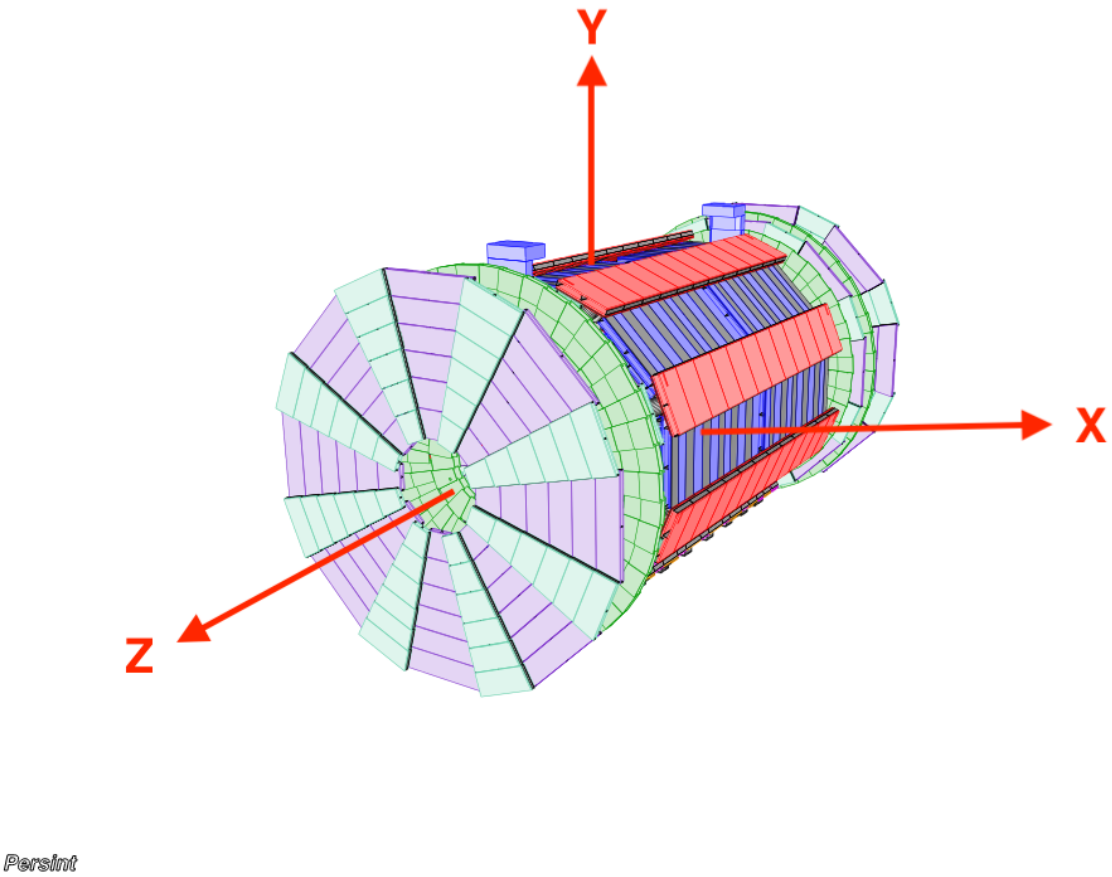

Figure 3.2. The axis system of ATLAS.

3.1.3. Calorimeter

The calorimeters are positioned outside the solenoidal magnet surrounding the inner detector. They measure the particles' energy by absorbtion. The calorimeters is formed of two basic parts: an inner electromagnetic calorimeter and an outer hadronic calorimeter. Electromagnetic (EM) calorimeter absorbs the energy of electromagnetically interacting particles which are charged particles and photon. It meausures very precisely the amount of energy and the location of the energy absorbed. The EM calorimeters contain acordeon shaped electrodes, lead, stainless steel and liquid argon (LAr). The cryostot surrounds the EM to keep it cool. The hadron calorimeter absorbs the particles that have strong interaction and pass through the EM calorimeter, which are hadrons. It makes less precise measurement comparing the EM calorimeters in the amount of energy and location of it.

3.1.4. Muon Spectrometer

The Muon Spectrometer (MS) of the ATLAS identifies and measures the momentum of muons in the range of pseudo rapidity $|\eta| < 2.7$ and does the trigger for these particles in the region of $|\eta| < 2.7$. Muons usually pass through the Inner detector and calorimeter undetected since their greater masses do not allow them to deceleration radiation as much as other particles like electron due to bremsstrahlung. They can penetrate more deeply. This is the reason why the Muon Spectrometer is positioned in the outermost of the ATLAS. The Muon spectrometer consists of chambers and chambers consist of several tubes filled with gas. While muons pass through these tubes, it ionises the gas, and the electrons or ions are going to the center of tube and it gives signal, leaves hits. These signals, hits coming from the layers, chambers are being combined with the time it takes and the position of the muon in the beam will have been detected. The MS is an enormously large tracking system which has 3 toroidal magnets, 1200 chambers measuring the tracks of muons with high precision and a set of chambers for trigger with a good time resolution. The MS starts at radius of 4.25 m in the ATLAS and it extends to the radius of 11 m. It has one million readout

channels and it covers the area of 1200 m^2. It was designed to measure the standalone momentum with 3% accuracy for 100 GeV muons and 10% accuracy of 1 TeV muons. The Muon Spectrometer is formed of three air-core toroid magnets, one in the barrel ($|\eta| < 1.05$) and 2 in the end caps, and the particle detectors for both the trigger and tracking. Since the low amount of material pass through the Muon Spectrometer, it has a precise determination in transverse momentum. The MS consists of 4 main subsections: Thin Gap Chambers (TGC), Resistive Plate Chamber (RPC), Monitored Drift Tubes (MDT), and Cathod Strip Chambers (CSC). The MS is divided in 8 equal parts in ϕ as octants in Z projection and their sector number correspondences can be seen in Figure 3.3[1] .

Monitered Drift Tubes (MDT): It is formation of gas filled tubes with 30. mm diameter and the varying length of 1-6 m. Charged particles ionize the gas inside of the tubes and the ionized electrons give signal to readout electronics and it is converted to data. The MDTs can do a precise measurement on momentum of muons in the region of $|\eta| < 2$.

Thin Gap Chambers (TGC). It is a multi-wire chamber whis is a part of the ATLAS trigger system and it covers the region of $1.05 < |\eta| < 2.7$. There is 1.4 mm between wire and cathode and 1.8 mm between two wires.

Cathode Strip Tubes (CST). It covers the region of $2. < |\eta| < 2.7$. It can provide tarcking measurement in the counting rates up to 1000Hz/cm^2.

Resistive Plate Chambers (RPC) providing information to the muon trigger is positioned in the barrel together with Thing Gap Chambers (TGC) positioned in the End Cap. Monitored Drift Tubes (MDTs) in the barrel and End Cap, and Cathode Strip Chambers in the forward precisely measure the position in the bending plane. RPCs provide the first level muon trigger. Two RPC chambers are located at the barrel middle station (BM) providing the low-p_t trigger information and RPC modules

[1] In Chapter 7, both sector and octant numbers are used.

located at the outer barrel region (BO) provides the high-p_t trigger information with the information by the low-p_t trigger. Each chamber has two detector layers consisting of two sets of orthogonal readout strips measuring η and ϕ coordinates. This redundancy in the track measurement enables a good trigger efficiency by increasing trigger robustness and rejecting fake tracks resulted from noise and cavern background. In a sense, it creates an auto-check for the system.

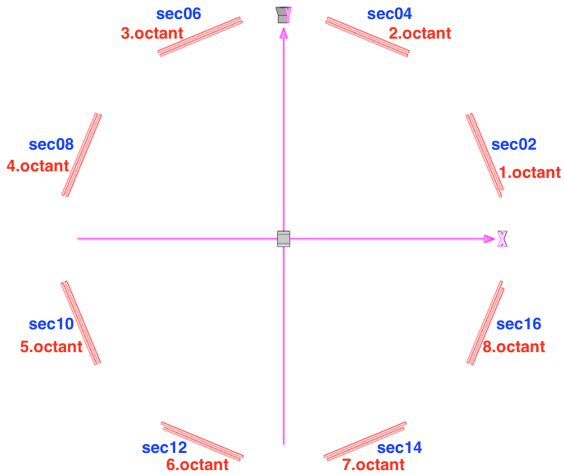

Figure 3.3. Sector and octant numbering and of Muon System of ATLAS.

3.1.4.1. The Resistive Plate Chambers (RPC) of the ATLAS experiment. First publication on RPCs was on 1981. Since then, they had great development and they are widely used in high energy and astroparticle physics experiments. The general structure of RPCs can be seen in Figure 3.4.

RPCs are gaseous detectors and their working principle is based on detection of gas ionization produced by the charged particles when traversing the active part of the detector under a high electric field applied by resistive electrodes [12]. Electrodes are generally made of bakelite and have volume resistivity between 10^9 and 10^{12} Ωcm. In order to facilitate the homogeneous flow of gas between the plates, the distance between them is kept by the insulator spacers. The distance and plates can be varied in different

experiments. The RPC detectors are used as trigger, the usual distance would be 2 mm, on the other hand, for light detectors, the distance can be decreased to 200-300 μm. General characteristics of RPCs used in the ATLAS experiment is that they have 2 mm as the distance between the plates and have 2 mm of thickness. The spacers are cylindrical shape and have 12 mm diameters and placed in every 10 cm in the plates in the both η and ϕ directions. Thin layers of graphite painting cover the plates. Graphite resistivity of 100 kΩ enables high voltage spare equally to the plates and preventing the Faraday Cage that would prevent signal inducing outside the plates. Under the high voltage, smoothness of bakelite plates is provided by covering them with linseed oil. Readout strips have generally 30 mm thickness. The type of gas and usage of high voltage determine the mode of detector. Avalanche mode is the typical Townsend Mechanism. In the ATLAS experiment, gas mixture used in the RPCs is $C_2H_2F_5$ (TetraFlourethane) 94.7% and SF_6 0.3%. RPCs have time resolution of 2 ns. Time resolution makes RPCs good detector.

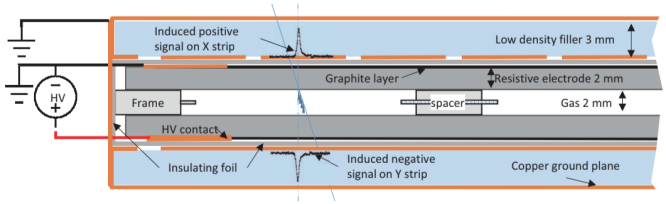

Figure 3.4. Structure of a Resistive Plate Chamber of the ATLAS experiment [4].

3.1.5. ATLAS Trigger System

In the LHC, there are approximately 1 billion proton-proton collisions per second, of course, not all of these events can lead to a new discovery. Hence, the ones that are interesting in terms of physics concerns need to be selected. In order to do that, ATLAS uses a multi-level trigger system [5]. Level-1 works on information from muon detectors and calorimeter. It selects the events made less than 2 microseconds after it occurs. Approximately, 100,000 of 40 million bunch crossings per second is kept here. Level-2 looks at the events that are selected by Level-1 more detailed, Region of

Interest (RoI). A few thousand events per second pass Level-2, then pass on to Level-3. After this level, we have 200 events per second.

3.1.5.1. Muon Trigger. The MS trigger chambers has 3 purposes requiring the followings:

- the identification of bunch crossing with the time resolution better than 25 ns of the LHC's bunch-crossing interval.
- well defined p_T cutoffs with the granularity of order 1 cm.
- measurement of the second coordinate which is orthogonal to the measurement of the precision chambers with the spatial resolution 5-10 mm.

This system includes two types of detectors which are RPC in the barrel and TGC in the end cap. This two combination satisfies the rate capability and the spatial resolution required by physics and the background conditions. Trigger chambers cover about 3650 m^2 in the barrel and 2900 m^2 in the end cap. There are 350 000 readout channels in the barrel and 440 000 in the end cap. Considering the physics objectives, the trigger system must select the muons with $p_t > 6GeV$ and $p_t > 20GeV$ at the nominal luminosity. The MS trigger system psudorapidity coverage of $|\eta| \simeq 2.4$ is enough for B physics and Higgs. For these, multi lepton trigger need to have high and bias-free single muon efficiency. The expected background will require the counting rates in the trigger chambers should be approximately 10 Hz/cm^2 at the nominal luminosity of $1 \times 10^{34} cm^{-2} s^{-1}$ of the LHC. The MS trigger has 3-level trigger system. The level-1 trigger (LVL1) uses reduced-granularity data from the detectors and level-2 trigger (LVL2) uses the data that is found interesting at LVL1 with full granularity and precision. The level-3 trigger (LVL3) uses full event data for the final event selection of offline analysis.

Level-1 Trigger:The drift time of the MDTs is much longer than the LHC bunch-crossing interval of 25 ns, hence, it is crucial to identify the bunch-crossing to reconstruct the trajectories of muons accurately and match the muon trigger to the other triggers from the other detectors. Therefore, the trigger system is designed with

the time resolution shorter than 25 ns. The LVL1 takes the data of the LHC bunch-crossing rate of 40 MHz with a reaction time of 2 μs. The maximum output is limited by 75 kHz with the help of LVL2 trigger and subdetectors readout systems but it can be extended to 100 kHz. The LVL1 trigger must provide the selectivity of $\sim 10^{-4}$. The first level of muon trigger for the barrel region uses three stations of RPC. The two of the stations are installed next to both side of the middle MDT chambers and the third station is installed alongside of the outer MDT. The low-p_t trigger uses only two stations, RPC1 and RPC2 for coincidences. The momentum resolution is about 20% and it is limited by the fluctuations in the central calorimeter due to energy and multiple scattering. The high-p_t trigger uses the coincidences in all three stations. Its momentum resolution is about 30% with p_t of 20 Gev and it is limited due to the multiple scattering in the central calorimeter and the axial length of interaction region.

Level-2 Trigger: The ATLAS level-2 trigger is designed to ease the burden of LVL1 and reduce the rate to the frequency of $\sim$ 1 KHz. In order to reduce the rate by 100 factor, LVL2 must coporate with other subdetectors. LVL2 is processing the information of Region of Interest (RoI) provided by LVL1.

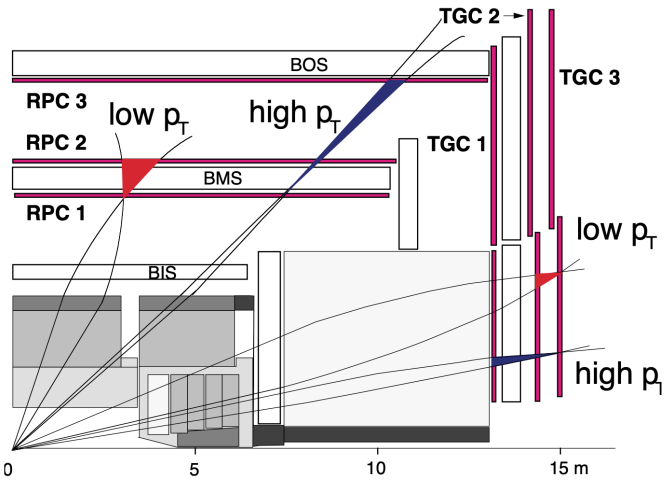

Figure 3.5. Muon Trigger Scheme [5].

4. UPGRADE OF ATLAS FOR HL-LHC

In 2012 December, ATLAS proposed [13] the plans to keep the current detection capabilities and improve with the new challenges that High Luminosity LHC (HL-LHC) will bring in 2025. With the HL-LHC, mass extension will be increased and it will provide us to inquire more of SUSY, exotic particles, Higgs boson properties. Since the fact that the increase of luminosity will result in increase of radiation, the precautions must be taken in this matter, while practicing it. The extra amount of radiation will damage the Inner Detector, hence, it will be replaced by all-silicon tracker to keep up with 10 times higher radiation. DAQ and software systems needs to improve with the upgraded version of the software and hardware systems as well since it needs to be able to cope with the large sample of events.

4.1. ATLAS Upgrade Plans

To explore the physics beyond standard model and electroweak symmetry breaking more deeply, LHC will undergo through drastic change, which is High Luminosity LHC (HL-LHC). With the opportunity brought by increasing luminosity, Particle Physics world will be able to search the Particle Physics subjects that are still mystery such as electroweak symmetry breaking and Physics beyond Standard Model (BSM). Beside the unsolved issues, it will facilitate understand deeply the already discovered particle Higgs boson. However, HL-LHC will bring challenges and to cope with this new environment, LHC experiments must do crucial modifications. The LHC was designed for proton-proton collisions with the center of mass energy $\sqrt{}$ s = 14 TeV and an instantaneous luminosity $1 \times 10^{34} cm^{-2} s^{-1}$. In order to deeply understand the physics processes in LHC, two upgrades are planned [4]. In 2019/2020, during the long shutdown 2 (LS2), the injectors will be upgraded to make the peak luminosity of LHC increase $2^{34} cm^{-2} s^{-1}$ in order to provide an integrated luminosity of 300 fb^{-1} by the end of Run 3 in 2023. The experiments in LHC will be upgraded with the installation of new components during long shutdown (LS3). In the following years of

operation, HL-LHC is expected to deliver peak luminosities of $5^{34}cm^{-2}s^{-1}$, and a total integrated luminosity of 3000 fb^{-1} between 2035-2040. If the circumstances of this new environment can be adjusted, the overall luminosity can increase to $7 - 7.5^{34}cm^{-2}s^{-1}$ with an average pile-up of approximately $\langle\mu\rangle = 200$. These increases in luminosity will result in an integrated luminosity of around 4000 fb^{-1}. The increase in luminosity will bring many challenges to the detectors in LHC since the amount of flow of the particles will increase at the same rate. Therefore, the experiments must take steps to meet these circumstances brought by the new environment. The upgrade of ATLAS will be planned in two steps: the Phase-I during LS2 and the Phase-II upgrade in LS3.

4.1.1. Upgrades in the Muon Spectrometer

Muons play a significant role in HL-LHC. In order to understand the electroweak symmetry breaking in detail, precise measurement of Higgs couplings is crucial and most of the Higgs decay channels include muons, H→Z+Z→ 4μ and H→ $\mu + \mu$ and on the other hand, in Beyond Standard Model, muon channels are crucial such as a rare interaction of B $\rightarrow \mu + \mu$. Hence, precision in muon measurements, p_t resolution and time resolution play crucial role. In upgrade, increased number of events will cause performance to degrade. There will be a huge amount of information that cannot be handled in the current trigger system. To improve the trigger system, additional BIS78 sectors will be added to extend trigger coverage. Hence, BIS78 will be playing an important role in the upgrade. Current Muon Spectrometer of ATLAS has 3 toroidal superconducting magnets providing 0.5 T magnetic field. Muon trajectories are measured via the hits on 3-layers MDT hits in the region of $|\eta| < 2.7$. In the End caps, instead of MDTs, CSCs are present to measure trajectories. The magnetic field inside MS can bend the trajectory such as that average deviation of the curved trajectory from the straight line is 500 micrometer for a $p_T = 1$ TeV. The first level muon trigger is based on RPC and TGC coincidence hits. The maximum rate and latency of the first level trigger are 100 kHz and 2.5 μs. In Phase-I upgrade, during LS2, BIS7 and BIS8 MDT chambers will be replaced by the integrated BIS78 stations of new RPC and small diameter MDTs (sMDT) to enhance the trigger coverage in this region.

4.1.2. BI RPC Upgrade

The BI systems are designed to extend the trigger coverage and enhance the trigger efficiency with the help of the BM and BO chambers. Any 3-hit combination on 3 out of 4 chambers which are one BI, 2 BM and 1 BO will be accepted and the remaining hits combination on BI-BO will be covered. The new BI RPCs will have 3 gas gaps instead of 2 gas gaps which is the case for the other RPCs. This will provide the idea of two out of three planes and this requirement will increase the efficiency and decrease the fake rate caused by photons and neutrons. The RPC technology has been re-designed in 2010, the main purpose was a better rate capability and ageing behaviour. The thickness of RPCs has been reduced from 2 mm to 1 mm and the electrodes resistivity has been changed from 1.8 mm to 1 mm. The new generation of low-noise high-sensitivity amplifiers are used in these new RPCs in order to achieve a good efficiency for a lower voltage across the gas gap, therefore, the charge per avalanche, detector current will be reduced and it will improve the rate capability and ageing process. For BIS, because of the limited space, the MDT chambers will be replaced by a smaller diameter and smaller tube diameter (15 mm instead of 30 mm) MDTs (sMDT) in order to have RPCs inside of the sMDT chambers. With the BI RPC chambers, barrel trigger acceptance becomes 96%. The installation of BI RPCs is a challenge because of the limited space. Hence, the thickness and weight of RPC detectors must be reduced. When the fact that there will be higher hit rates with the HL-LHC is considered, the challenge of creating the chambers can be solved by reducing the gas gain (charge per count) and increasing the sensitivity and signal-to-noise ratio of the front-end electronics while preserving the RPC fast timing capability. The new RPCs design have been formed by considering these requirements. This new generation RPCs will have larger rate capability and smaller weight and thickness beside they will be working in the half of former voltage they used. BIS78 Phase-I will be the first project to use this new technology. This project will add an additional trigger chamber which will be placed in the barrel-endcap region at $1. < |\eta| < 1.3$. The layout of this new module is shown in the Figure 4.1. This module will be in the same place with the envelope of existing BIS7 and BIS8 MDTs. The BIS78 RPC system consists of 16+16

BIS7 and BIS8 triplets. The standard dimensions of the BIS7 and BIS8 chamber are $1820 \times 990 \times 60mm^3$ and $1820 \times 440 \times 50mm^3$.

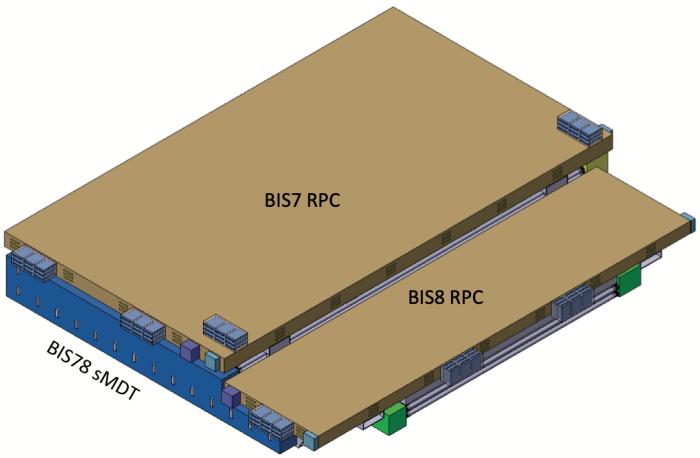

Figure 4.1. The design of BI RPC [4].

The new RPCs have 3 layers and each has strip panels to determine ϕ and η coordinates of the hit. The strip pitches vary between 24-26 mm. They have approximately 8700 readout channels. When the thickness is reduced by half, the working voltage has become from 9600 V to 5400 V and the time resolution will change from 1.1 ns to 0.4 s. Hence, it provides better avalanche transfer efficiency and the signal-to-noise ratio. The present RPCs has very fragile gas inlets that can cause cracks by mechanical stress which will result in non-homogeneous gas flow inside the gas gaps. In this new design, this problem will have been solved as well by making them less fragile. Beside extending the trigger coverage and increasing redundancy, the new BI RPCs will provide other benefits:

- The momentum measurement will be possible with a 3-point sagitta measurement by the hits in BI, BM, and BO.
- ϕ coordinate will be measured which is not available in barrel inner MDTs.
- The new time resolution of 0.4 s can be used for searching the long-lived massive particles.

4.1.3. Peformance and Physics

The physics goals for the HL-LHC are more precise measurements for the properties of Higgs boson in its all interactions and more improved measurements of Standard Model (SM) processes and the search for beyond the Standard Model (BSM).

MS plays a crucial role in Physics studies. Hence, it is inevitable to upgrade the detector to cope with the new environment of high event pile-up and expected background brought by HL-LHC. The MS has superior momentum resolution with the help of the new inner tracker (ITk). High efficiency of the trigger and reconstruction is essential for the big data of HL-LHC.

4.1.3.1. Muon Reconstruction Performance. In order to be sure of the success of the HL-LHC, the muon recontruction and identification efficiency, fake rates and momentum resolution must not decrease significantly while operating at a pile-up of $\langle\mu\rangle = 200$. In order to examine the pile-up scenario, $Z \rightarrow \mu + \mu$ decay is used for the simulation where there is not the New Small Wheel (NSW) and the Phase-II upgrades. Pile-up events are passed through the full ATLAS simulation. For the analysis three types of data samples are compared:

- No pile-up ($\langle\mu\rangle = 0$);
- Nominal HL-LHC pile-up ($\langle\mu\rangle = 200$) without the effect of cavern background;
- Nomnal HL-LHC pile-up ($\langle\mu\rangle = 200$) with the effect of cavern background.

The same version of this work is done separately from ATLAS Simulation and our results are broadly compatible with these results above. The details will be discussed in the Chapter 6 BI RPC Performance.

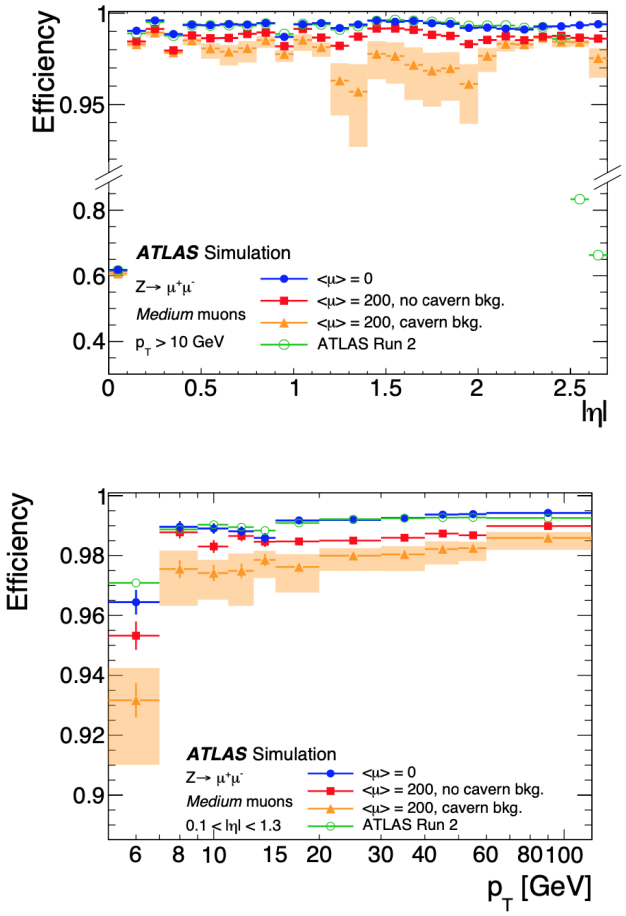

Figure 4.2. Reconstruction and identification efficiency of muons for interaction of $Z \to \mu\mu$ decays as a function of the pseudorapidity for muons with $p_T > 10$ GeV, and as a function of the transverse momentum for muons in the region $0.1 <| \eta |< 1.3$. Three running scenarios are compared: no pile-up (blue circles), $\langle\mu\rangle = 200$ without the effect of cavern background (red squares), and $\langle\mu\rangle = 200$ with cavern background (orange triangles). A shaded area indicates the systematic uncertainty on the amount of simulated cavern background [4].

5. PERFORMANCE STUDIES IN HL-LHC

5.1. Reconstruction Efficiency at HL-LHC

It is crucial to keep the performance efficiency at acceptable level in terms of physics studies when considering the challenging consequences of HL-LHC. To guarantee that the detector performance does not degrade significantly when operating at pile-up of $\langle\mu\rangle = 200$ is main priority for physics studies. In order to do that, performance of the detector in this new environment must be explored in many aspects such as muon reconstruction and identification efficiency, fake rates and momentum resolution. For this analysis, $Z \rightarrow \mu\mu$ interaction and new MS trigger algorithms for upgrade are used in this simulation. 3 different simulated data samples are compared in reconstruction efficiency, η, ϕ, p_t profile and residual. In the plots on this chapter, color of red is corresponding to the muon of a particle gun, blue for muon couples from $Z \rightarrow \mu\mu$ interaction ($\langle\mu\rangle = 0$) and green for muon couples from $Z \rightarrow \mu\mu$ interaction at pile-up ($\langle\mu\rangle = 200$). To make error bars more visible, log scale has been applied to p_t inverse plot and since we could not model the tail of the p_t inverse residual histogram, we fit gaussian only to the core part of it. All plots are normalized for proper comparison between data sets. Number of events for particle gun case is 40000, for $Z \rightarrow \mu\mu$ it is 110000, and for pile-up it is 2000. The reason that error bars are large for pile-up case is that the statistics were low. As we can see from the Figure 5.1, despite the decrease of 10% in reconstruction efficiency at pile-up, reconstruction and identification of muons are in good level for HL-LHC.

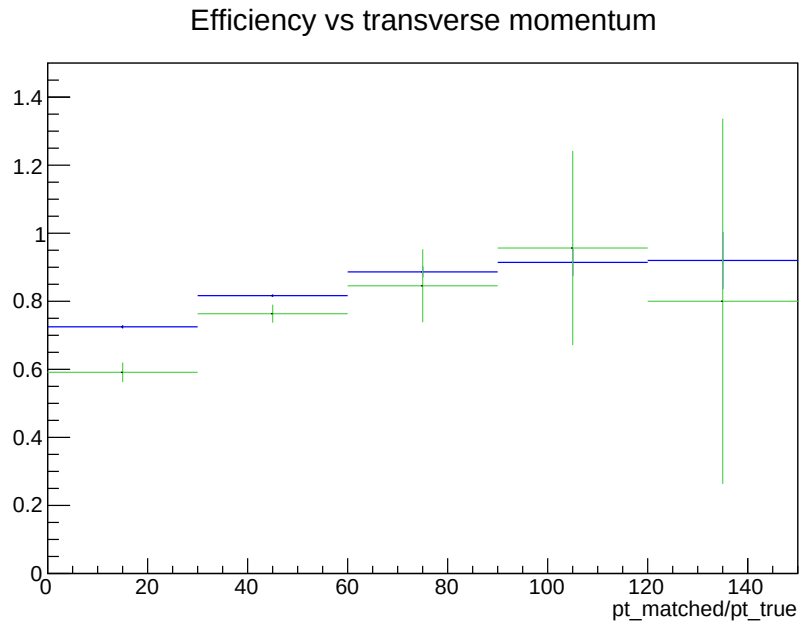

Figure 5.1. p_t dependence of efficiency.

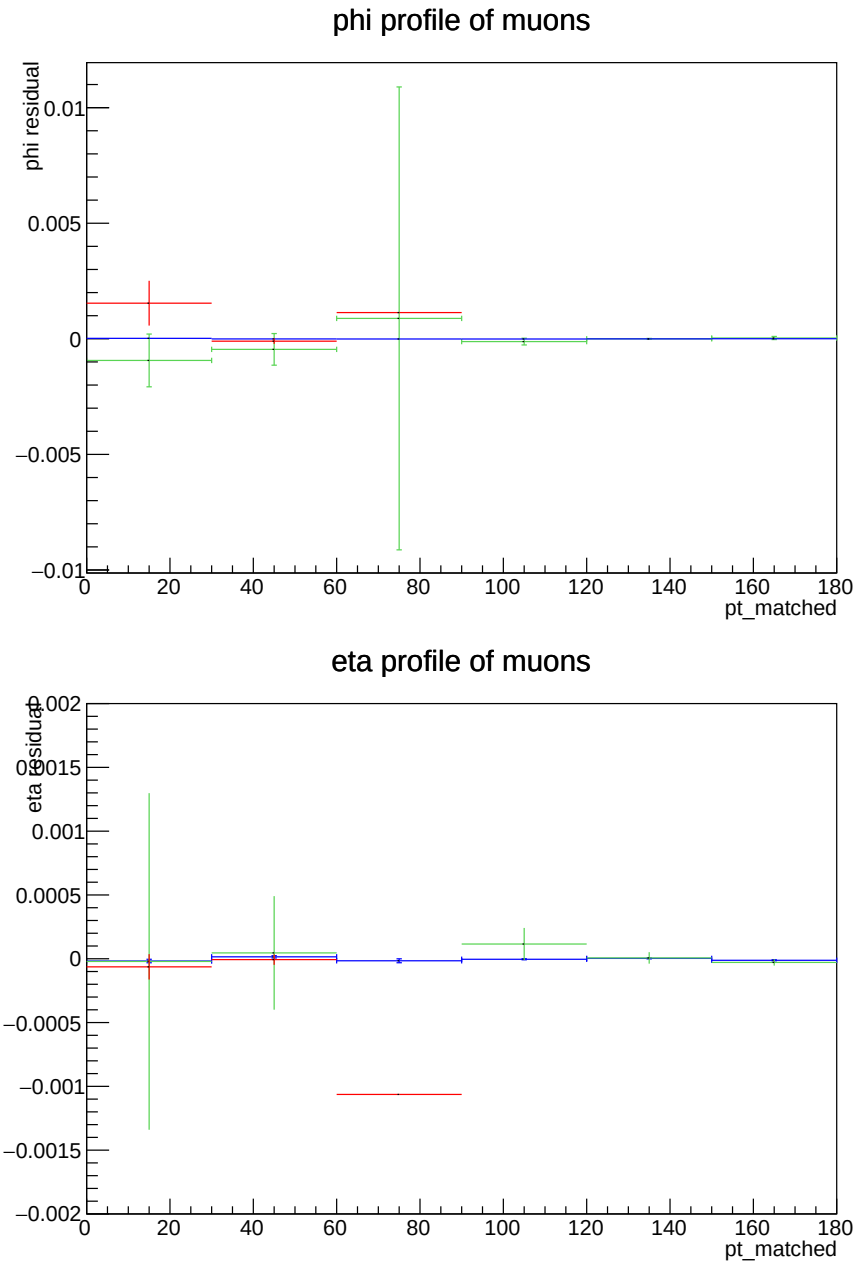

Figure 5.2. η and ϕ profile of muons.

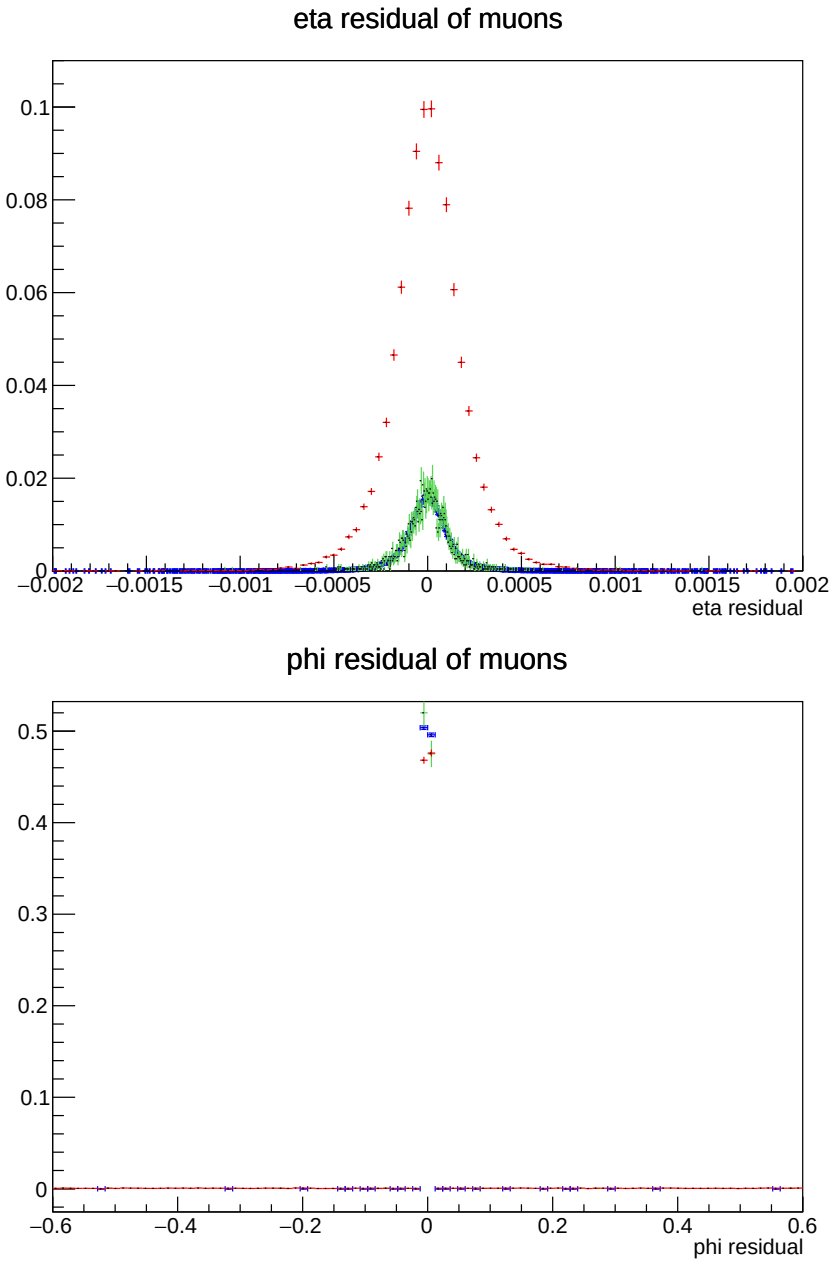

Figure 5.3. η and ϕ residual of muons.

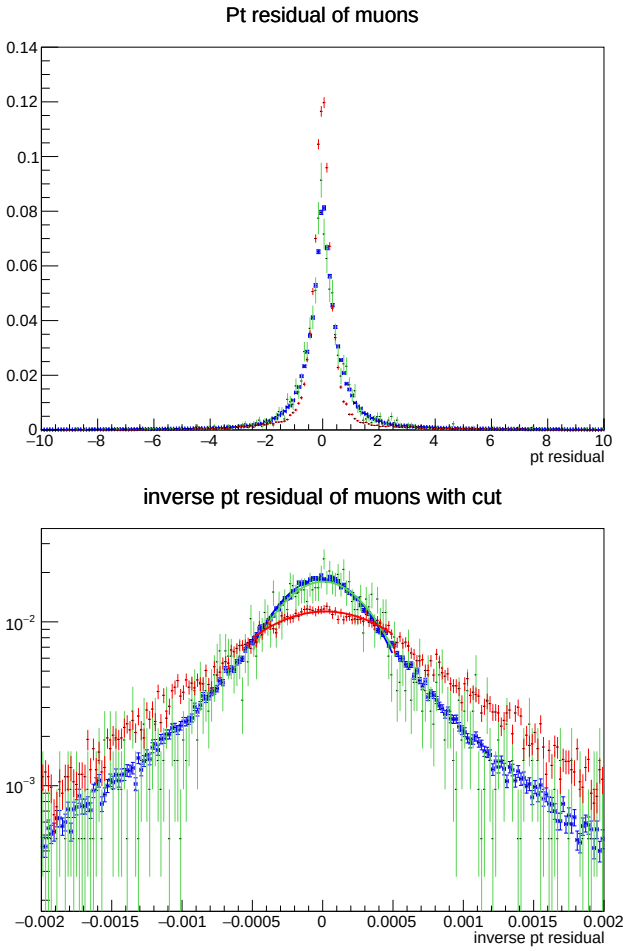

Figure 5.4. p_t residual of muons and inverse p_t residual of muons with cut.

6. BI RPC PERFORMANCE STUDIES

6.1. RPC Trigger Efficiency

As we discussed in Chapter 4, it is essential that the BI systems extend the trigger coverage and enhance the trigger efficiency for HL-LHC. The upgraded system will provide a different trigger scheme and in this chapter, we will test these trigger systems in the new environment of HL-LHC. In order to do that, 3 different simulated data samples will be compared for different trigger schemes. Number of events for the $Z \rightarrow \mu\mu$ is 110000, for the pile-up it is 64750 and for the pile-up with cavern background it is 31625. The colors on the plots: Blue for the $Z \rightarrow \mu\mu$, the green for the pile-up and the pink for the pile-up with cavern background.

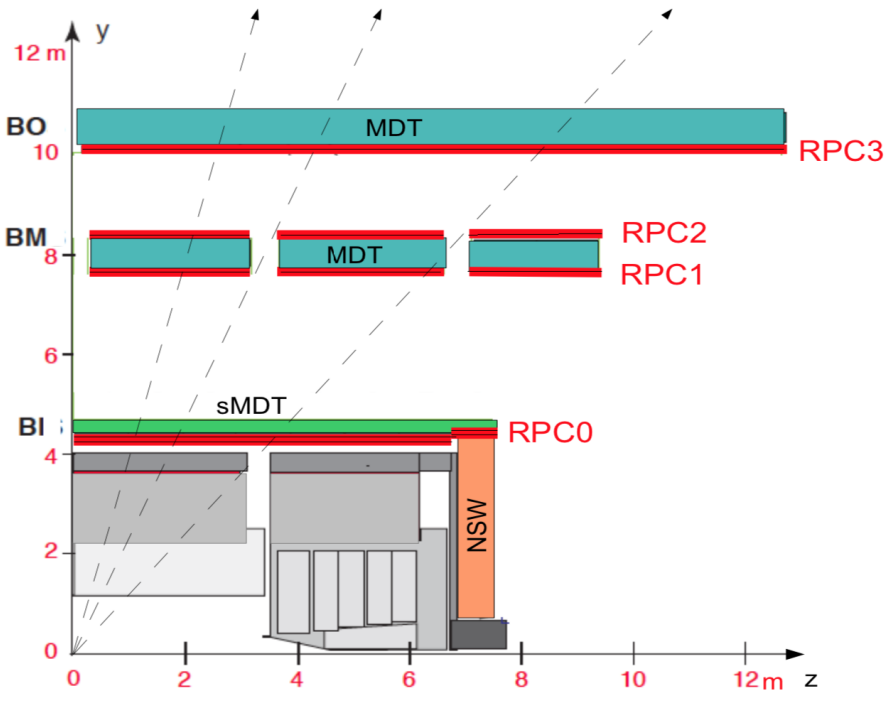

Figure 6.1. Transverse section of a small sector in the barrel region [4].

We explored many possibilities that efficiency may depend on: Pile-up, existence of certain chambers, quality and threshold. The different trigger schemes (see Table 6.1) are based on which RPC planes are taken account while operating.

- 3/3 Chambers: Hits in at least three out of four planes of the RPC1+RPC2 chambers and in at least one out of two planes of RPC3. This is equivalent to the present high-pt trigger [4].
- 3/4 Chambers: The previous requirement in a logical OR with the requirement of hits in at least two planes out of three in RPC0 and in at least three planes out of six in RPC1+RPC2+RPC3. In this way, all combinations of three-chamber coincidences are accepted.
- 3/4 Chambers + BI-BO: The previous requirement in a logical OR with the requirement of at least two hits in RPC0 and at least one hit in RPC3. This enhances the trigger covarage in the regions where no BM RPCs are installed due to the mechanical support structure of the toroid coils. The BI-BO coincidence is expected to be prone to accidental coincidences of uncorrelated background hits that are negligible in three-chamber coincidences. In the baseline version of this trigger, BI-BO coincidences are used in the whole barrel region, but can be limited to the BM acceptance gaps, if the muon trigger in the barrel gets too high.

Quality	Trigger	Requirement
0	3/3 Chambers	3[RPC1+RPC2]+1[RPC3]
1	3/3 Chambers + BIBO	3[RPC1+RPC2]+1[RPC3] OR (2[RPC0] AND 3[RPC1+RPC2+RPC3]) OR (2[RPC0] AND 1[RPC3])
2	3/4 Chambers	3[RPC1+RPC2]+1[RPC3] OR (2[RPC0] AND 3[RPC1+RPC2+RPC3])

Table 6.1. Quality and their corresponding trigger schemes.

In order to see the effect of new trigger scheme in Muon Spectrometer, some properties that will indicate these different trigger systems are defined in analysis

framework. Hence, pile-up dependence and trigger system effect is seen through this analysis. These properties are *ThrValue* and *Quality*. *ThrValue (Threshold)* contains 2 value separating muons as $p_t < 10$ GeV and $p_t > 20$ GeV as 1 and 2. *Quality* indicates which trigger scheme is used such that in Table 6.1. To grasp the physical meaning of *Quality* property, its dependence to η and ϕ values is explored through these plots in Figure 6.2. For this analysis, 2D colored histogram method is used. Same procedure is applied for *ThrValue (Threshold)* property and the correlation between *ThrValue (Threshold)* and *Quality* are explored. This can be seen in Figure 6.3.

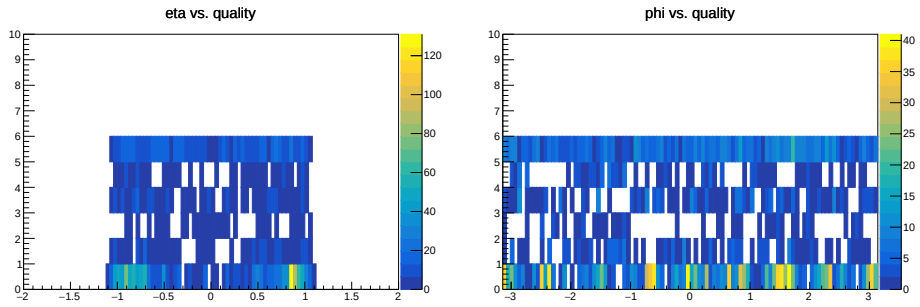

Figure 6.2. 2D colored histogram of η and ϕ versus quality values.

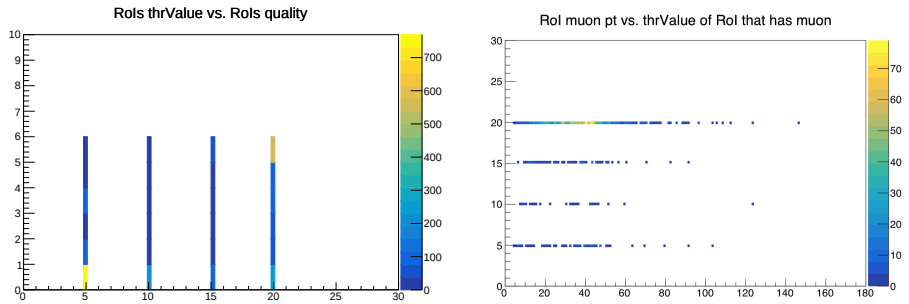

Figure 6.3. 2D colored histrogram of ThrValue versus quality and RoI muon pt and thrValue of RoI that has muon.

6.1.1. Performance Dependence on Pile-up

3 different data samples and different trigger systems are used for this analysis. In order to see RPC trigger performance on Pile-up, RPC Trigger efficiency is plotted

for every combination of *Threshold* and *Quality* properties. There is a 3% decrease in efficiency in the plots in Figure 6.4. But this decrease is normal when we consider the uncertainty of simulated cavern background affect. As it can be seen from the plots of Figure 6.4, the efficiency increased with BI RPCs.

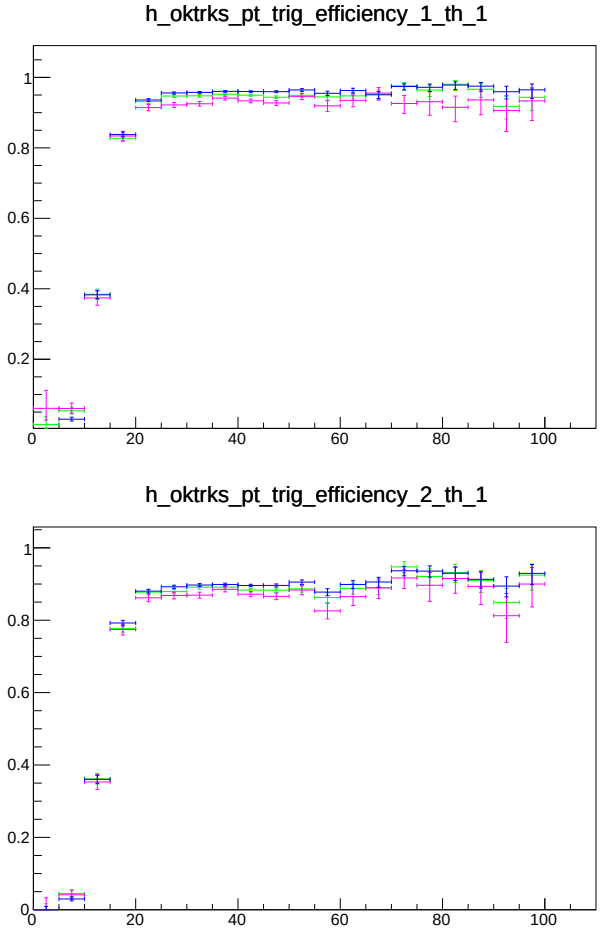

Figure 6.4. P_t dependence of trigger efficiency to the pile-up and trigger algorithms.

7. BIS78: UPGRADED ATLAS MS SIMULATION

7.1. BIS78 Geometry Implementation

Current barrel Muon System of ATLAS contains 3 RPC chambers, in the radius of approximately 6, 8 and 10 meters and in the range of $|\eta| < 1.0$. In Figure 7.2, new MS and RPC chamber that will be added in barrel inner region can be seen. For Phase-II Upgrade, new chambers will be added to the current Muon System, in the radius of 4.4 meters and in the range of $1.0 < |\eta| < 1.3$, which is BIS78. With HL-LHC, the number of particles will increase with the same amount of luminosity and there will be huge amount of information that the current MS trigger system cannot handle. Therefore, BIS78 will be playing a critical role for the upgrade as extending the trigger coverage, providing better pt resolution and time resolution. In order to test the new environment, full simulation of the new geometry is essential. For full Athena Simulation, new sectors must be described in ATLAS Muon Detector Description Database (AMDB), uploaded to the ATLAS Oracle Database and necessary updates must be done in Athena, main software framework of ATLAS, for new sectors to work in simulation. Specifically, the modifications corresponding to the new geometry must be done in Athena *MuonSpectrometer/MuonGeoModel* package.

7.2. PERSINT

For the following work of visualisation of the new geometry, Persint [6] program is used. Persint is an interactive visualization program developed for ATLAS. The main purposes of this program can be listed as,

- Designing the Muon Spectrometer.
- Resolving the possible anomalies by the MuonGeoModel which is a package forming the MS geometry in the simulation.
- Optimization of reconstruction software.

- Analyzing the collision events.
- Analyzing cosmic ray data in the commissioning phase.

Persint is a very versatile program when one needs to visualise the events in the most detailed way. It can be operated in Linux, MacOS and Windows. It is interfaced with Athena. Persint is a well-suited program in the cases where the visual representation of the detector response is crucial in order to understand the complicated events. Pesint is designed for the 3D representation of the objects. It visualises the detector geometry with the information provided by the AMDB. Persint works with many fully interaction applications. These application contain visualisation of active detector elements, passive material, magnetic field map, detection of the volume clashes and the display of event's hits. Even one can display the reconstructed events by the any reconstruction program in Athena. Beside that, *MuonBoy* embedded in Persint can be used for reconstruction. The default representation in Persint is 3D. However, one can visualise the 2D projections to the desired axis to focus on the particular part of the detector. It is possible to use translation, zoom and rotation as well to change the viewpoint. The remarkable features of Persint can be summarized as:

- Three dimensional representation of the objects in full volume or wire mode.
- Display of event's hits and its reconstruction.
- Spatial navigation with real time displacement.
- Displays can be exported as .png, .jpg, .bmp, or .svg files.
- Detection of clashing volumes.
- Boolean volume operations (addition, subtraction, intersection).
- Display the magnetic field map and generate muons and track in the magnetic field.
- Distribution of material along tracks.
- Vertex display.
- The calculation of invariant mass.
- Display of jets and missing E_T vector.

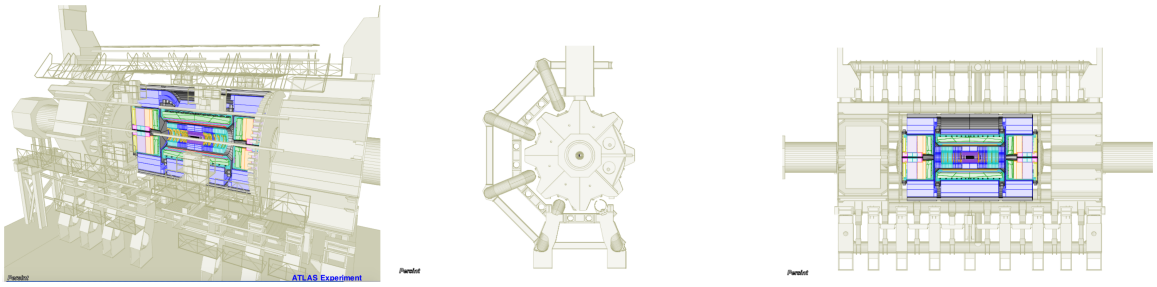

Figure 7.1. Various views of Persint [6].

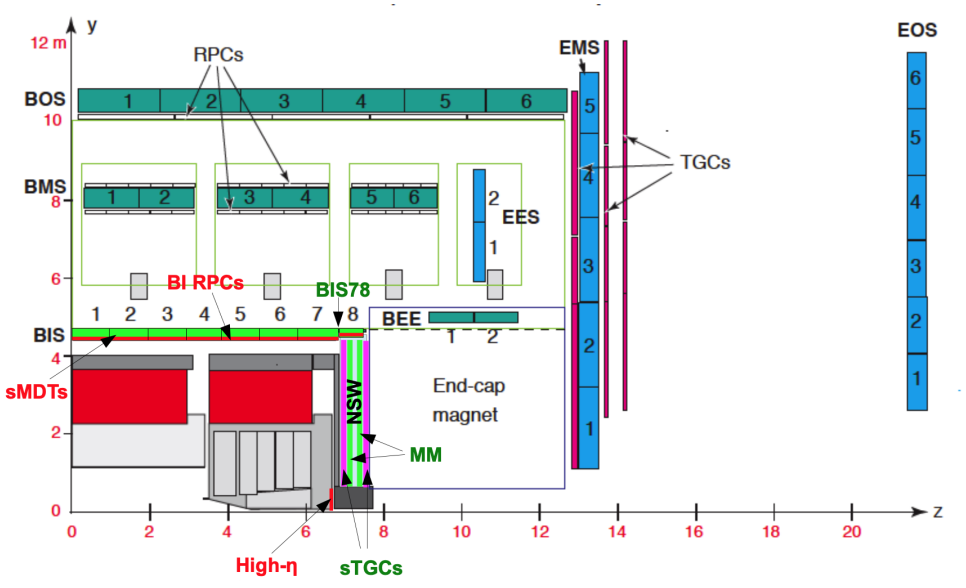

Figure 7.2. Upgraded cross-sectional view of Muon System [4].

7.3. AMDB

The ATLAS Muon Spectrometer Detector Description Database (AMDB) [7] is an object-oriented language that is used to describe the Muon Spectrometer geometry for simulation. It has a flat file organization where each line has numbers describing the geometry of the detector. Symmetries inherited from the Muon Spectrometer geometry exist inside of it to compactify the code. The AMDB file is a part of *amdb-simrec/amdcsimrec* software package which is describing the detector geometry taking symmetries and conventions into account. The AMDB description is mainly separated into two parts: the description of active elements (detectors) and passive elements (dead matter such as magnets and support structure). The description of active elements is object-oriented. It has a geometry tree organisation. Stations are at the top level of this tree. The Stations are formed as a collection of objects whose technology can be varied with the basic shape of trapezoid and they can be customized according to the one's needs by cutout description. The inner structure described can be passed through these stations. Then, copies of these stations are positioned and aligned in the AMDB axis. The quantities in AMDB are in mm.

7.3.1. The Axis System in AMDB

The global axis system in AMDB is the same as the ATLAS axis system. The local coordinate system is used for defining the objects and the orientation in the global axis can be seen in Figure 7.3. The local coordinate orientation is different in the Barrel, End Cap A and End Cap C regions (see Figure 7.4). s-z-t local coordinate system orientation is shown in the figures. However for the convenience, in the following sections dealing with the geometry design, x-y-z local coordinate system will be used instead of s-z-t. s corresponds to the x, y for z and z for t, this correspondence can easily be seen in Figure 7.6.

AMDB file has different parts to describe the different properties of the stations. The basic parts to describe the main properties of the stations are: W,D,P,H,M,E,N,

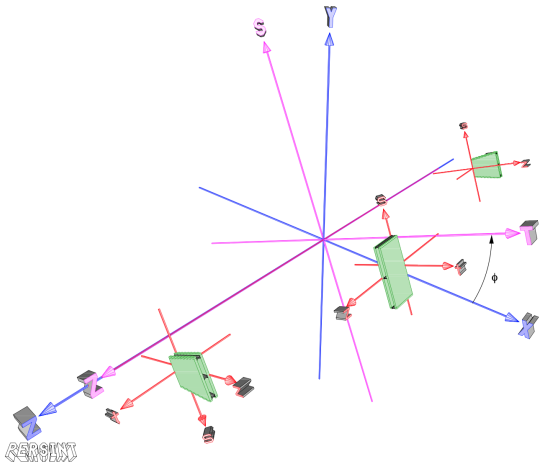

Figure 7.3. Three axis systems in AMDB [6].

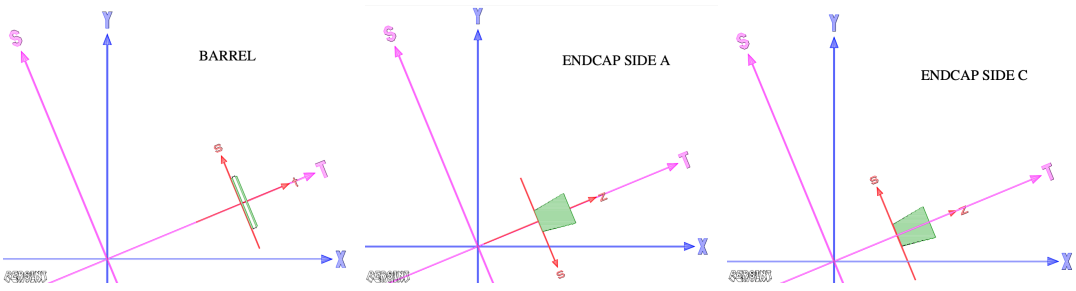

Figure 7.4. Barrel and End Caps local axis systems in AMDB [6].

V,A,B,C,R,X. These are the all entries of AMDB. The entries of D,H,P and W will be focused since they are the most basic entries to define a detector geometry.

7.3.2. Creating the Stations

The general scheme of D entries can be seen in Figure 7.16. This is the part where we determine the type of station, the technology of the object needed and describe the dimensions of envelopes of these objects. The parameters describing the geometry can be seen in Figure 7.6. There are five basic technologies: MDT, RPC, TGC, DED, SPA. Basic shapes to create certain technologies can be seen in Figure 7.7.

```
*-- Definition of stations ------------------------------------------------------
* Typ I  No
*   s     z      t    Io Tec i    sh  W_xS    W_xL     L_y     Ex     D1     D2     D3
*
D BIL 1   7
   0.     0.     0.    1 MDT 1       2671.5  2671.5 1081.261   0.    55.     0.     0.
-1280.    0.   123.03 2 CHV 1          6.0     6.0 1081.261   0.     0.     0.     0.
   0.     0.   123.03 3 CMI 1          6.0     6.0 1081.261   0.     0.     0.     0.
1280.     0.   123.03 4 CRO 1          6.0     6.0 1081.261   0.     0.     0.     0.
   0.   240.   208.03 5 LB  1       2620.0  2620.0    50.     0.     0.     0.     0.
   0.   840.   208.03 6 LB  1       2620.0  2620.0    50.     0.     0.     0.     0.
   0.     0.   293.03 7 MDT 2       2671.5  2671.5 1081.261   0.    55.     0.     0.
```

Figure 7.5. AMDB D entries [7].

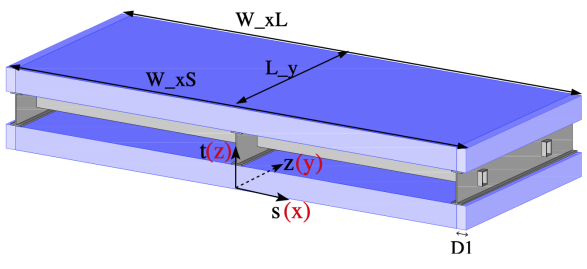

Figure 7.6. D entry parameters and the local coordinates [7].

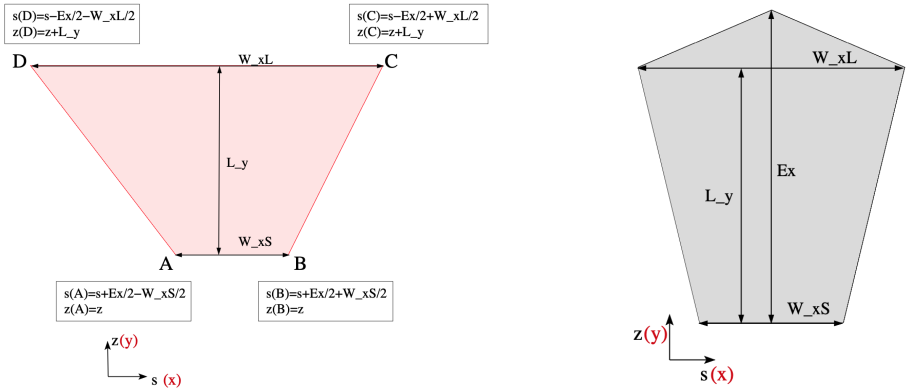

Figure 7.7. Basic shapes of the object with technology MDT, RPC, TGC, SUP, SPA and CSC [7].

7.3.3. Cutout Description

H entries are responsible for the cutout description of AMDB. This is the part where one can use in order to create special type of shapes. The description of cutout in the AMDB can be seen in Figure 7.8 and the parameters to determine the dimension of the pieces that will be cut can be seen in Figure 7.9.

7.3.4. Grand Global Positioning

Once creating a station, it needs to be positioned in the global coordinate in the ATLAS. P entries do this job by determining the R and Z coordinates, and in which octant the sector will be placed. Even one can determine the orientation of the station around its center of mass via the parameters of α, β, γ. The global positioning can be described in the AMDB such as Figure 7.10. The parameter of *Iphi* indicates in which octant the particular sector will placed and *Jgeo* indicates whether the sector has a mirror symmetry in the Z axis or not. Which cutout description will be used can be determined via *Jcut* parameter as well.

```
*-- Definition of BOS stations -------------------------------------------------
* Typ I  No
*  dx     dy     dz  Io Tec i x y s  W_xS    W_xL     L_y     Ex     D1     D2
* ...
D BOS 1  10
   0.     0.     7.00 1 SUP 1       3660.   3660.      0.     0.     0.     0.
   0.     0.     7.00 2 DED 1       3660.   3660.   1046.     0.     0.     0.
   0.  1050.     7.00 3 RPC15       3660.   3660.    870.     0.     8.   120.
   0.  1046.     7.00 4 SUP 3       3660.   3660.      0.     0.     0.     0.
   0.     0.    57.00 5 RPC13    -1 3660.   3660.   1110.     0.     8.   120.
   0.  1114.    53.00 6 DED 1       3660.   3660.    806.     0.     0.     0.
   0.  1920.     7.00 7 SUP 2       3660.   3660.      0.     0.     0.     0.
   0.     0.   135.00 8 MDT 1       3773.3  3773.3  1920.     0.    55.     0.
   0.     0.   232.02 9 SPA 4       3773.3  3773.3  1920.     0.     0.     0.
   0.     0.   549.0210 MDT 2       3773.3  3773.3  1920.     0.    55.     0.
H BOS 1 1 4
1045.   630.          2              140.0   140.0   200.00   0.    49.7
1045.   684.2         5              140.0   140.0   200.00   0.    49.7
1451.7  824.3         8              870.0   870.0   123.75   0.    49.7
1451.7 1295.3        10              870.0   870.0   123.75   0.    49.7
*
*-- Positioning of BOS stations ---------------------------------------------
*    Jgeo   Iphi     <-------- Translation (mm) ------->&lt;--- Rotation (Deg) --->
* Typ |Jcut   |    Jzz   dPhi       Z        T       S     Alpha   Beta    Gamma
*  |  | |     |      |      |       |        |       |      /t      /z      /s
*  |  | | --------  |      |       |        |       |       |       |       |
P BOS 1 1 11111001  6    22.5  10910.   10153.48    0.      0.      0.      0.
*
```

Figure 7.8. General scheme of creating a station with cutout description [7].

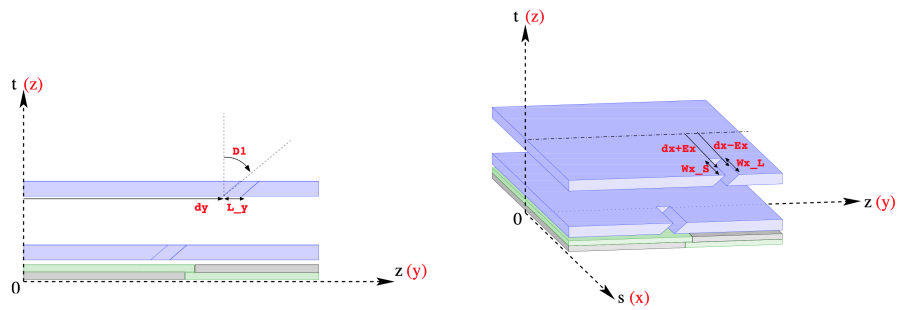

Figure 7.9. Parameters of cutout description [7].

```
*-- Positioning of BIL stations -------------------------------------------------
*    Jgeo   Iphi     <-------- Translation (mm) ------->&lt;--- Rotation (Deg) --->
* Typ |Jcut   |    Jzz   dPhi       Z        T       S     Alpha   Beta    Gamma
*  |  | |     |      |      |       |        |       |      /t      /z      /s
*  |  | | --------  |      |       |        |       |       |       |       |
P BIL 2   11200000  1     0.     330.    4740.96    0.      0.      0.      0.
```

Figure 7.10. AMDB P entries [7].

7.3.5. Inner Structure Description

One of the crucial parts is W entries which are responsible for inner structure of the objects such as RPC since it describes the detector materials such as strips. The structure of W entries can be varied in different technologies.

```
* matteo BIS7 TEST
W RPC26 .110 2 2
 27.07    27.2     2.                ! pitch (s_phi,z_eta) / dead separation
   64      40                        ! n readout strips (s-phi,z_eta)
 45.715   37.85    1.                ! strip offset(s-phi,z_eta)/ dead separation
    1       1                        ! nber of (s) strips readouts/ nber of (s) gas gaps
* matteo BIS7 (short) TEST
W RPC27 .110 2 2
  27.07    28.09    2.               ! pitch (s_phi,z_eta) / dead separation
   64      32                        ! n readout strips (s-phi,z_eta)
  45.715   37.63    1.               ! strip offset(s-phi,z_eta)/ dead separation
    1       1                        ! nber of (s) strips readouts/ nber of (s) gas gaps
* matteo BIS8 TEST
W RPC28 .110 2 2
   27.07   21.81    2.               ! pitch (s_phi,z_eta) / dead separation
   64      16                        ! n readout strips (s-phi,z_eta)
   26.996  37.64    1.               ! strip offset(s-phi,z_eta)/ dead separation
    1       1                        ! nber of (s) strips readouts/ nber of (s) gas gaps
*
W RPC29 .110 2 2
  25.2     21.81    2.               ! pitch (s_phi,z_eta) / dead separation
   64      16                        ! n readout strips (s-phi,z_eta)
   45.8    37.64    1.               ! strip offset(s-phi,z_eta)/ dead separation
    1       1                        ! nber of (s) strips readouts/ nber of (s) gas gaps
```

Figure 7.11. W entries of AMDB for RPC.

7.4. New Geometry Design in AMDB

The comparison between current Barrel Inner and new Barrel Inner regions can be seen in Figure 7.12. The red pieces indicate the new RPCs that will be added into barrel inner region and purple pieces indicate the MDTs. The new geometry BIS78 is designed by Daniel Soyk and the BIS78 drawings of total 16 sectors to be implemented are shared in order to describe the new sectors in AMDB. The inner structure of all type of new RPCs is provided via drawing as well. The detailed description of new geometry drawings can be seen in Figure 7.13.

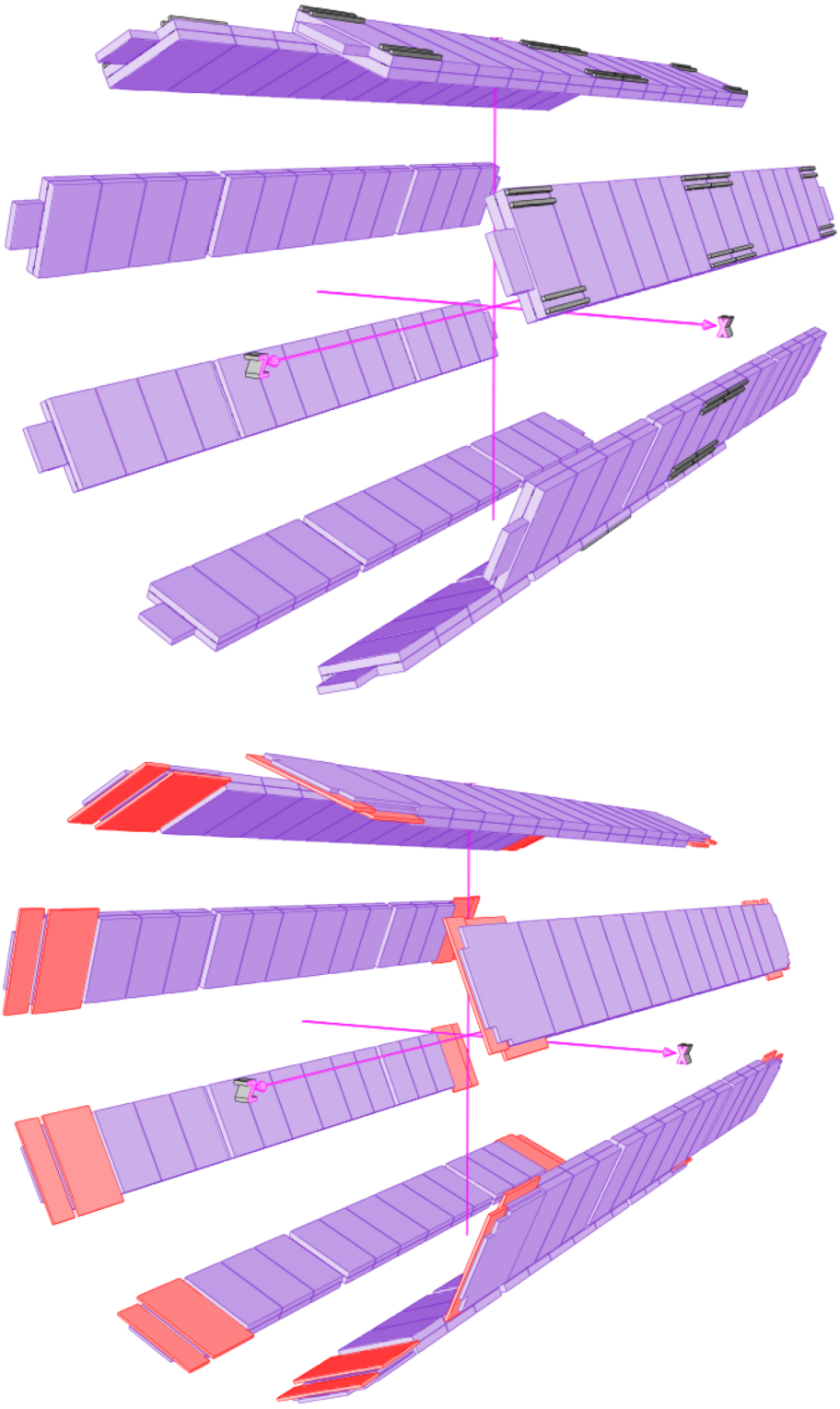

Figure 7.12. Longitudinal view of current BIS and new BIS chambers via Persint.

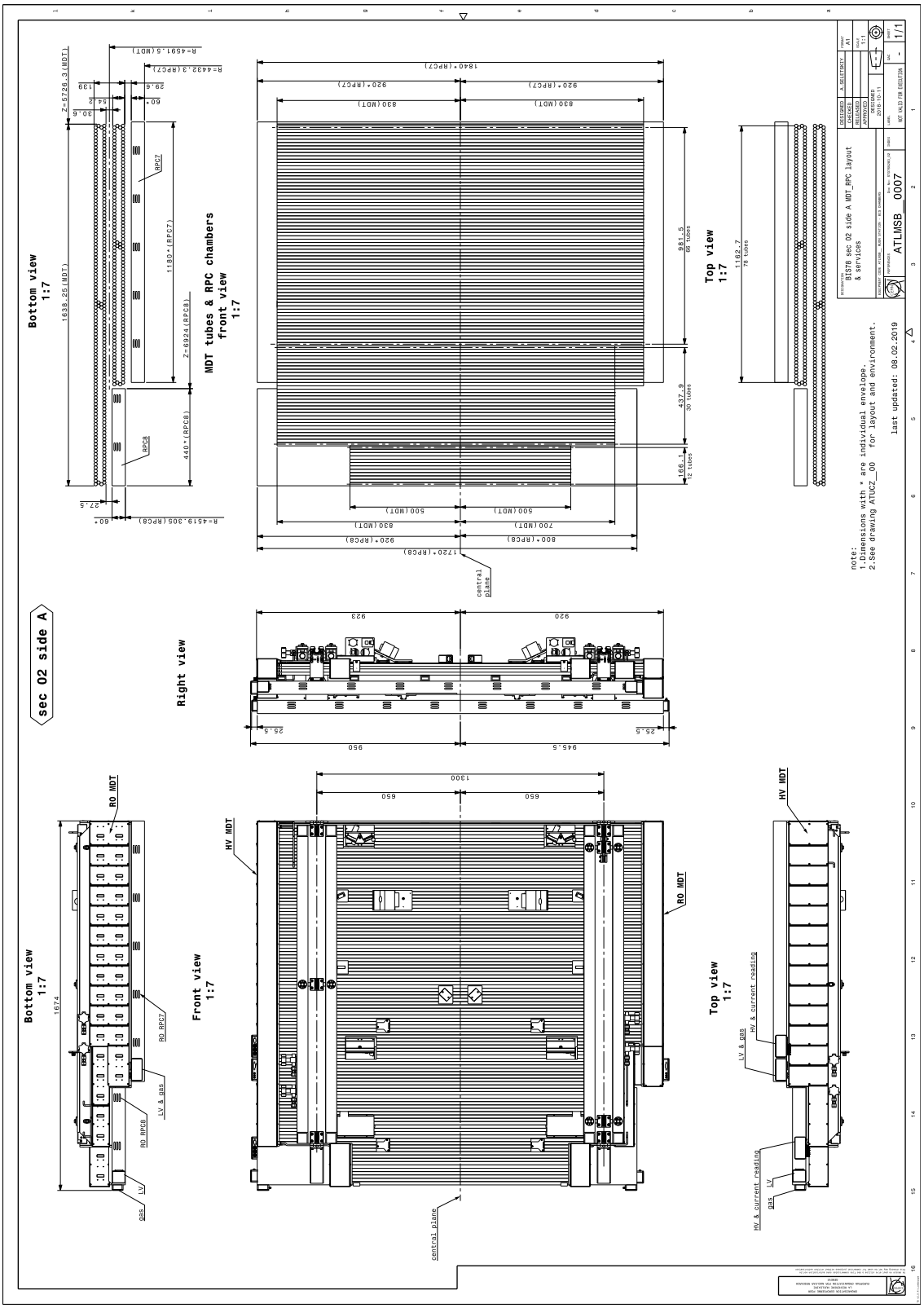

Figure 7.13. Drawing of BIS78 sector for the first octant side A.

7.5. Forming the Stations

In order to understand the axis system in the drawings, one BIS78 sector is visualized via Persint as in Figure 7.14. The parameters in D entries as W_xS, W_xL, L_y, L_x of AMDB in order to create a basic shape of trapezoid are already determined in the drawings as it can be seen in Figure 7.15. Therefore, these objects in BIS stations were created by implementing the quantities of these D entry parameters in AMDB such that in Figure 7.16.

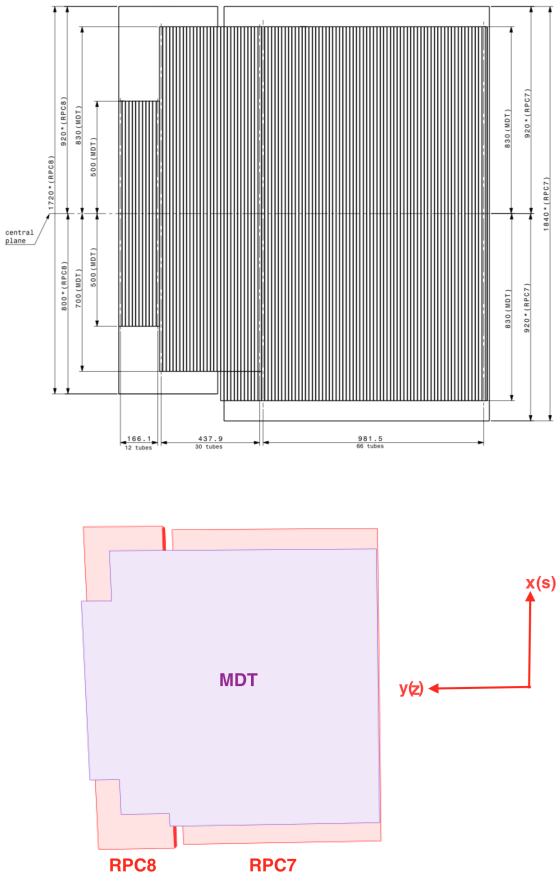

Figure 7.14. Visualization of MDT Tubes & RPC Chambers Front View for the first octant side A in Persint.

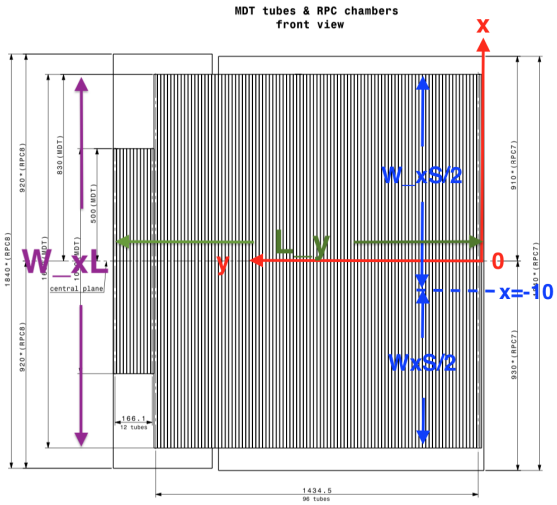

Figure 7.15. Corresponding D entry parameters in the drawing.

```
D BIS11   4                                  W_xS   W_xL   L_y     Ex    D1    D2
x 15.    y 0.  z 145.32 1 MDT 9             1630.0 1630.0  981.5   0.    0.    0.
  15.      0.    230.32 2 MDT 9             1630.0 1630.0 1457.1   0.    0.    0.
  35.    -12.     57.00 3 RPC26             1840.0 1840.0 1000.    0.    0.    0.
  60.   1017.    154.50 4 RPC28             1720.0 1720.0  440.    0.    0.    0.
```

Figure 7.16. AMDB D entries of one sector in the drawing.

7.6. Forming Relative Positions of the Objects in One Station

The local coordinates which are determining the relative position of objects in one station must be extracted from the other parameters determined in the drawings since they are not explicitly determined. As we can see it from Figure 7.17 we can apply the formula below to find the local coordinates. The local x values correspond to the offset from the central plane of the center of mass of the object. After determining the x,y,z parameters of D entries, the local coordinates are implemented into the AMDB accordingly.

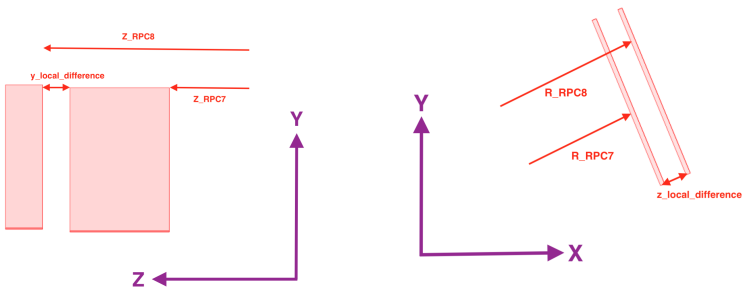

Figure 7.17. Illustrations of local y and z values difference between two objects.

We can find the local coordinates such that,

$$z_{\text{local-difference}} = R_{\text{object2}} - R_{\text{object1}} \tag{7.1}$$

$$y_{\text{local-difference}} = Z_{\text{object2}} - Z_{\text{object1}} \tag{7.2}$$

7.7. Global Positioning of the Chamber

Having created the BIS78 sectors, they must be placed in the ATLAS detector. In order to do that, P entries of AMDB positioning the sectors in the global coordinate will be used. For the global position of the chamber, it is determined by R and Z parameters in the drawings as it can be seen from Figure 7.18. These P entry parameters in the

drawings are implemented in AMDB in order to place the chambers in ATLAS detector as in Figure 7.10.

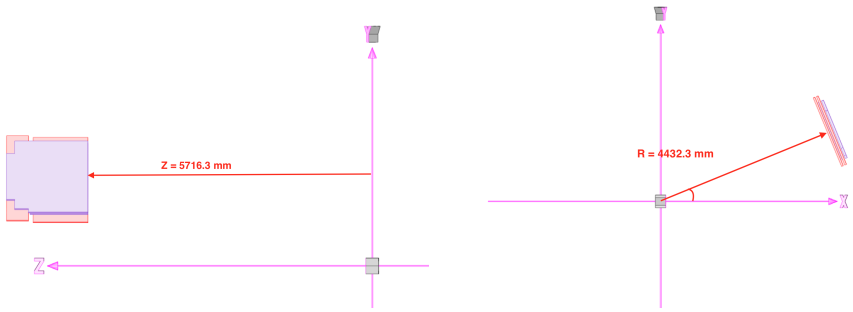

Figure 7.18. Example of one sector global positioning in Persint.

* Typ	I	C	Iphi	Iz	dPhi	Z	R	S	Alfa	Beta	Gamma	
P BIS	7	1	10000000	7	22.5	5716.3	4432.3	0.	0.	0.	0.	-6791.051
P BIS13	1	1	01000000	7	22.5	5716.3	4432.	0.	0.	0.	0.	-6791.051
P BIS 9	1	1	00100000	7	22.5	5716.3	4432.	0.	0.	0.	0.	-6791.051
P BIS10	1	1	00010000	7	22.5	5897.5	4432.3	0.	0.	0.	0.	-6791.051
P BIS 8	1	1	00001000	7	22.5	5897.5	4447.3	0.	0.	0.	0.	-6791.051
P BIS11	1	1	00000100	7	22.5	5897.5	4432.3	0.	0.	0.	0.	-6791.051
P BIS12	1	1	00000010	7	22.5	5897.5	4432.3	0.	0.	0.	0.	-6791.051
P BIS16	1	1	00000001	7	22.5	5897.5	4447.	0.	0.	0.	0.	-6791.051

Figure 7.19. Implementation of position parameters into AMDB.

Parameters in Global Positioning:

- Typ It : Station type.
- Icut : Cut-out index (no cut-out if missing).
- Iphi : Indicates in which of the 8 octants, a station of this type is to be positioned.
- Iz : Index identifying the Z (for Barrel) or R (for End-Caps) position of the station. For the negative Z locations, these indexes are negative.
- dPhi : Relative Phi position of the station in its octant.
- Z : Z position of the lowest Z edge of the station.
- R : Radial position of its innermost edge.
- S : Ortho-radial position of the center of the station.

- Alfa, Beta, Gamma : Three angles defining the deviations from the nominal orientation of the station.

7.8. Basic Shapes in the Drawings

There are different types of shapes for RPCs and MDTs in the drawings as they can be seen from Figure 7.20 and Figure 7.21.

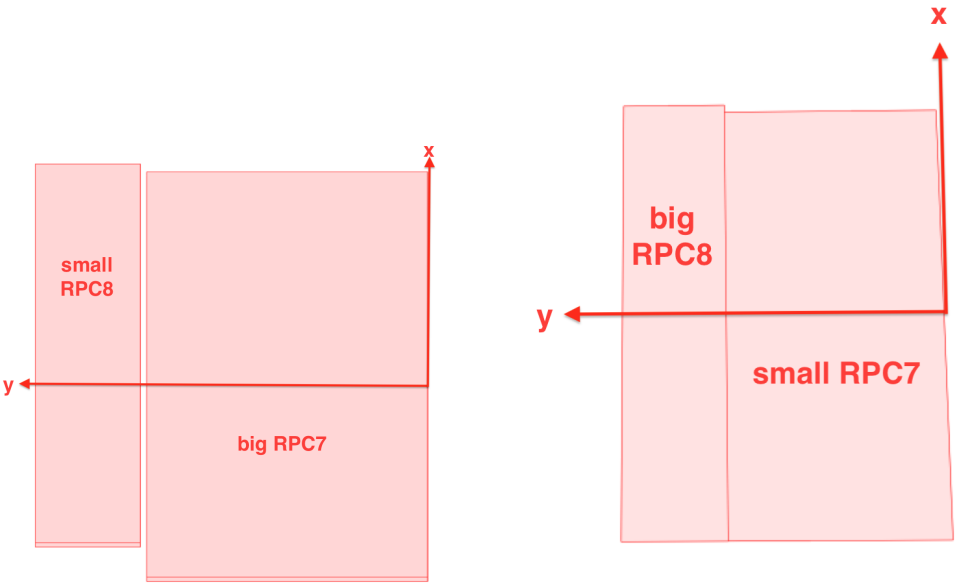

Figure 7.20. Basic shapes of RPCs in BIS78.

In order to form MDT shapes, cut-out description of AMDB (H entries) is used such that the dimensions of pieces that will be taken of are determined and these pieces are formed such that in Figure 7.22. Therefore, we have the exact shapes for Top MDTs and it is implemented in AMDB as in Figure 7.23. All sectors for BIS78 are described in AMDB. The parameters in the drawings, L_y, W_xS, W_xL and local x, y and z values are implemented in AMDB and R and Z values determining the global positioning are implemented, as well. To match with parameters in BIS78 design, a new type of station is defined for every sector.

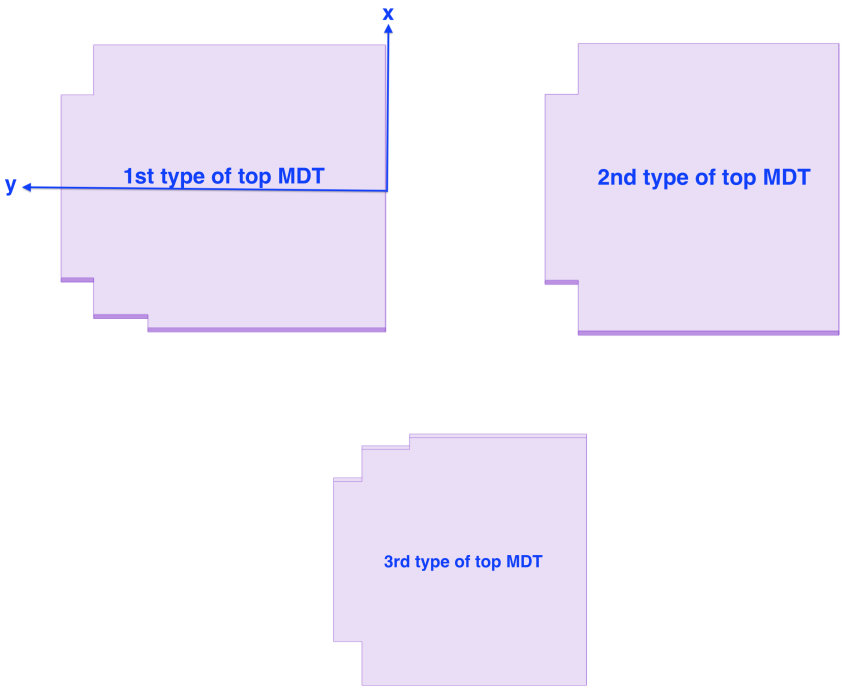

Figure 7.21. Basic shapes of Top MDTs in BIS78.

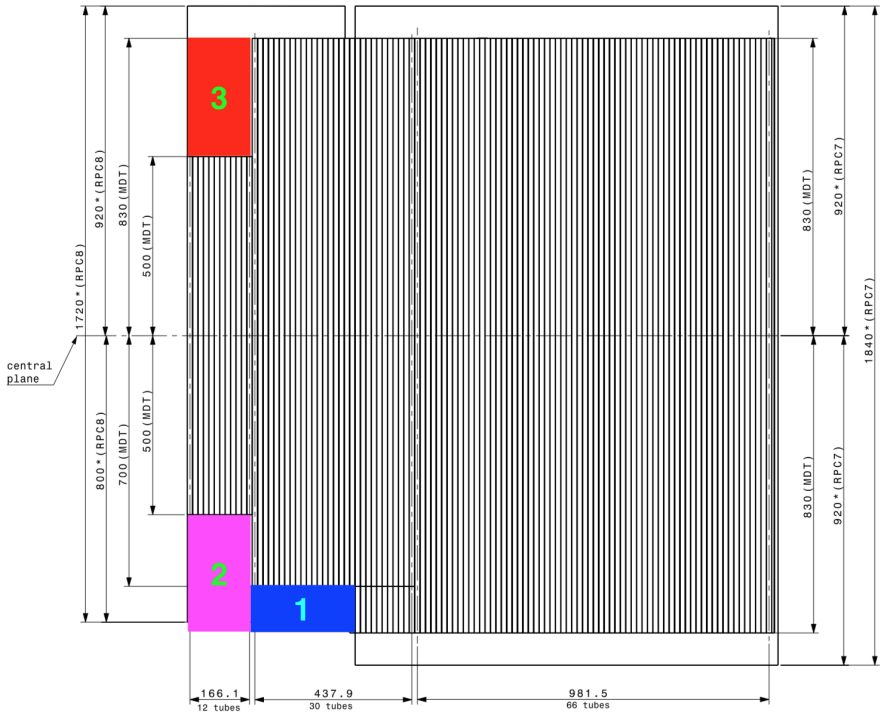

Figure 7.22. Illustration of formation of cut-out pieces.

```
# BIS 7 1 4
-765.x 1198.3 y  1
-665.   1472.2   2
 665.   1472.2   3
-860.     0.

 2
 2  object number with cut
 2
 4

          W_xS    W_xL    L_y
130.0   130.0   440.0   0.   0.
330.0   330.0   166.1   0.   0.
330.0   330.0   166.1   0.   0.
120.0   120.0   440.0   0.   0.
```

Figure 7.23. Implementation of cut-out parameters to AMDB.

7.9. Inner Structure Design of RPCs

In Phase-II Upgrade, RPC structure has been undergone through many changes. One of the main modifications is increasing the layer numbers from 2 to 3 and this will enhance the position resolution. Beside the layer numbers, many inner structure parameters i.e. number of strips, pitches, strip positioning will be changed. The details of new design for RPCs inner structure can be seen in Figure 7.25. Parameters generally can be defined for η and ϕ strips separately as in Figure 7.24. The parameters of inner structure are indicated in the drawings. These parameters meaning can be seen in the following figures. According to these definitions, W entries are implemented in AMDB for each different RPC types as in Figure 7.11.

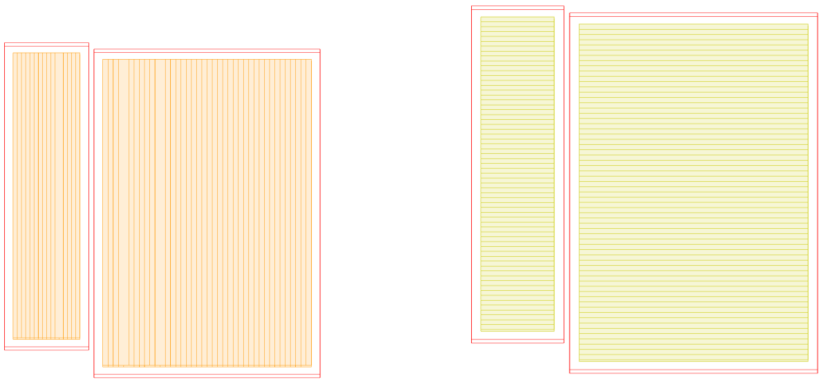

Figure 7.24. η and ϕ strips in BIS78 RPCs.

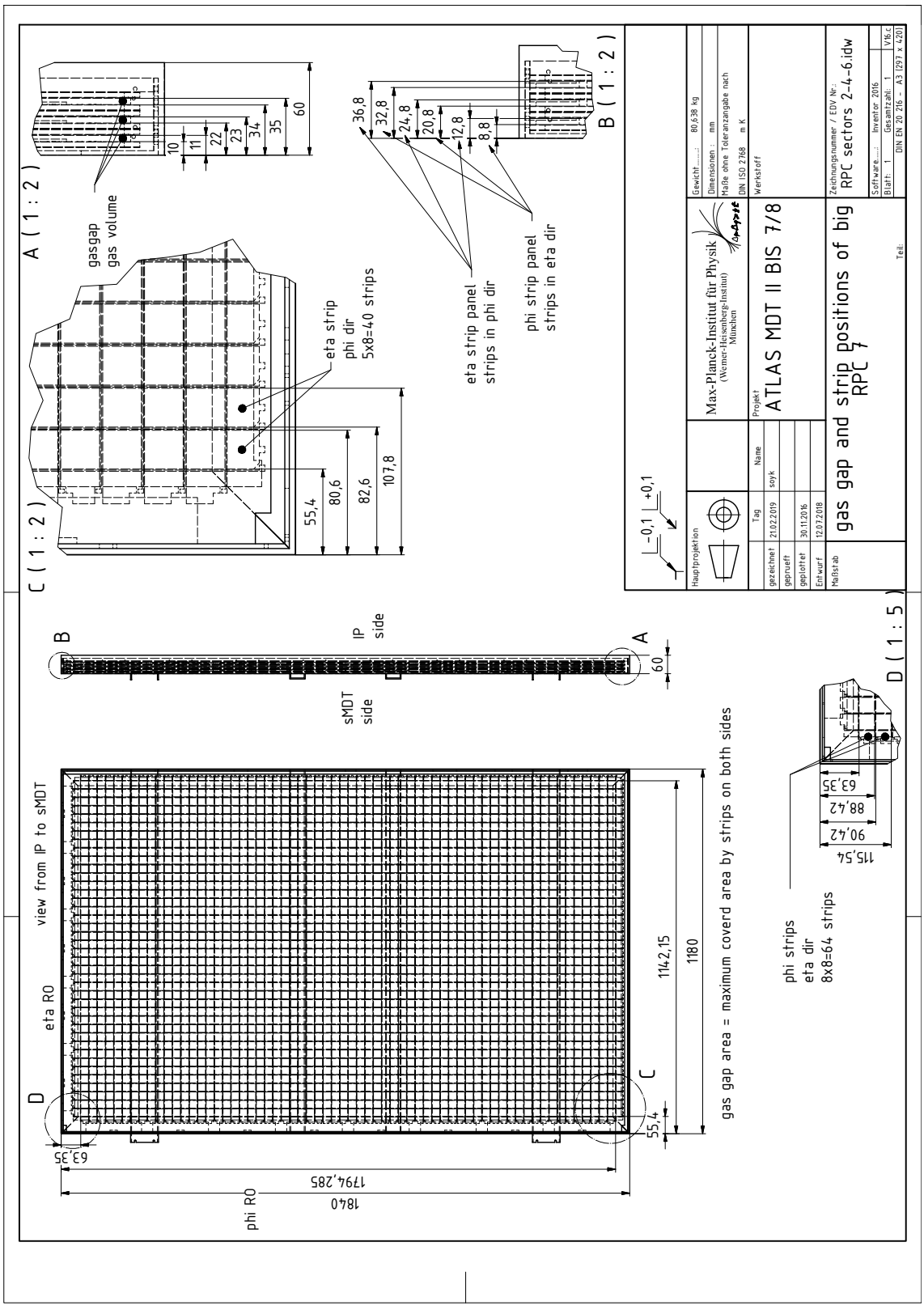

Figure 7.25. Gas gaps and strip positions of big RPC7

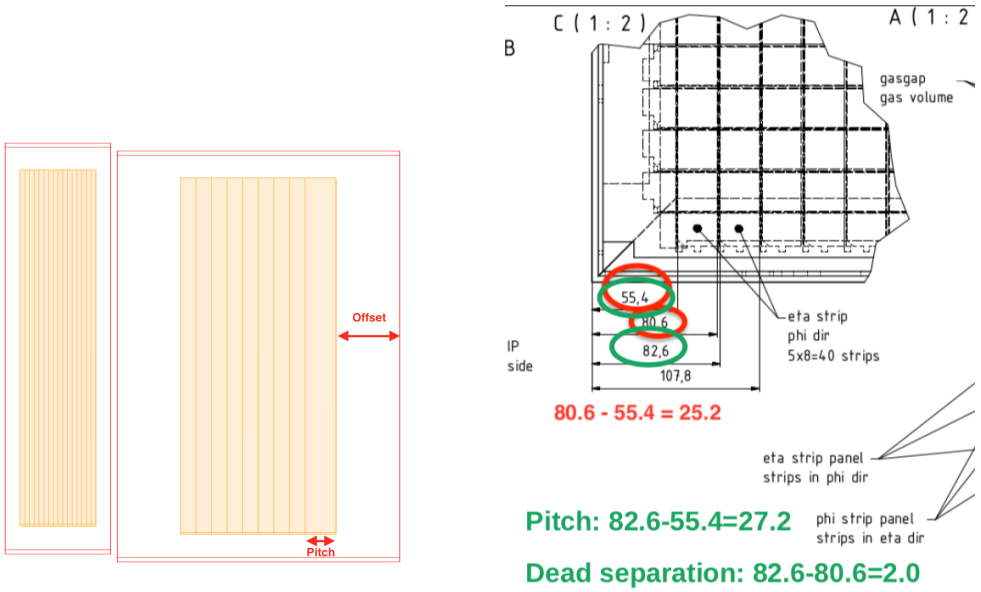

Figure 7.26. Illustration of pitch in Persint and pitch calculation in the drawing.

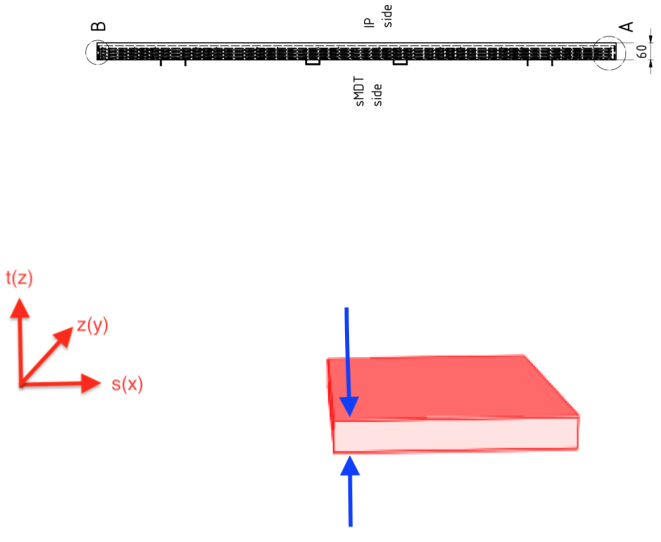

Figure 7.27. Illustration of total thickness parameter in drawings and Persint.

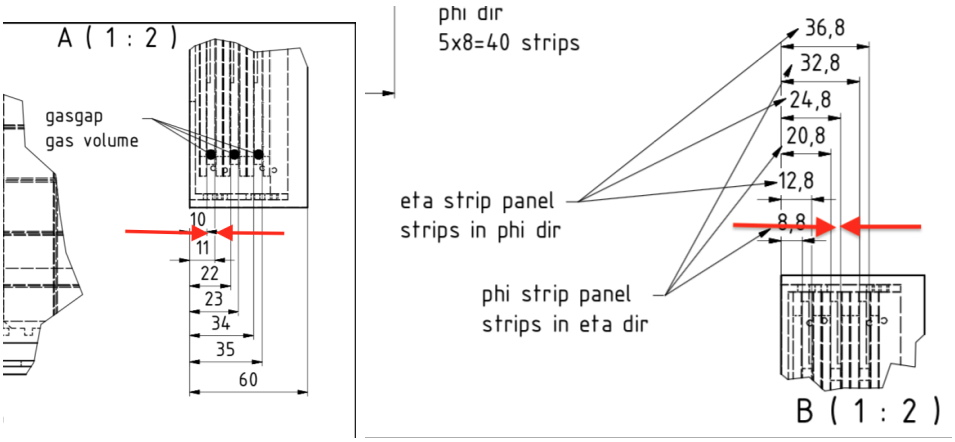

Figure 7.28. Gas volume and Strip panel parameter in the drawings.

7.10. Uploading to the Oracle Database

After implementing the new geometry in AMDB, this new file containing the information of the new geometry needs to be uploaded to the ATLAS Oracle Database to form a new layout for simulation. The new layout is formed in the name of *MuonSpectrometer-R.08.01-BIS78v3*. The initial checks are done in the database to see the correspondences between AMDB file and database.

7.11. How ATLAS Simulation Works

Simulation [8] is a very crucial part of ATLAS software project and it uses the Geant4 simulation toolkit. The simulation software developed in ATLAS has been used for large scale productions at the Computing Grid through production of approximately 10^9 full physics events. This process is mainly divided into three parts, though they may be combined into a single job: 1) event generation 2) physics and detector response 3) digitization of physics quantities with production of final output. The events are produced by many different generators interfaced to Athena and they have been checked in terms of physics performances. Events from these generators can either be written to a file for further processing, or passed directly into the further simulation stages. The particles in each event start from the vertex of (0,0,0). The layouts providing

the information of the geometry of the detectors for the simulation are available for running. After running a simulation of the particular events on a certain geometry, the interaction points of the particles on the active area are saved as coordinates of the simulation hits. Then, the ATLAS digitization software converts these hits to the detector response as digits.

7.12. Importance of Detector Simulation

Modern particle physics [9] is highly dependent on computer simulation in order to observe accurate physics. Simulation process begins with the particles produced by the so-called event generators at the collision point. As they traverse, their interaction such as decays or ionization through the detector is formed and is saved as hits. Then, these hits are transformed to the digits as the response of the detector by the digitization. Since today's detectors are immensely complex, all these processes of the matter and detector interaction cannot be calculated analytically without the help of computer simulation. Hence, the computer simulations in particle physics is the only way to understand the response of the detectors to the physics processes. This is the reason why particle physics studies require the simulated collision events in order to estimate the uncertainities of the experimental setup. Figure 7.29 shows how the detector simulation leads to the discovery of Higgs Boson. In this plot, detector simulation shows the uncertainty of the predicted measurement outcome of the null hypothesis, where the Higgs boson would not exist. The significance of the null hypothesis is tested by comparing the predicted measurement outcome and its uncertainty with the data recorded by the detector. This directly leads to the discovery of the Higgs boson. On the other hand, simulations are needed in order to produce huge data simulation with high statistics required by physics analysis.

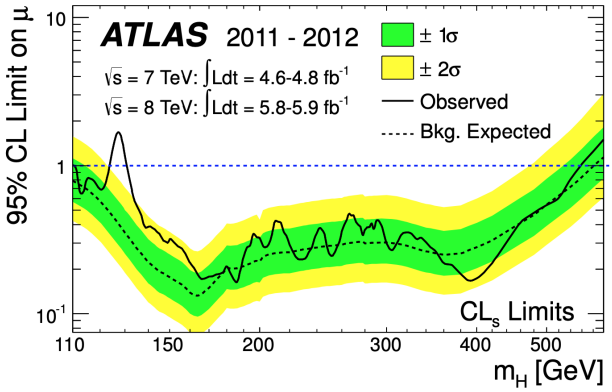

Figure 7.29. The exclusion plot on Higgs Boson [9].

7.13. Simulation for BIS78

The simulation is based on the new geometry of *MuonSpectrometer-R.08.01-BIS78v3* and consists of events of single particles with the range of transverse momentum 5 GeV and 7 GeV, fired on detector area of $1.0 < |\eta| < 1.3$, where the new stations are positioned. The story does not end when we describe new geometry in AMDB. For simulation, particular part of Athena forms those shapes in the simulation according to our definitions in AMDB as in Figure 7.30. In our case, the responsible parts are for forming the shapes for RPCs is *MuonGeoModel/RpcLayer.cxx* and for position of RPCs is *MuonGeoModel/Rpc.cxx*.

```
GeoVPhysVol*
RpcLayer::buildBIS(int cutoutson, std::vector<Cutout*> vcutdef)
{
    std::cout << std::setiosflags(std::ios::fixed);
    std::cout << std::setprecision(4);

    double eps = 0.000001;
    double tol = 1.e-6;

    MYSQL* mysql = MYSQL::GetPointer();
    RPC* r = (RPC*)mysql->GetTechnology(name);

    double thickness = 11.8 - tol; //fix r->rpcLayerThickness - tol;
    double length = m->length;
    double width  = m->width;
```

Figure 7.30. Example of retrieving information of AMDB in Athena framework.

7.14. Observation in Simulation

Active area is the part where the particles interact with detector material and the signal of response is sent through. Therefore, the volume of active area and its position in the envelope and match between hits and digits (detector response) are crucial in performance studies of the detector, therefore affect the quality of physics analysis. Hence, we need to be make sure of those properties in simulation are compatible with our implementation by the drawings. In order to do that, the first and last entries of simulation hits will be extracted and compared with the size of the active area defined in AMDB by the quantities in the drawings. The example of comparing the active areas of RPC7 in Z direction for all sectors can be seen in Table 7.1. In Table 7.1, it can be seen that active area in simulation is approximately 100 mm larger than our implementation for sec02,04,06 for Z direction. For sec08,10,12,14,16, active area in simulation is approximately 80 mm larger than our implementation. This anomaly is present for phi direction as well. These differences are out of range of tolerance of 1. mm. Possible reason to the range difference between the drawings and the simulation active area is because in software part, *MuonGeoModel* is not compatible with new RPCs of BIS78, which should be fixed.

RPC7	Beginning Z coordinate of the active area in Simulation	Ending Z coordinate of the active area in Simulation	Beginning Z coordinate of the active area in Implementation
octant1	5713.3	6874.4	5754.1
octant2	5713.3	6873.6	5754.1
octant3	5713.3	6873.6	5754.1
octant4	5894.5	6875.8	5935.1
octant5	5894.5	6875.5	5935.2
octant6	5894.5	6874.3	5935.1
ocant7	5894.5	6875.5	5935.1
octant8	5894.5	6873.0	5935.1
RPC7	Ending Z coordinate of the active area in Implementation	Active Area Size in Simulation	Active Area Size in Implementation
octant1	6840.9	1061.1	1086.75
octant2	6840.9	1060.3	1086.75
octant3	6840.9	1060.3	1086.75
octant4	6832.0	981.3	896.9
octant5	6832.0	981.0	896.9
octant6	6832.0	979.8	896.9
octant7	6832.0	981.0	896.9
octant8	6832.0	978.5	896.9

Table 7.1. Simulation hits coordinates in Z direction for RPC7 all sectors.

7.15. Updates in Software

After forming the BIS78 in AMDB, those sectors including detailed the geometry of active areas are formed by Geant4 in simulation with the information provided by AMDB. However, *MuonSpectrometer* package does not foreseen the new properties of BIS78, therefore and it should be modified.

7.15.1. Updates in MuonGeoModel

The main modifications that will be applied to Athena to create BIS station and BIS RPCs can be seen below:

- Rpc class should build 3 gas gaps in case of BIS chambers.
  (i) Rpc creates one additional RpcLayer object.
- Rpc uses the RpcLayer class to build the internal structure.
  (i) RpcLayer::build() → for the usual RPCs.
  (ii) RpcLayer::buildBIS() → new method to be added for BIS RPCs which is satisfying the new properties.
- Introduce the third layer.
- Introduce the new RPC objects.
- Introduce the BIS station.

In *RpcLayer* class, new buildBIS() method is defined in order to form new RPCs in BIS78. Software Athena is renovated according to the new structure of BIS78 RPCs. In Athena, BIS station and new RPC objects are introduced.

7.15.2. Resolving Active Area Issue

We deduced that the active area size and position in simulation are not corresponding to our implementation in AMDB in any sector and any direction. In order to solve this discrepancy, the responsible part for building active area in RpcLayer.cxx

of MuonGeoModel package must be modified. The values building the active area of RPCs in the simulation will be determined according to our implementation. The fixation of the size of the active area is essential as much as the fact that the active area begins and ends in the correct position. In order to do that, we need to change the responsible part of the code that forms and positions the active area of RPCs, which is *MuonGeoModel/RpcLayer.cxx*. In order to be sure that which part of the code forming the active areas, the effect of these modifications in the certain parts of the code are demonstrated by using some exagrated numbers. The following work is for the examination of how *RpcLayer.cxx* forms the active areas for RPCs of BIS78.

Resizing active area: This piece of code in *RpcLayer.cxx* in Figure 7.31 is suspected to be the responsible for forming the active areas. The following assumptions are made: *ggLength* and *ggWidth* in Figure 7.31 correspond to the respectively envelope dimensions in Y and Z directions. *gasLength* and *gasWidth* in Figure 7.31 correspond to the respectively active area size in Z and Y directions. Therefore, in order to modify the active area size, appropriate values must be subtracted from the *ggLength* and *ggWidth* variables to get the correct *gasLength* and *gasWidth* as active area sizes determined in the drawings. The subtraction values are defined as *deadFrameSizeEta* and *deadFrameSizePhi* variables for two different directions of Z and Y respectively. According to our assumptions, the code is changed to the way in Figure 7.31. To see the effect of the these changes on the active area and whether if it contracts the active area, the histogram of the simulation hits are drawn. In the following plots, the histograms of two situations of where *deadframesizeEta/Phi=0 mm* and *deadframesizeEta/Phi=500 mm* are superimposed and they are colored respectively as blue and red. For this work, the simulation is run over 1000 events. From the plots in Figure 7.36 and Figure 7.34, we see that the red simulation hits area actually is contracted by our modifications in the piece of code in Figure 7.31 of *RpcLayer.cxx*. Hence, the plots verify our assumptions regarding the definition of active area in the simulation.

Shifting: GeoTransform objects *ty* and *tz* in Figure 7.32 make the shift of the active area respectively in Y and Z direction. In the following plots, blue simulation hits

are for the case of *ty/tz = 0. mm* and red simulation hits are for the case of *ty/tz = 450/300. mm*. It can be seen from the plots, the red simulation hits area is shifted.

```
// this brings to the center of the gas gap

    double ggLength    = length;
    double ggWidth     = width/r->NGasGaps_in_s-eps;
    double gasLength   = ggLength - 2.*r->bakeliteframesize;
    double gasWidth    = ggWidth - 2.*r->bakeliteframesize;;
```

```
    double ggLength    = length;
    double ggWidth     = width/r->NGasGaps_in_s-eps;

    double deadframesizeEta = 500.;
    double deadframesizePhi = 500.;

    double gasLength   = ggLength - deadframesizeEta;

    double gasWidth    = ggWidth - deadframesizePhi;
```

Figure 7.31. The first version of code defining active area in Y and Z directions and the modifications made for redefining the active area.

```
GeoTransform* ty = new GeoTransform(GeoTrf::TranslateY3D(300.));

GeoTransform* tz = new GeoTransform(GeoTrf::TranslateZ3D(450.));

prpcl->add(ty);

prpcl->add(tz);
```

Figure 7.32. the piece of code making shifts in Y and Z directions.

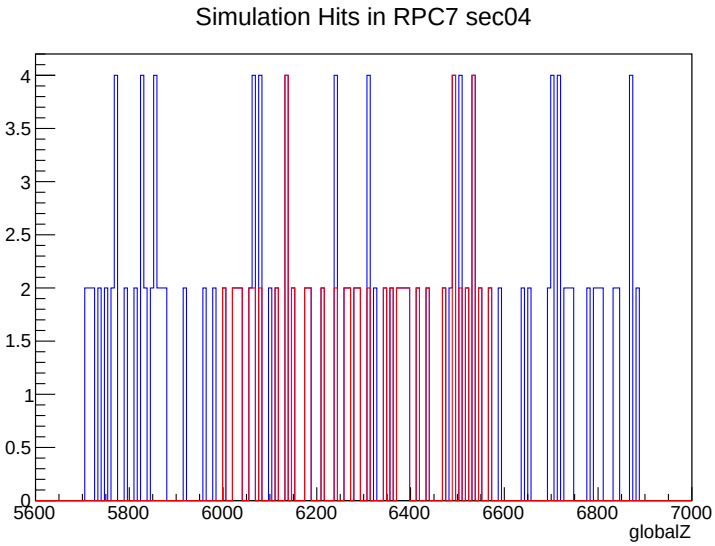

Figure 7.33. Simulation Hits for deadFrameSizeEta=0. and deadframesizeEta=500. in Z direction.

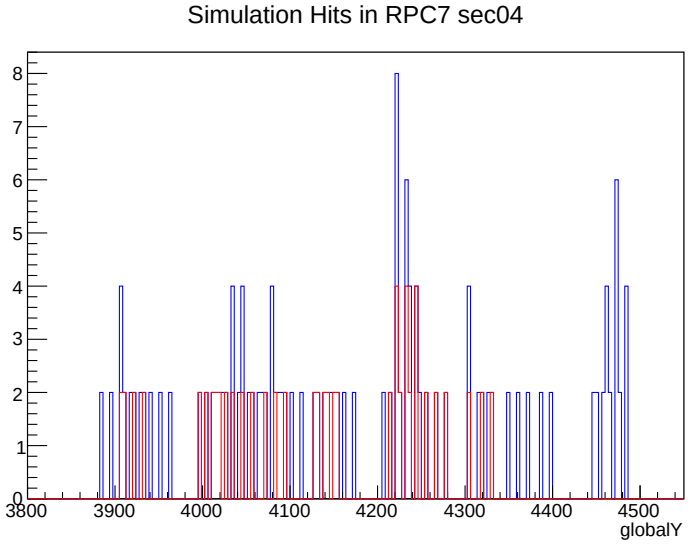

Figure 7.34. Simulation Hits for deadFrameSizePhi=0. and deadFrameSizePhi=500. in Y direction. Because of inclination in Y direction, the contraction amount will be different from the deadFrameSizePhi value.

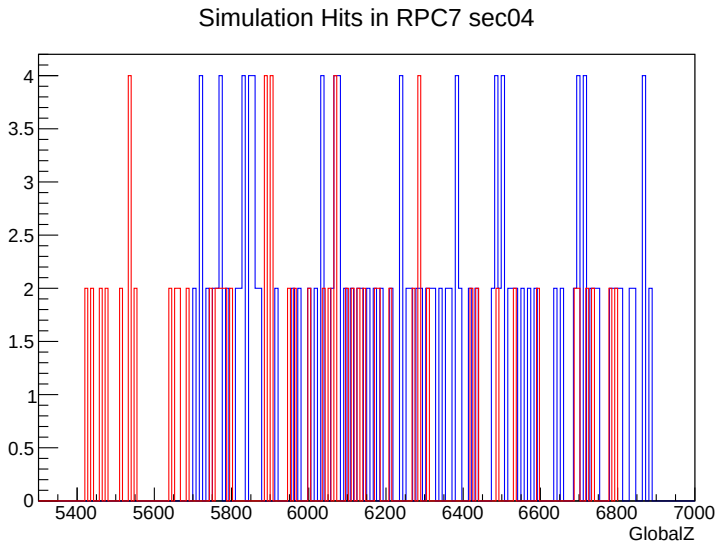

Figure 7.35. Simulation Hits for deadFrameSizeEta=0., tz = 450. in Z direction.

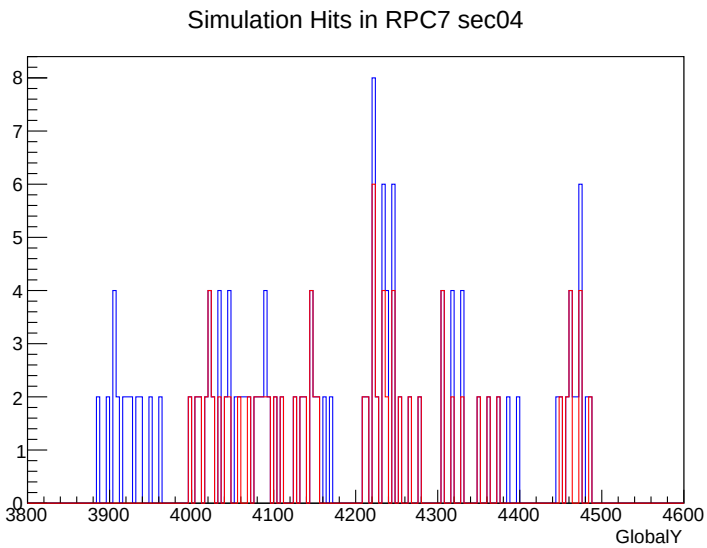

Figure 7.36. Simulation Hits for deadframesize=0., ty = 300. in Y direction.

7.16. Redefining the Active Area in Simulation

To determine the dead frame size values, the envelope dimension is subtracted from the active area size in the drawings. In simulation, the active area is positioned at the center of mass of the envelope by default, however, according to the drawings in Figure 7.37, the active area is positioned asymmetrically in the envelope. Hence, the certain amount of shifting must be applied. The offsets indicated in the drawing set the amount of shifting around center of mass in the active area. In order to determine the shifting values, we look at the difference between the default center of mass of the envelope and the center of mass of shifted version of the active area according to the drawing. Similarly, it can be done this way: To set the correct shifting values, first the shifting values are set to zero. From the global coordinate we get, the correct values are determined by subtracting the global coordinate *(tz=0)* from the beginning of active area in the global coordinate of the drawing. Since the active area sizes and their positions vary in the different types of RPCs, the following definitions are made in order to get the correct active area accordingly in Figure 7.38 and Figure 7.39. Different dead frame sizes and shifting variables are defined for each type of RPCs.

After making all of the corresponding changes according to the examination we did before, the position of simulation hits on BIS78 RPCs has been investigated. In practice, the construction and installation of RPCs has tolerance of 1 mm, so the difference between simulation and implementation side can be less than or equal 1 mm. The data in the Table 7.2 and Table 7.3 shows that the difference of simulation hits between implementation side and simulation side in η is in the 1 mm tolerance range. Hence, our geometry implementation and modified code are compatible with the data of the simulation. However, as it can be seen from the Table 7.6, the difference between observed simulation hits coordinates and the correct values of implementation in ϕ is not in the range of tolerance 1mm. So, the further investigations are needed. The simulation hits coordinates in Y will be searched for each gas gap layer (see Table 7.9). Yet, a pattern to the regarding issue is not found. This maybe resulted from the fact that RPC Digitization strategy where in X and Y direction, simulation hits cannot be

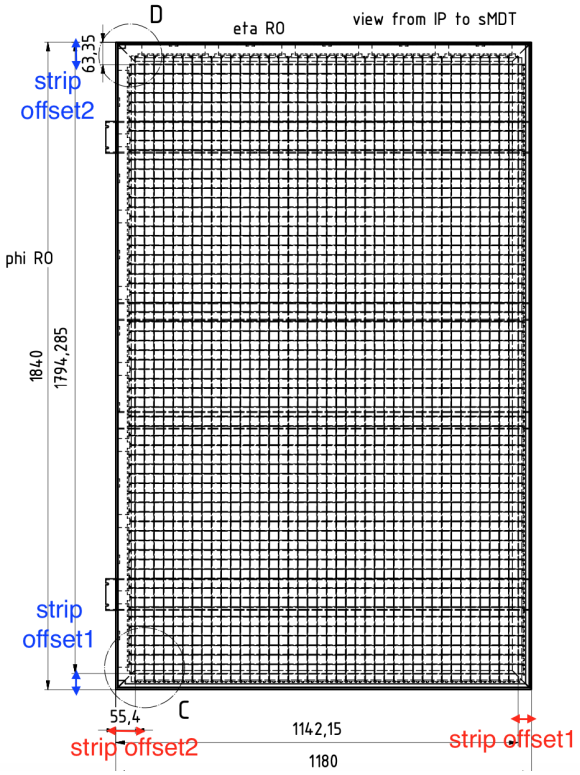

Figure 7.37. Strip volume position in the drawings.

```
  double ggLength    = length;
  double ggWidth     = width/r->NGasGaps_in_s-eps;


  double gasLength;
  double gasWidth;

  double deadframesizeEta;
  double deadframesizePhi;

  double y_translation;
  double z_translation;


if(name == "RPC26" ){//big RPC7

   deadframesizeEta = 93.25;
   deadframesizePhi = 109.52;


   gasLength    = ggLength - deadframesizeEta;
   gasWidth     = ggWidth - deadframesizePhi;

   y_translation = - 9.1;
   z_translation = 3.22;
}
```

```
if(name == "RPC27" ){//small RPC7

   deadframesizeEta = 93.12;
   deadframesizePhi = 109.52;

   gasLength    = ggLength - deadframesizeEta;
   gasWidth     = ggWidth - deadframesizePhi;

   y_translation = - 9.1;
   z_translation = 3.06;

}
```

Figure 7.38. Redefining active areas of RPC26 and RPC27.

```
if(name == "RPC28"){//big RPC8

   deadframesizeEta = 93.04;
   deadframesizePhi = 109.52;


   gasLength    = ggLength - deadframesizeEta;
   gasWidth     = ggWidth - deadframesizePhi;


   y_translation = - 27.7;
   z_translation = 3.11;

}
```

```
if(name == "RPC29"){//small RPC8

   deadframesizeEta = 93.04;
   deadframesizePhi = 109.2;


   gasLength    = ggLength - deadframesizeEta;
   gasWidth     = ggWidth - deadframesizePhi;

   y_translation = - 8.8;
   z_translation = 3.11;

}
```

Figure 7.39. Redefining active areas of RPC28 and RPC29.

```
GeoTransform* ty = new GeoTransform(HepGeom::TranslateY3D(y_translation));
GeoTransform* tz = new GeoTransform(HepGeom::TranslateZ3D(z_translation));

prpcl->add(tx);
prpcl->add(ty);
prpcl->add(tz);
```

Figure 7.40. Translation objects in the code.

corresponding to the picture of the new geometry. This will be updated as well for further steps but this is well enough for our foresight. Another reason that is the fact that the fixation of layer positions is still under investigation; therefore, it could affect the position of simulation hits in Y direction. The active area in ϕ direction still is in the perfect shape for further studies at this point.

7.16.1. Fixing Digits

Now, we are sure of the fact that the active areas in the stations are implemented correctly and simulation hits are in the correct positions, we can move onto the examination of digits. In order to be sure that strips are in the correct position, we need to check the number of strips and and pitch values and see whether they are in the way that are implemented in AMDB. As it can be seen from the Table 7.14, the number of η strips is 40/32 and the pitch value is are compatiple with 27.2/28.09/21.81 mm ; for ϕ strips, the number of strips is 64 and the pitch values are compatible with 27.07/25.2

which are the exact values that are implemented in AMDB. All sectors are checked in terms of the correspondance between digits and simulation hits and they are in agreement as well. As it can be seen from the Figure 7.41 and Figure 7.42 matches between digits and simulation hits are in good agreement.

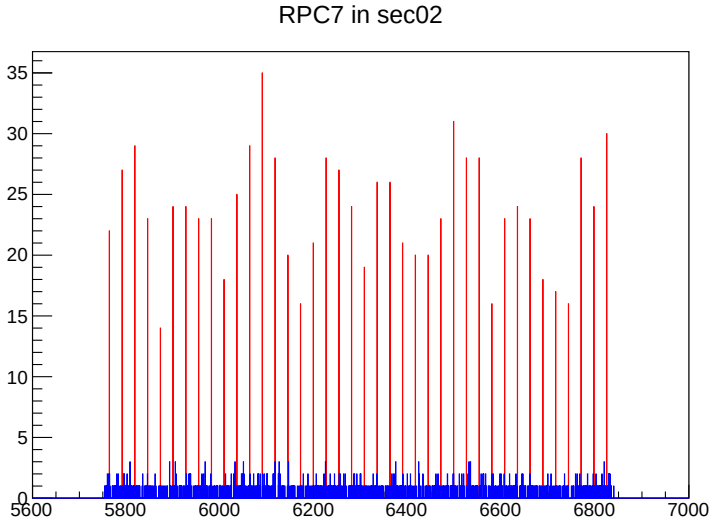

Figure 7.41. Simulation hits in Z direction and η strips digits correspondance. Blue color is for the simulation hits and red color is for the digits. This is the first octant of RPC7.

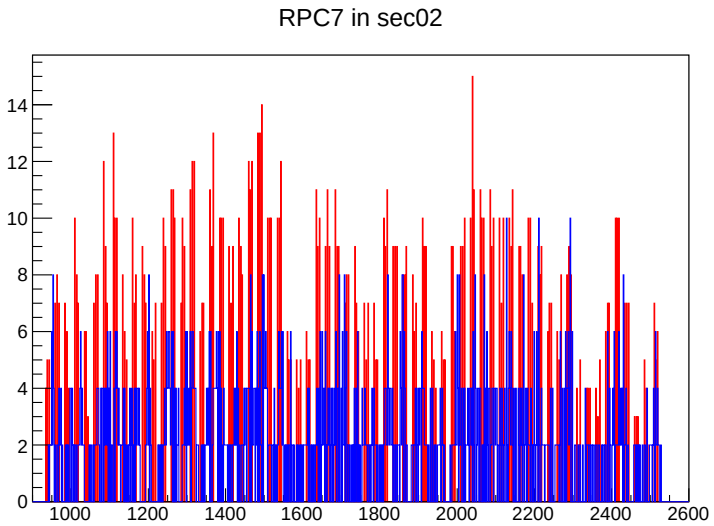

Figure 7.42. Simulation hits in Y direction and ϕ strips digits correspondance. Blue color is for the simulation hits and red color is for the digits. This is the first octant of RPC7.

RPC7	Beginning Z coordinate of the active area in Simulation	Ending Z coordinate of the active area in Simulation	Beginning Z coordinate of the active area in Implementation
octant 1	5754.2	6840.0	5754.1
octant 2	5755.4	6840.8	5754.1
octant 3	5755.6	6840.8	5754.1
octant 4	5936.8	6832.0	5935.1
octant 5	5935.1	6831.8	5935.1
octant 6	5936.7	6832.5	5935.1
octant 7	5935.8	6832.0	5935.1
octant 8	5935.1	6832.0	5935.1
RPC7	Ending Z coordinate of the active area in Implementation	Active Area Size in Simulation	Active Area Size in Implementation
octant 1	6840.9	1085.8	1086.7
octant 2	6840.9	1085.4	1086.7
octant 3	6840.9	1085.2	1086.7
octant 4	6832.0	895.2	896.9
octant 5	6832.0	896.7	896.9
octant 6	6832.0	895.9	896.9
octant 7	6832.0	896.2	896.9
octant 8	6832.0	896.9	896.9

Table 7.2. Simulation hits coordinates in Z direction for RPC7 in all sectors.

RPC8	Beginning Z coordinate of the active area in Simulation	Ending Z coordinate of the active area in Simulation	Beginning Z coordinate of the active area in Implementation
octant 1	6962.1	7308.0	6962.0
octant 2	6961.9	7308.9	6962.0
octant 3	6962.7	7308.9	6962.0
octant 4	6961.9	7308.9	6962.0
octant 5	6961.9	7308.9	6962.0
octant 6	6961.9	7308.8	6962.0
octant 7	6961.9	7308.9	6962.0
octant 8	6962.4	7308.7	6962.0
RPC8	Ending Z coordinate of the active area in Implementation	Active Area Size in Simulation	Active Area Size in Implementation
octant 1	7308.6	346.0	347.0
octant 2	7308.9	347.0	347.0
octant 3	7308.9	346.2	347.0
octant 4	7308.9	347.0	347.0
octant 5	7308.9	346.9	347.0
octant 6	7308.9	346.9	347.0
octant 7	7308.9	346.9	347.0
octant 8	7308.9	346.3	347.0

Table 7.3. Simulation hits coordinates in Z direction for RPC8 in all sectors.

RPC7	Beginning Y coordinate of the active area in Simulation	Ending Y coordinate of the active area in Simulation	Beginning Y coordinate of the active area in Implementation
octant 1	930.3	2529.3	917.6
octant 2	3817.5	4505.5	3825.9
octant 3	3834.3	4515.0	3825.9
octant 4	933.0	2548.0	917.6
octant 5	-913.0	-2528.0	-917.6
octant 6	-3845.3	-4525.3	-3811.0
octant 7	-3836.0	-4524.0	-3825.9
octant 8	-950.5	-2551.5	-920.1
RPC7	Ending Y coordinate of the active area in Implementation	Active Area Size in Simulation	Active Area Size in Implementation
octant 1	2516.4	1599.0	1598.8
octant 2	4488.1	688.0	662.2
octant 3	4488.1	680.7	662.2
octant 4	2516.4	1615.0	1598.8
octant 5	-2516.4	1615.0	1598.8
octant 6	-4473.2	680.0	662.2
octant 7	-4488.1	688.0	662.2
octant 8	-2518.9	1601.0	1598.8

Table 7.4. Simulation hits coordinates in Y direction for RPC7 in all sectors.

RPC8	Beginning Y coordinate of the active area in Simulation	Ending Y coordinate of the active area in Simulation	Beginning Y coordinate of the active area in Implementation
octant 1	1062.0	2557.0	1061.1
octant 2	3894.0	4566.0	3879.5
octant 3	3916.0	4596.0	3879.5
octant 4	990.5	2569.5	1048.7
octant 5	-934.5	-2546.5	-1052.1
octant 6	-3949.5	-4560.3	-3871.2
octant 7	-3960.0	-4597.0	-3895.0
octant 8	-1094.5	-2523.5	-1069.6
RPC8	Ending Y coordinate of the active area in Implementation	Active Area Size in Simulation	Active Area Size in Implementation
octant 1	2549.3	1495.0	1488.2
octant 2	4541.7	672.0	662.2
octant 3	4541.7	680.0	662.2
octant 4	2647.4	1579.0	1598.8
octant 5	-2651.0	1612.0	1598.8
octant 6	-4487.7	610.8	616.4
octant 7	4511.5	637.0	616.4
octant 8	2557.8	1429.0	1488.2

Table 7.5. Simulation hits coordinates in Y direction for RPC8 in all sectors.

RPC7	Beginning Y coordinate of the active area in Simulation	Ending Y coordinate of the active area in Simulation	Beginning Y coordinate of the active area in Implementation
1. octant			
1. gas gap	930.0	2511.0	917.6
2. gas gap	930.0	2530.0	928.5
3. gas gap	930.0	2530.0	939.4
2. octant			
1. gas gap	3815.5	4486.9	3825.9
2. gas gap	3832.3	4495.3	3830.4
3. gas gap	3843.0	4506.9	3834.9
3. octant			
1. gas gap	3832.3	4495.3	3825.9
2. gas gap	3844.0	4506.0	3830.4
3. gas gap	3853.2	4516.9	3834.9
4. octant			
1. gas gap	931.5	2529.9	917.6
2. gas gap	931.5	2548.5	928.5
3. gas gap	933.0	2548.0	939.4

Table 7.6. Simulation hits coordinates in Y direction for RPC7 for each gas gap in all sectors.

RPC7	Beginning Y coordinate of the active area in Simulation	Ending Y coordinate of the active area in Simulation	Beginning Y coordinate of the active area in Implementation
5. octant			
1. gas gap	-911.5	-2528.5	-917.6
2. gas gap	-913.0	-2528.0	-928.5
3. gas gap	-913.0	-2528.0	-939.4
6. octant			
1. gas gap	-3843.0	-4497.0	-3811.0
2. gas gap	-3854.0	-4508.9	-3815.5
3. gas gap	-3864.0	-4526.0	-3820.0
7. octant			
1. gas gap	-3841.9	-4496.0	-3825.9
2. gas gap	-3852.9	-4507.9	-3830.4
3. gas gap	-3862.9	-4525.9	-3834.9
8. octant			
1. gas gap	-950.0	-2548.5	-920.1
2. gas gap	-951.5	-2549.5	-931.0
3. gas gap	-950.0	-2548.5	-941.9

Table 7.7. Simulation hits coordinates in Y direction for RPC8 for each gas gap in all sectors.

RPC7	Ending Y coordinate of the active area in Implementation	Active Area Size in Simulation	Active Area Size in Implementation
1. octant			
1. gas gap	2516.4	1581.0	1598.8
2. gas gap	2527.3	1600.0	1598.8
3. gas gap	2538.2	1600.0	1598.8
2. octant			
1. gas gap	4488.1	671.4	662.2
2. gas gap	4492.6	663.0	662.2
3. gas gap	4497.1	663.9	662.2
3. octant			
1. gas gap	4488.1	663.0	662.2
2. gas gap	4492.6	662.0	662.2
3. gas gap	4497.1	663.7	662.2
4. octant			
1. gas gap	2516.4	1598.4	1598.8
2. gas gap	2527.3	1617.0	1598.8
3. gas gap	2538.2	1618.0	1598.8

Table 7.8. Simulation hits coordinates in Y direction for RPC7 in all sectors for each gas gap.

RPC7	Ending Y coordinate of the active area in Implementation	Active Area Size in Simulation	Active Area Size in Implementation
5. octant			
1. gas gap	-2516.4	1617.0	1598.8
2. gas gap	-2527.3	1615.0	1598.8
3. gas gap	-2538.2	1615.0	1598.8
6. octant			
1. gas gap	-4473.2	654.0	662.2
2. gas gap	-4477.7	654.9	662.2
3. gas gap	-4482.2	662.0	662.2
7. octant			
1. gas gap	-4488.1	654.1	662.2
2. gas gap	-4492.6	655.0	662.2
3. gas gap	-4497.1	663.0	662.2
8. octant			
1. gas gap	-2518.9	1598.5	1598.8
2. gas gap	-2529.8	1598.0	1598.8
3. gas gap	-2540.7	1598.5	1598.8

Table 7.9. Simulation hits coordinates in Y direction for RPC7 in all sectors for each gas gap.

RPC8	Beginning Y coordinate of the active area in Simulation	Ending Y coordinate of the active area in Simulation	Beginning Y coordinate of the active area in Implementation
1. octant			
1. gas gap	1061.9	2558.0	1061.1
2. gas gap	1062.0	2558.0	1072.0
3. gas gap	1062.0	2558.0	1082.9
2. octant			
1. gas gap	3893.0	4547.0	3879.5
2. gas gap	3911.0	4557.0	3884.0
3. gas gap	3913.0	4567.0	3888.5
3. octant			
1. gas gap	3914.0	4576.0	3879.5
2. gas gap	3931.5	4586.0	3884.0
3. gas gap	3934.5	4590.0	3888.5
4. octant			
1. gas gap	989.0	2570.0	1048.7
2. gas gap	989.0	2570.0	1059.6
3. gas gap	989.5	2569.5	1070.5

Table 7.10. Simulation hits coordinates in Y direction for RPC8 for each gas gap in all sectors.

RPC8	Beginning Y coordinate of the active area in Simulation	Ending Y coordinate of the active area in Simulation	Beginning Y coordinate of the active area in Implementation
5. octant			
1. gas gap	-932.0	-2547.0	-1052.1
2. gas gap	-931.5	-2548.5	-1063.0
3. gas gap	-933.0	-2548.0	-1073.9
6. octant			
1. gas gap	-3956.0	-4544.0	-3871.2
2. gas gap	-3966.0	-4561.0	-3875.7
3. gas gap	-3975.5	-4534.5	-3880.2
7. octant			
1. gas gap	-3960.0	-4571.5	-3895.0
2. gas gap	-3970.0	-4580.0	-3899.5
3. gas gap	-3980.5	-4592.5	-3904.0
8. octant			
1. gas gap	-1094.5	-2505.5	-1069.6
2. gas gap	-1096.0	-2524.5	-1080.5
3. gas gap	-1096.0	-2524.0	-1091.4

Table 7.11. Simulation hits coordinates in Y direction for RPC8 in all sectors for each gas gap.

RPC8	Ending Y coordinate of the active area in Implementation	Active Area Size in Simulation	Active Area Size in Implementation
1. octant			
1. gas gap	2549.3	1496.1	1488.2
2. gas gap	2560.2	1496.0	1488.2
3. gas gap	2571.1	1496.0	1488.2
2. octant			
1. gas gap	4541.7	654.0	662.2
2. gas gap	4546.2	646.0	662.2
3. gas gap	4550.7	654.0	662.2
3. octant			
1. gas gap	4541.7	662.0	662.2
2. gas gap	654.5	662.2	662.2
3. gas gap	4550.7	655.5	662.2
4. octant			
1. gas gap	2647.4	1581.0	1598.8
2. gas gap	2658.4	1581.0	1598.8
3. gas gap	2669.3	1580.0	1598.8

Table 7.12. Simulation hits coordinates in Y direction for RPC8 for each gas gap in all sectors.

RPC8	Ending Y coordinate of the active area in Implementation	Active Area Size in Simulation	Active Area Size in Implementation
5. octant			
1. gas gap	-2651.0	1615.0	1598.8
2. gas gap	-2661.8	1617.0	1598.8
3. gas gap	-2672.7	1615.0	1598.8
6. octant			
1. gas gap	-4487.7	588.0	616.4
2. gas gap	-4492.1	595.0	616.4
3. gas gap	-4496.6	559.0	616.4
7. octant			
1. gas gap	-4511.5	611.5	616.4
2. gas gap	-4515.9	610.0	616.4
3. gas gap	-4520.0	612.0	616.4
8. octant			
1. gas gap	-2557.8	1411.0	1488.2
2. gas gap	-2568.7	1429.5	1488.2
3. gas gap	-2579.6	1428.0	1488.2

Table 7.13. Simulation hits coordinates in Y direction for RPC8 in all sectors for each gas gap.

RPC7	number of η strips	number of ϕ strips	pitch of η (mm)	pitch of ϕ(mm)
1. octant	40	64	27.2	27.0
2. octant	40	64	27.2	27.0
3. octant	40	64	27.2	27.0
4. octant	32	64	28.0	27.0
5. octant	32	64	28.0	27.0
6. octant	32	64	28.0	27.0
7. octant	32	64	28.0	27.0
8. octant	32	64	28.0	27.0
RPC8				
1. octant	16	64	21.8	25.0
2. octant	16	64	21.8	27.0
3. octant	16	64	21.8	27.0
4. octant	16	64	21.8	27.0
5. octant	16	64	21.8	27.0
6. octant	16	64	21.8	25.0
7. octant	16	64	21.8	25.0
8. octant	16	64	21.8	25.0

Table 7.14. Pitch Values and Number of Srips for RPC7 and RPC8 in all sectors.

8. CONCLUSION

In this study, the new geometry for additional RPC chamber that will be placed in ATLAS detector barrel inner region for the necessity brought by HL-LHC is implemented for the full simulation. The new sector, BIS78, is described in the AMDB according to the new detector designs. In order to include the new enviroment for the full ATLAS simulation, it is implemented in the AMDB and uploaded into the ATLAS Oracle Database and Athena *MuonSpectrometer/MuonGeoModel* package is modified in the way that it will be compatible with the properties of the new geometry. The new RPC classes are added to *MuonSpectrometer/MuonGeoModel* and the definitions for forming the active areas in the detectors are redefined for BIS78 case. The simulation of the new geometry successfully run and the results have been investigated in terms of physics studies. The most prior part of the investigation is how the active areas of the new geometry act and whether if it satisfies the expected performance in the simulation. It is seen that the new geometry in simulation works in the way that it is expected and it satisfies the expectation of the new design and physics performance. The active areas in η and ϕ directions are in the expected positions comparing to our implementation. The strip positions and pitches in simulation are compatible with our implementation. The matching between digits and simulation hits are in good agreement. This will facilitate the further studies for physics performance of new geometry BIS78 in the simulation. Hence, the main priority for full ATLAS simulation has been completed.

REFERENCES

1. Geant4 Collaboration, *Introduction to Geant4*, Tech. rep., CERN, CERN,Switzerland, 2019.

2. Geant4 Collaboration, *Book For Application Developers*, Tech. rep., CERN, CERN,Switzerland, 2019.

3. Kretz, Moritz, Manner, Reinhard, Kugel, Andreas, *Studies Concerning the ATLAS IBL Calibration Architecture*, Ph.D. Thesis, CERN, CERN, 2020.

4. ATLAS Collaboration, *Technical Design Report for the Phase-II Upgrade of the ATLAS Muon Spectrometer*, Tech. rep., CERN, CERN,Switzerland, 2017.

5. ATLAS Collaboration, *Technical Design Report*, Tech. rep., CERN, CERN,Switzerland, 1997.

6. ATLAS Collaboration, *Persint Event Displayer of ATLAS*, Tech. rep., CERN, CERN,Switzerland, 2017.

7. ATLAS Collaboration, *The AMDB Manual*, Tech. rep., CERN, CERN,Switzerland, 2017.

8. A. Rimoldi and the ATLAS Collaboration, *Simulation strategies for the ATLAS Experiment at LHC, 2011 J. Phys.: Conf. Ser. 331 032026*, 2011.

9. Elmar Ritsch, *ATLAS Detector Simulation in the Integrated Simulation Framework applied to the W Boson Mass Measurement*, Ph.D. Thesis, CERN, CERN,Switzerland, 2017.

10. William R. Leo, *Techniques for Nuclear and Particle Physics Experiments*, Springer-Verlag Berlin Heidelberg, Route de St. Maurice 34. CH-1814 La Tour

de Peilz Switzerland, 1987.

11. Peter Sigmund, *Particle Penetration and Radiation Effects*, Springer-VerlagBerlin Heidelberg 2006, University of Southern Denmark Department of Physics Campusvej 555230 Odense Denmark E-mail: psi@dou.dk, 2006.

12. Giordano Cattani and the RPC group, *The Resistive Plate Chambers of the ATLAS experiment: performance studies*, *2011 J. Phys.: Conf. Ser. 280 012001*, 2011.

13. ATLAS Collaboration, *ATLAS Letter of Intent Phase-II Upgrade*, Tech. rep., CERN, CERN,Switzerland, 2012.

APPENDIX A: PERMISSION FOR USING FIGURES

The written permission from ATLAS Secretariat about using Figures/Pictures/Visuals/Information from ATLAS/CERN sources is in Figure A.1.

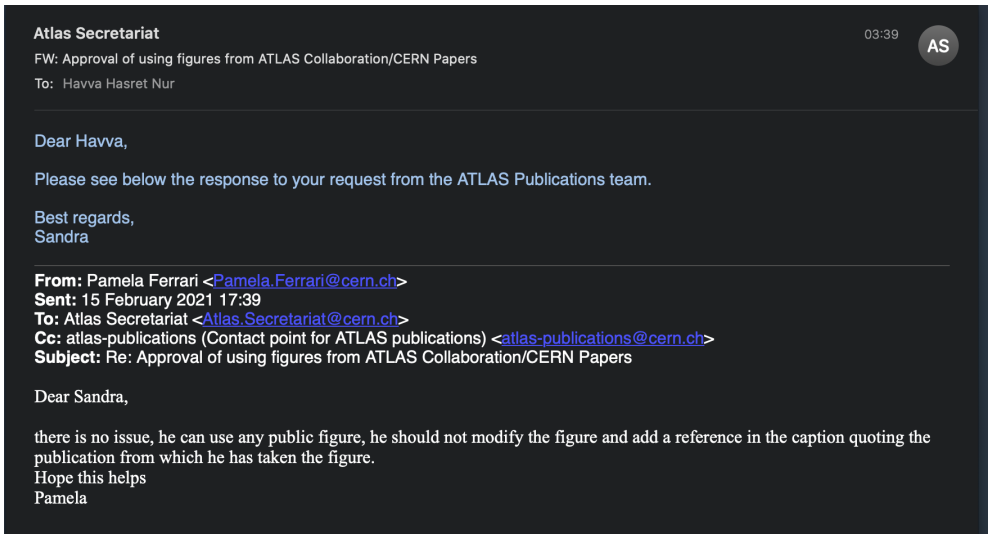

Atlas Secretariat 03:39 AS

FW: Approval of using figures from ATLAS Collaboration/CERN Papers

To: Havva Hasret Nur

Dear Havva,

Please see below the response to your request from the ATLAS Publications team.

Best regards,
Sandra

From: Pamela Ferrari <Pamela.Ferrari@cern.ch>
Sent: 15 February 2021 17:39
To: Atlas Secretariat <Atlas.Secretariat@cern.ch>
Cc: atlas-publications (Contact point for ATLAS publications) <atlas-publications@cern.ch>
Subject: Re: Approval of using figures from ATLAS Collaboration/CERN Papers

Dear Sandra,

there is no issue, he can use any public figure, he should not modify the figure and add a reference in the caption quoting the publication from which he has taken the figure.
Hope this helps
Pamela

Figure A.1. The Permission from ATLAS Secretariat.

APPENDIX B: INNER STRUCTURE OF RPCS IN BIS78

The information of RPC inner structure in the BIS78 drawings can be found in this chapter. Quantities are in mm.

W	RPC	Type
pitch_phi	pitch_eta	dead_separation
number of phi strips	number of eta strips	
strip_offset_phi	strip_offset_eta	
number of strip readouts	number of gas gaps	

Table B.1. General Scheme of RPC Inner Structure.

W	RPC	26 (Big RPC7)
27.07 64 45.71 1	27.2 40 37.85 1	2.
W 27.07 64 45.715 1	RPC 28.09 32 37.63 1	27 (Small RPC7) 2.
W 27.07 64 26.996 1	RPC 21.81 16 37.64 1	28 (Big RPC8) 2.
W 25.2 64 45.8 1	RPC 21.81 16 37.64 1	29 (Small RPC8) 2.

Table B.2. RPC Inner Structure in the code.

APPENDIX C: DESIGN DRAWINGS OF BIS7/8

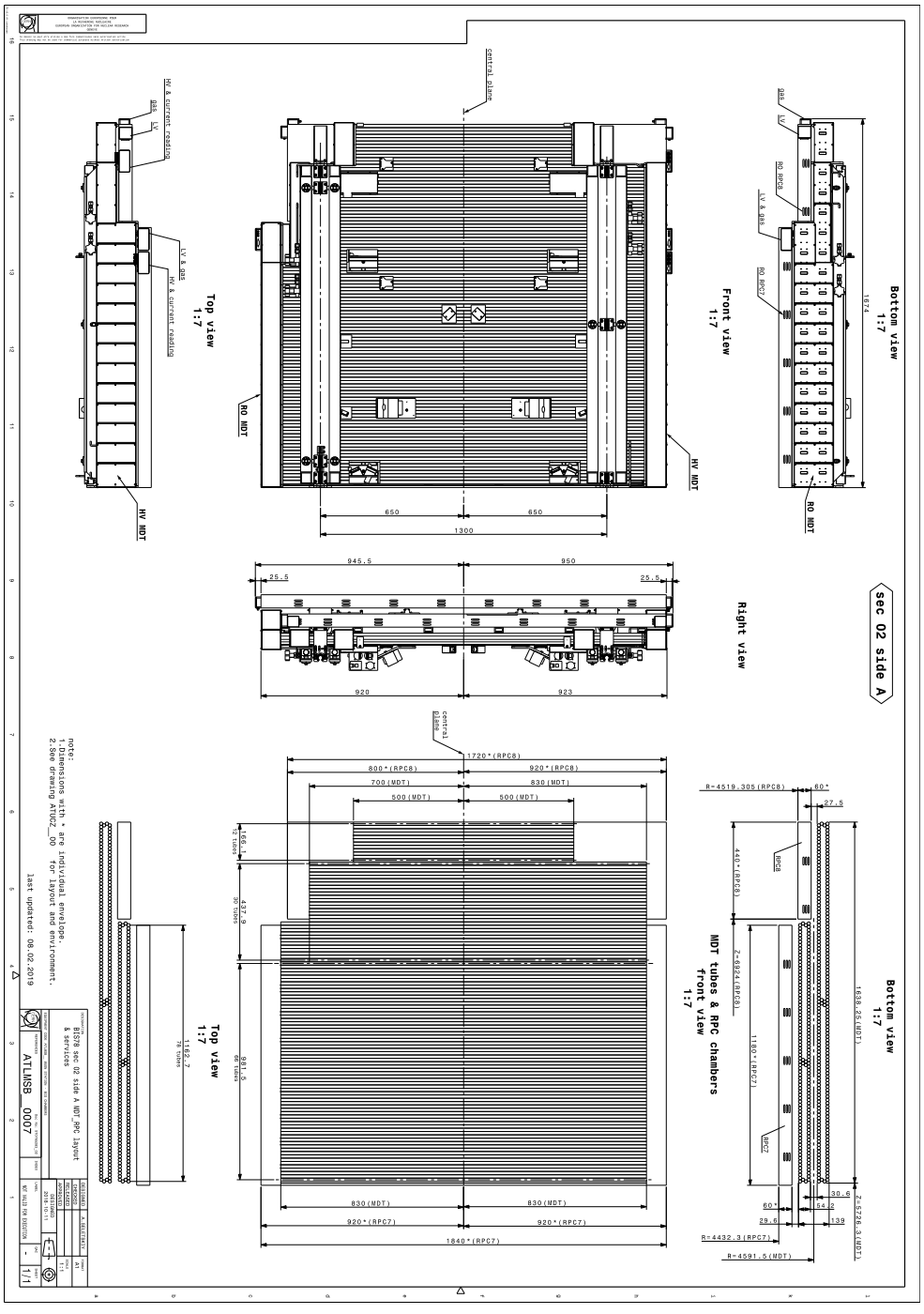

Figure C.1. RPC and sMDT design for octant 1 side A.

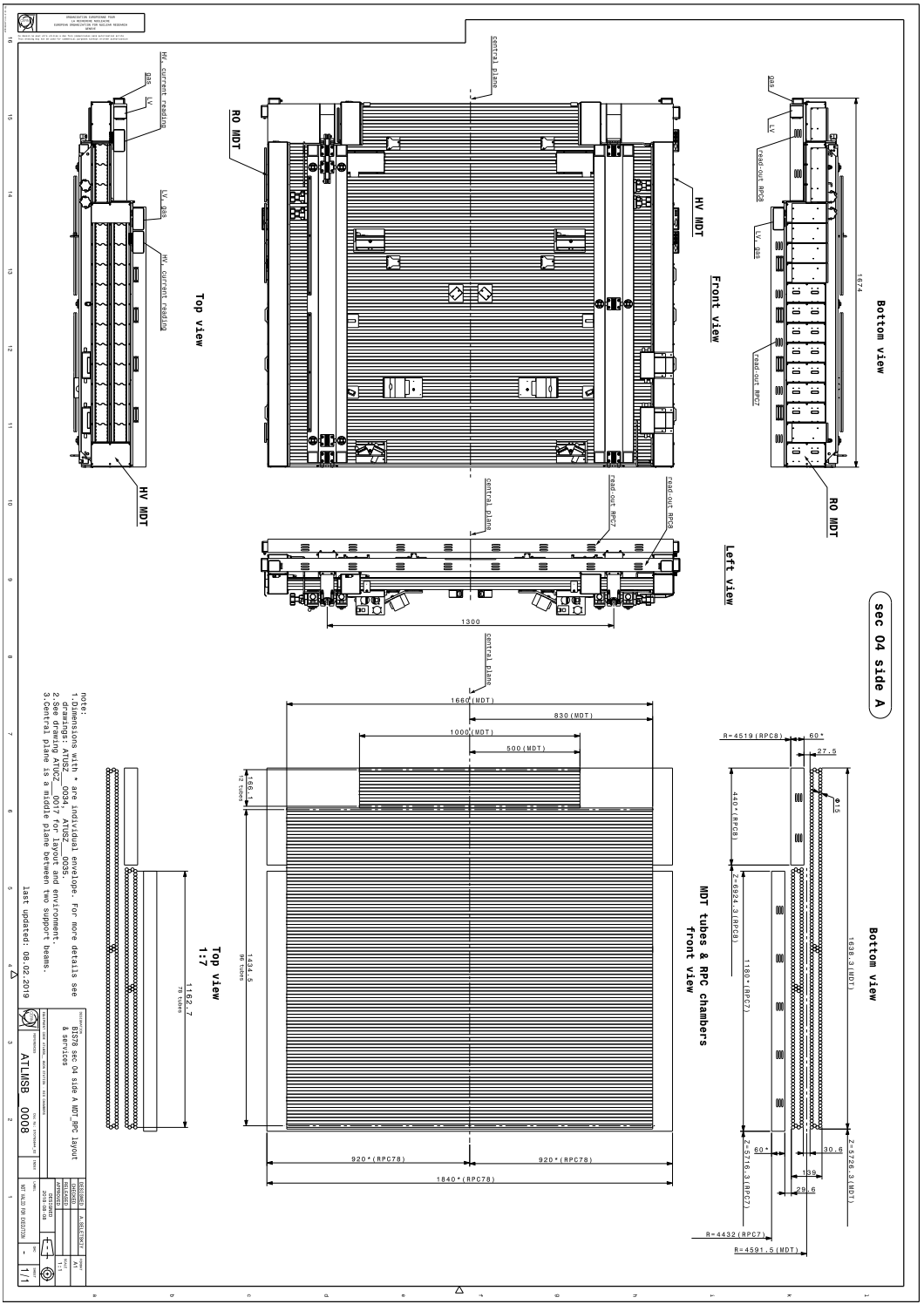

Figure C.2. RPC and sMDT design for octant 2 side A.

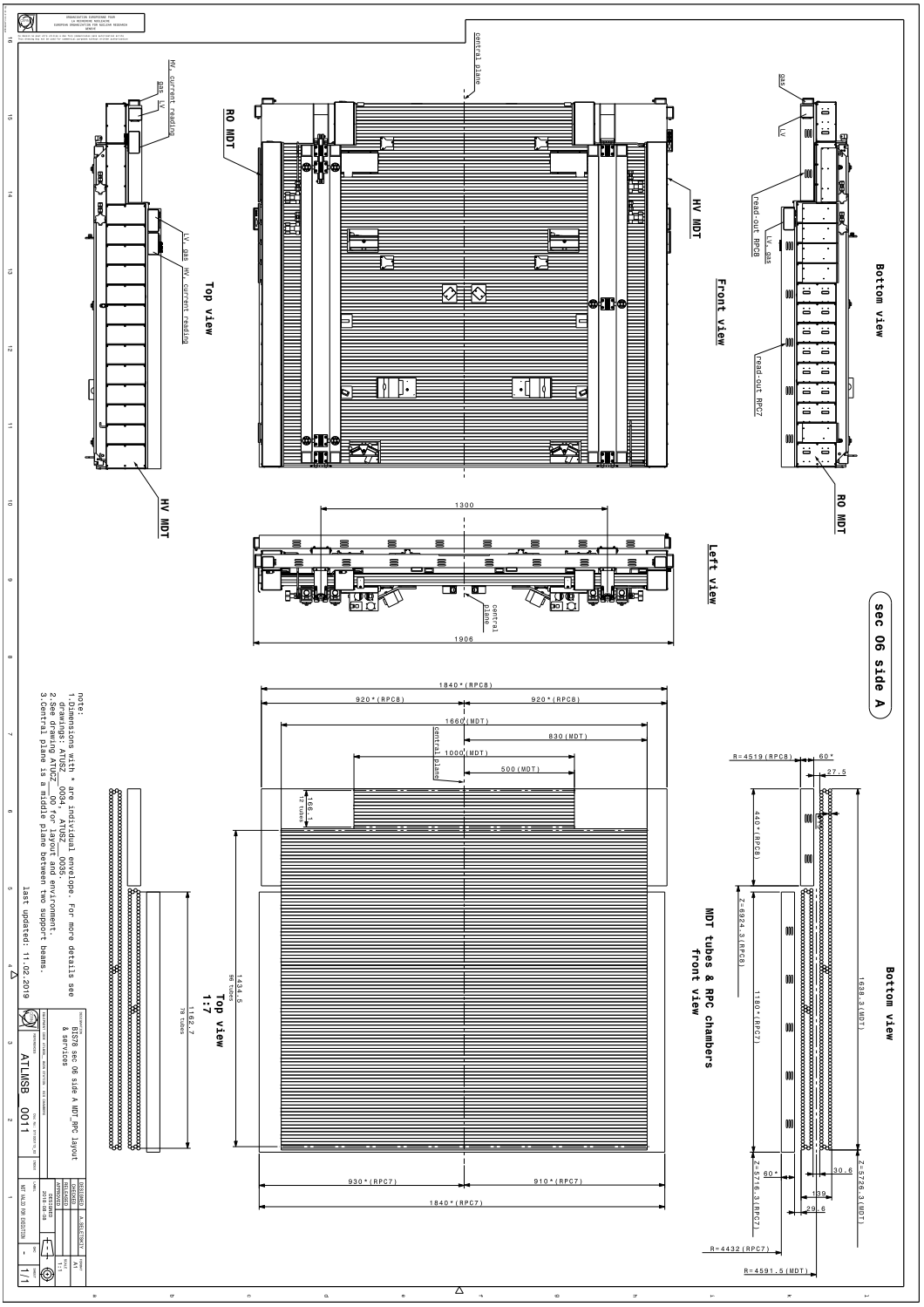

Figure C.3. RPC and sMDT design for octant 3 side A.

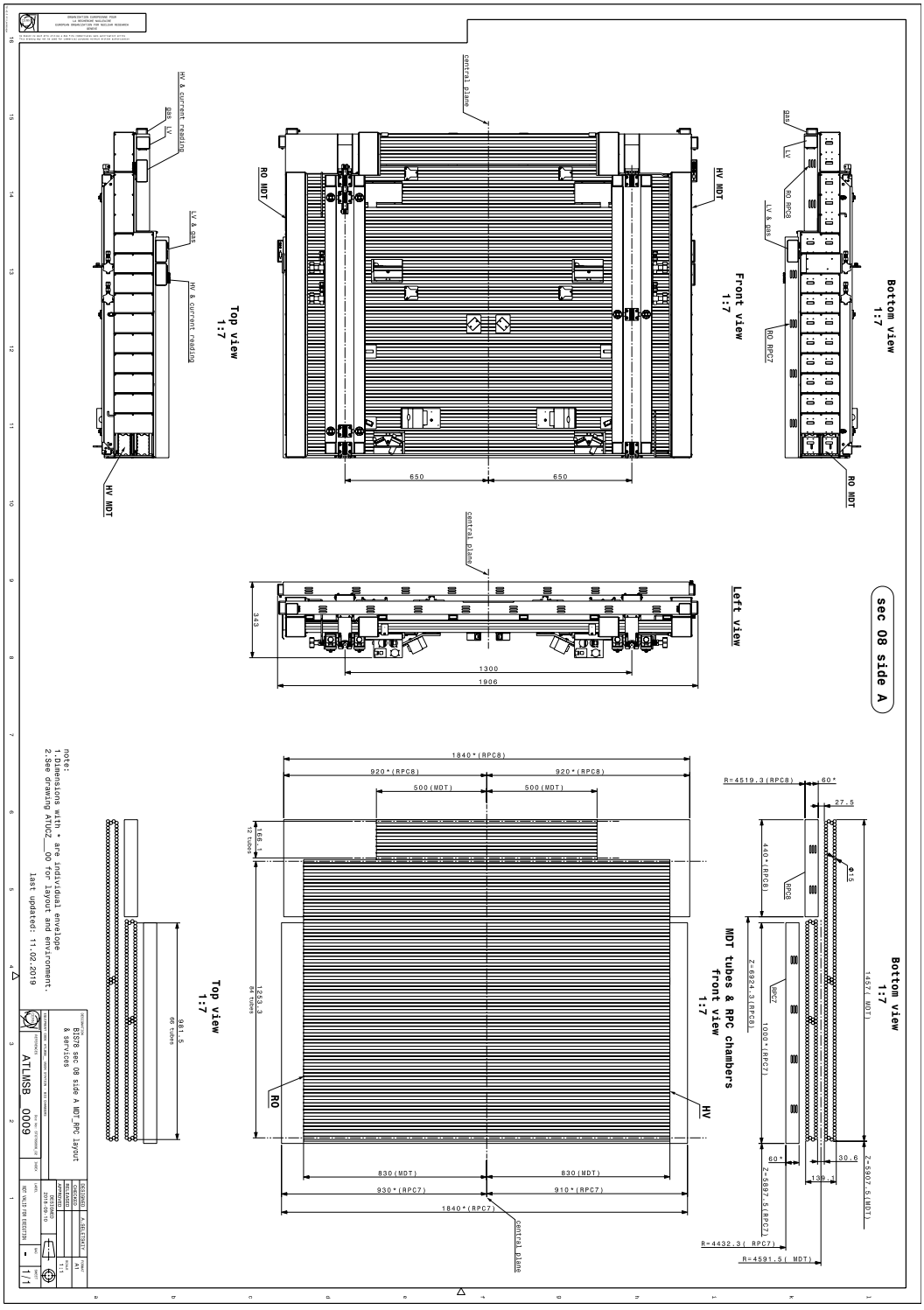

Figure C.4. RPC and sMDT design for octant 4 side A.

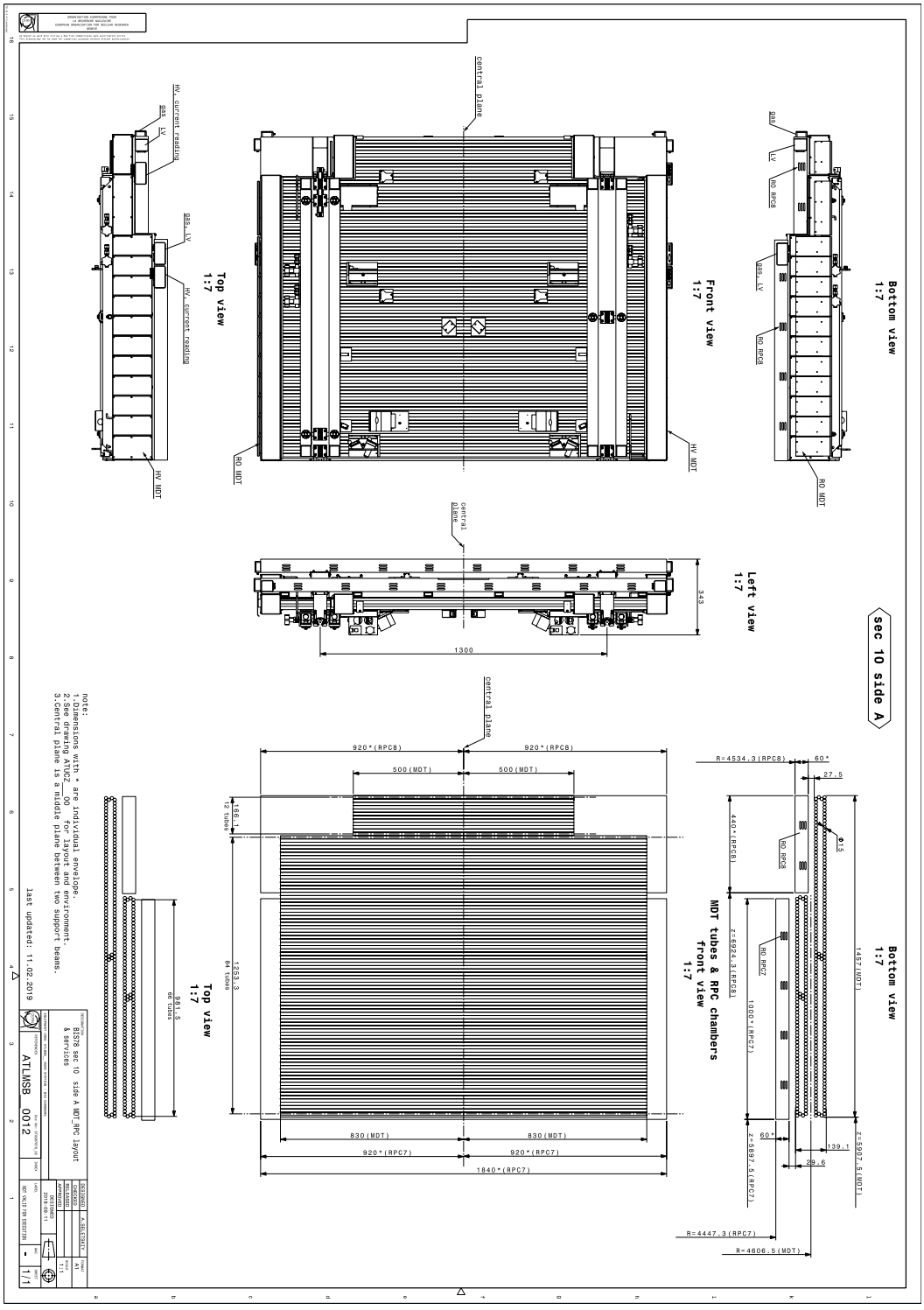

Figure C.5. RPC and sMDT design for octant 5 side A.

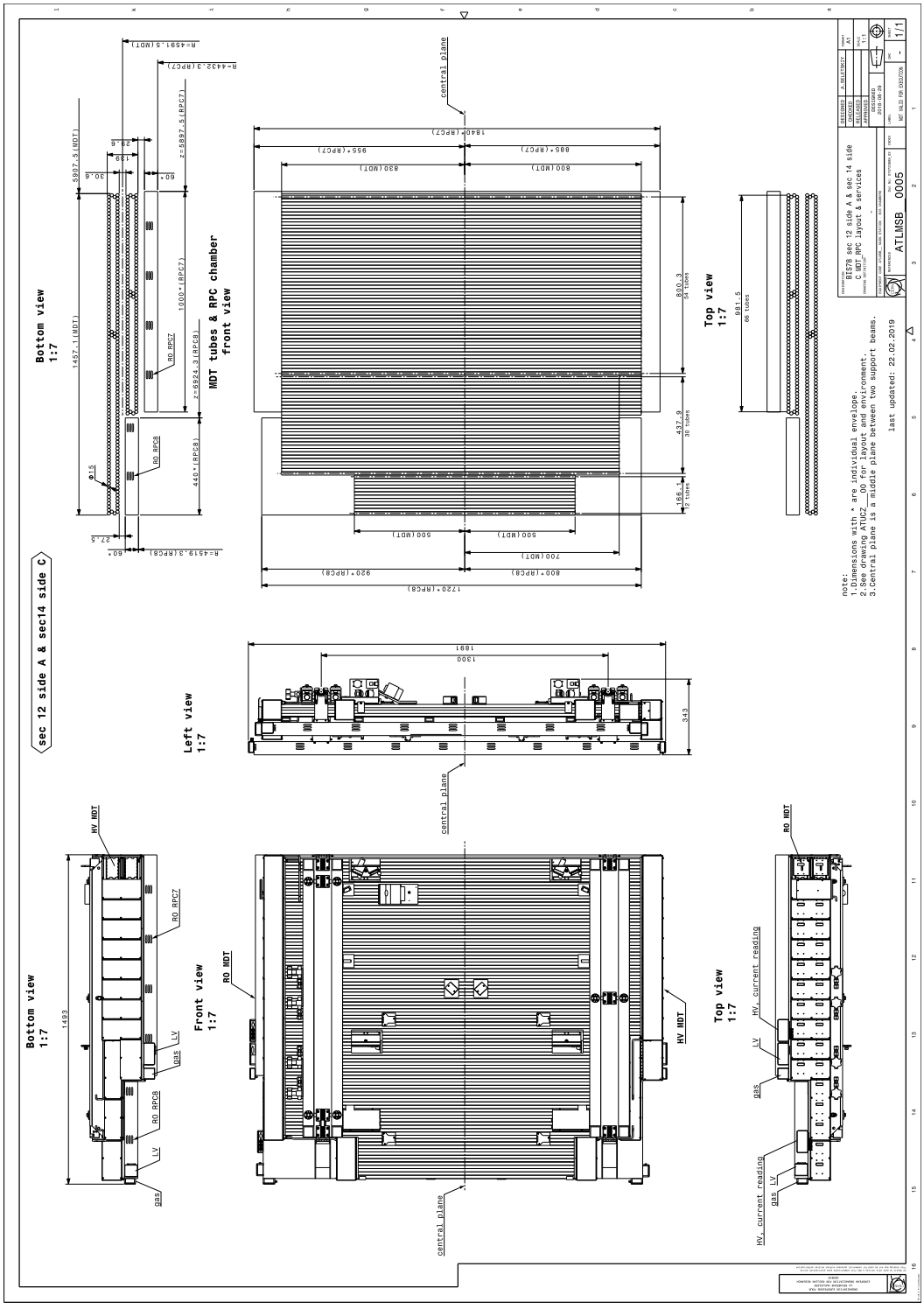

Figure C.6. RPC and sMDT design for octant 6 side A.

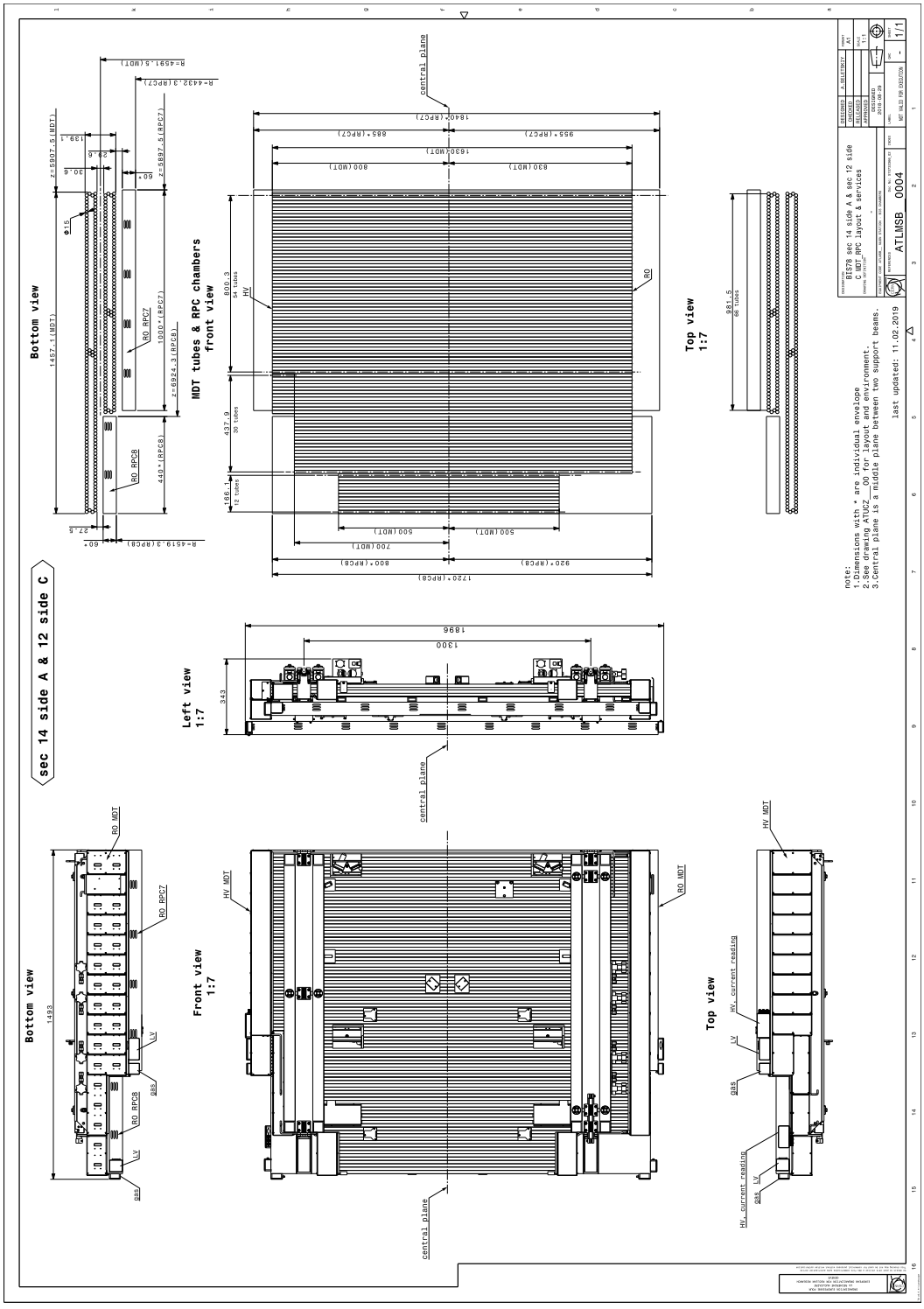

Figure C.7. RPC and sMDT design for octant 7 side A.

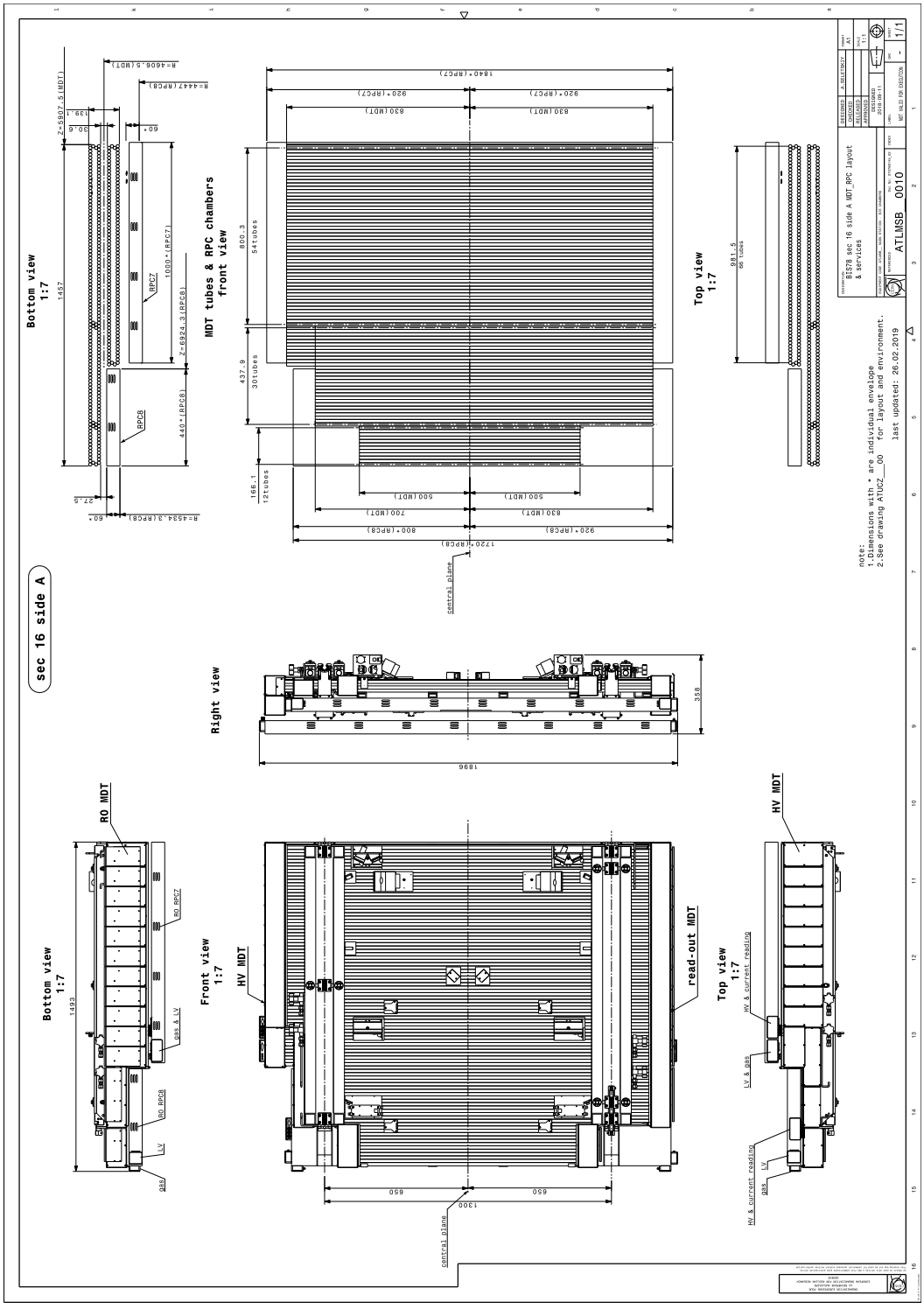

Figure C.8. RPC and sMDT design for octant 8 side A.

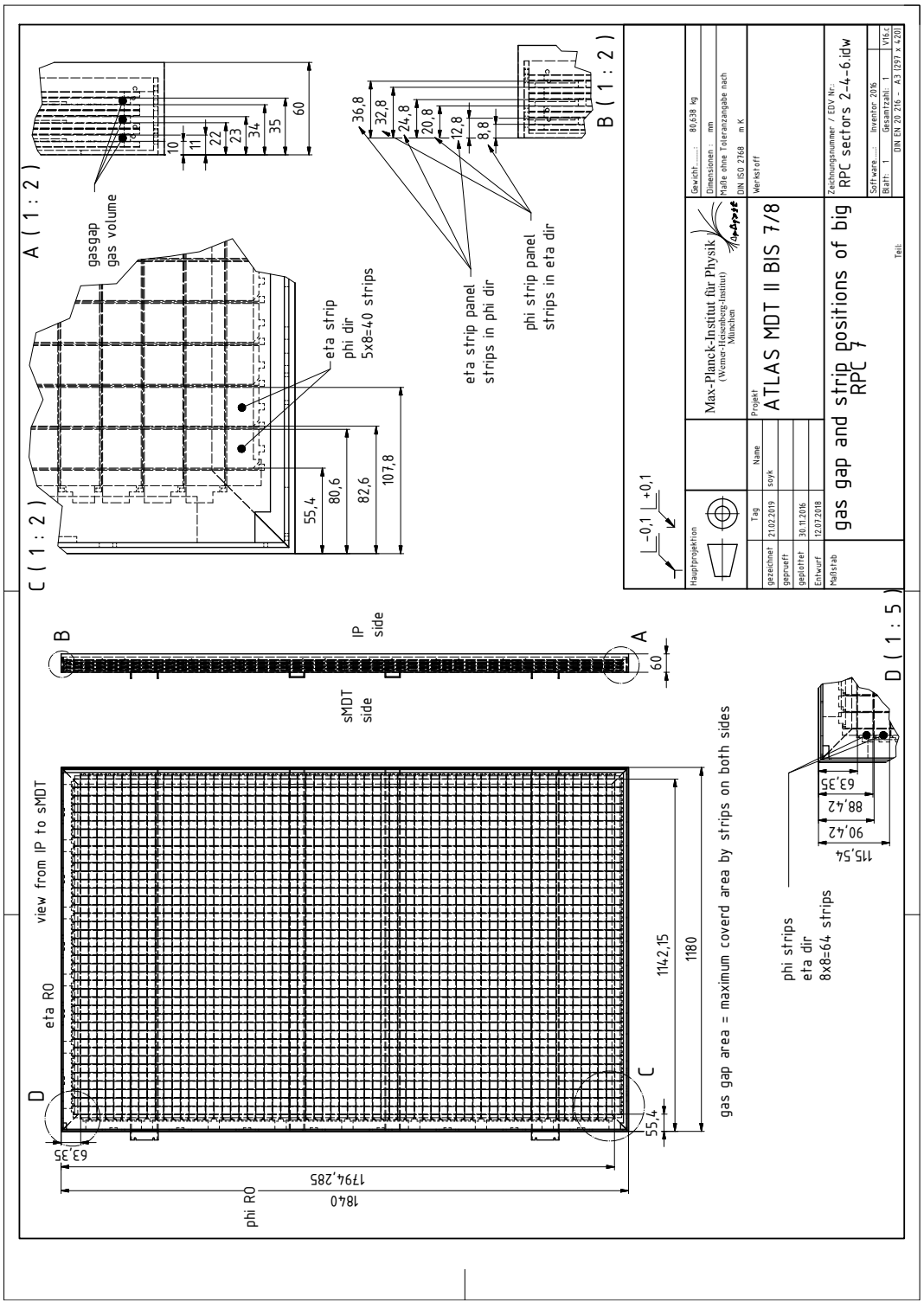

Figure C.9. Big RPC7 inner structure design.

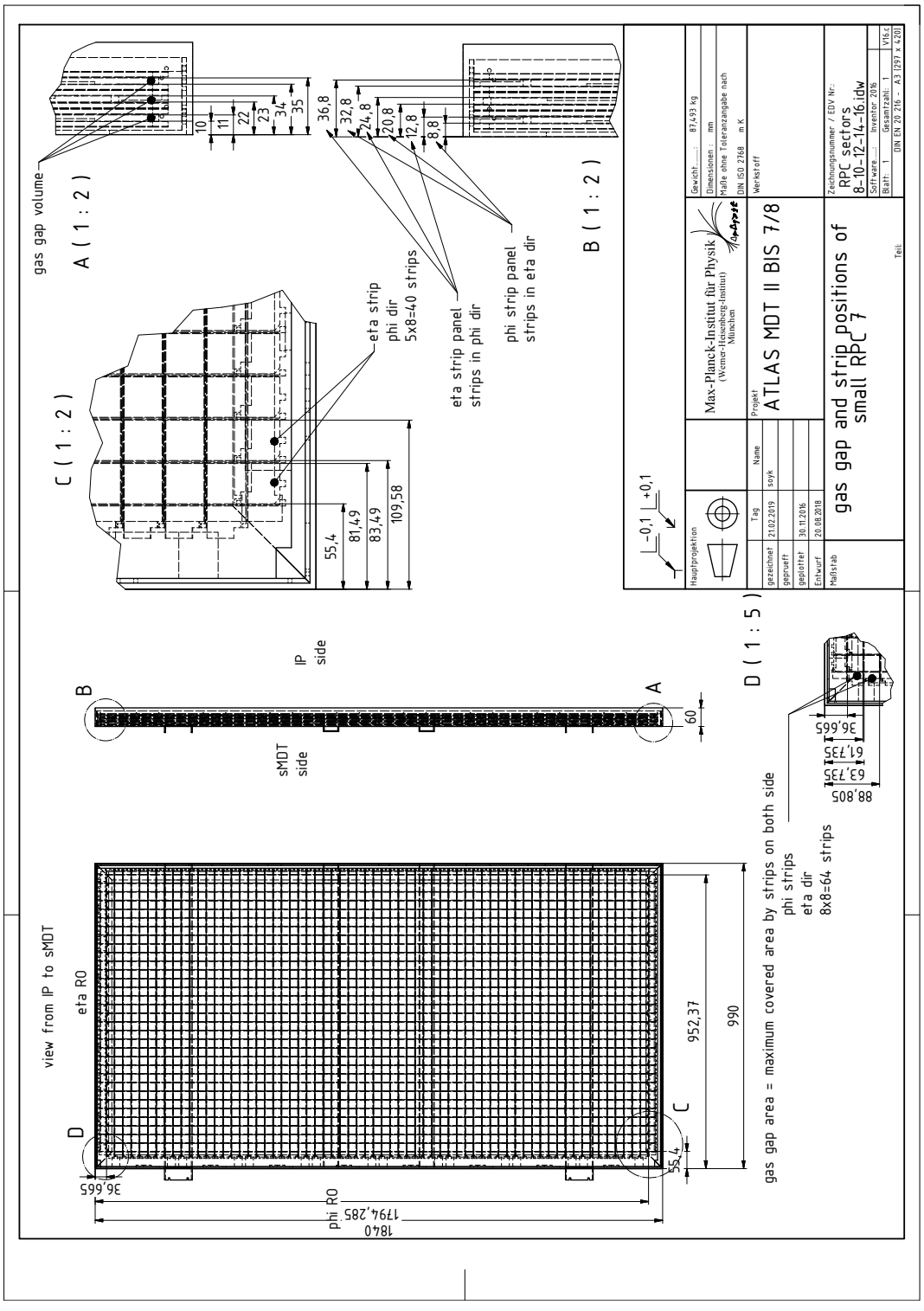

Figure C.10. Small RPC7 inner structure design.

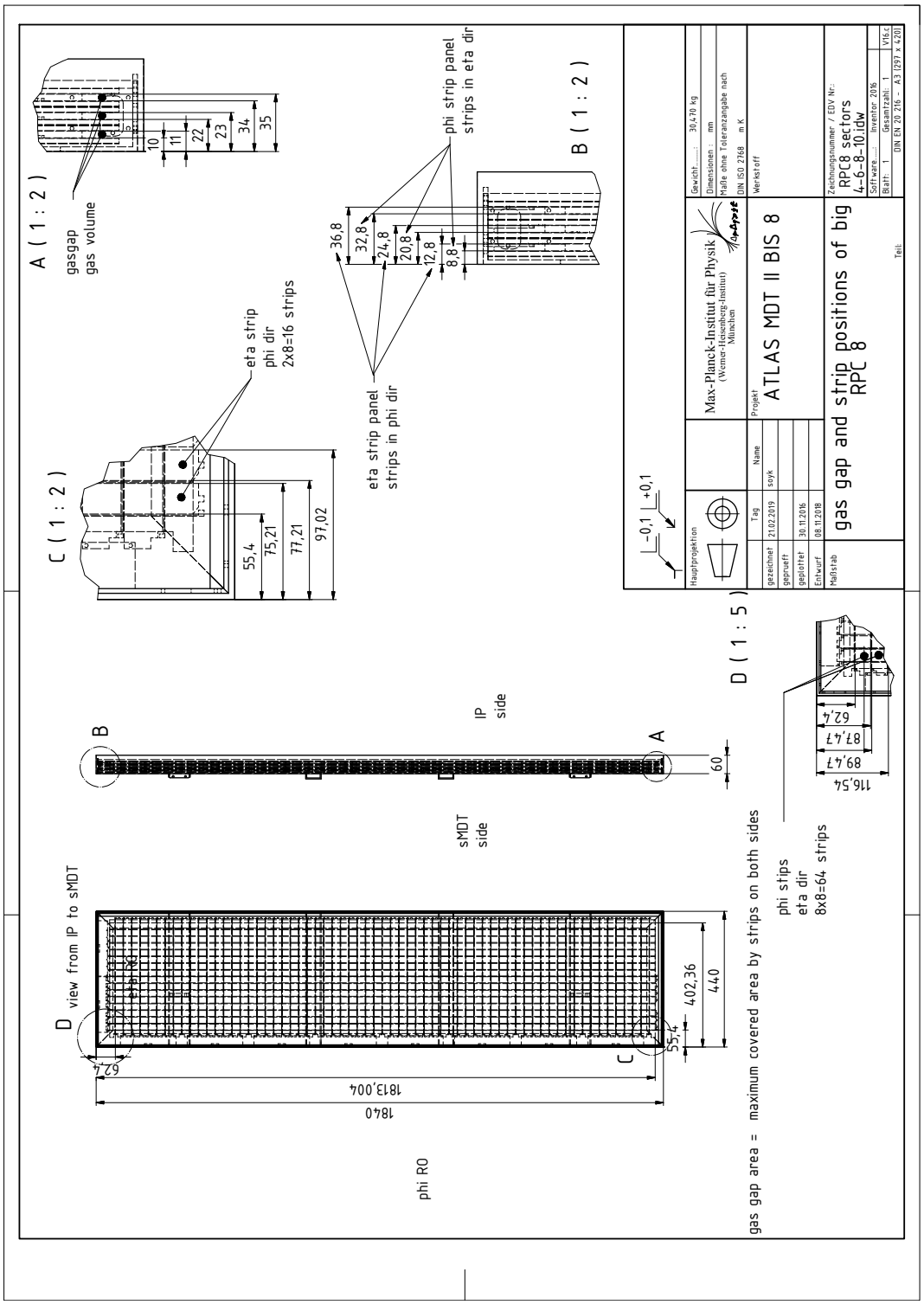

Figure C.11. Big RPC8 inner structure design.

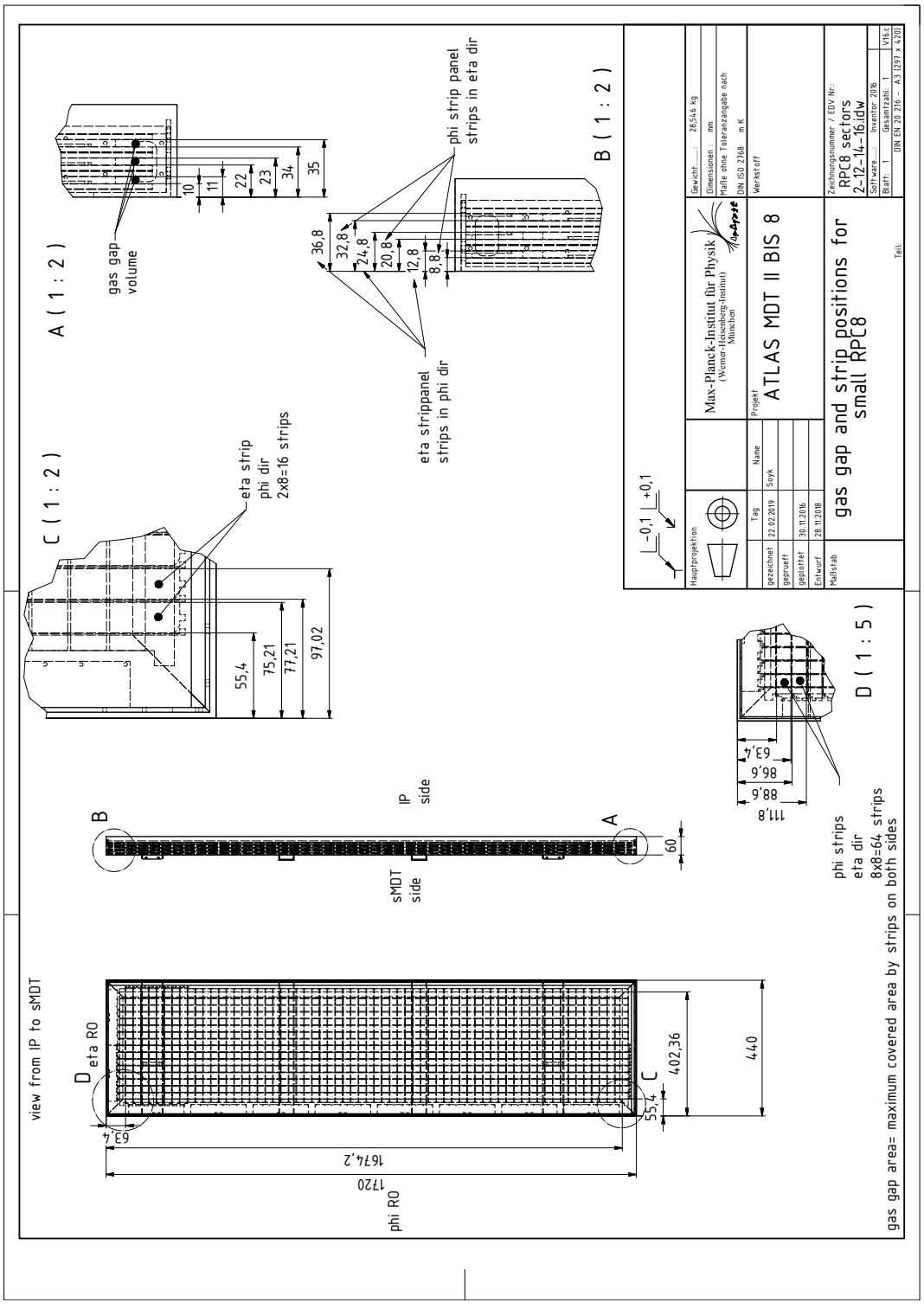

Figure C.12. Small RPC8 inner structure design.

APPENDIX D: RPC TOY MODEL GEANT4 SIMULATION PACKAGE

In order to form the simulation for RPC toy model in GEANT4 in Chapter 2, the critical parts of the codes are shown in this chapter. The main structure is dependent on the basic example B4a [2] that is found in the GEANT4.

```
/// \file B4DetectorConstruction.cc
/// \brief Implementation of the B4DetectorConstruction class
#include "B4DetectorConstruction.hh"
#include "G4Material.hh"
#include "G4NistManager.hh"
#include "G4Box.hh"
#include "G4LogicalVolume.hh"
#include "G4PVPlacement.hh"
#include "G4PVReplica.hh"
#include "G4GlobalMagFieldMessenger.hh"
#include "G4AutoDelete.hh"
#include "G4GeometryManager.hh"
#include "G4PhysicalVolumeStore.hh"
#include "G4LogicalVolumeStore.hh"
#include "G4SolidStore.hh"
#include "G4VisAttributes.hh"
#include "G4Colour.hh"
#include "G4PhysicalConstants.hh"
#include "G4SystemOfUnits.hh"

G4ThreadLocal

B4DetectorConstruction::B4DetectorConstruction()
```

```
 : G4VUserDetectorConstruction(),
   rpcPV(nullptr),
   fCheckOverlaps(true)
{
}

B4DetectorConstruction::~B4DetectorConstruction()
{
}

G4VPhysicalVolume* B4DetectorConstruction::Construct()
{
// Define materials
DefineMaterials();

// Define volumes
return DefineVolumes();
}

void B4DetectorConstruction::DefineMaterials()
{
// Lead material defined using NIST Manager
auto nistManager = G4NistManager::Instance();
nistManager->FindOrBuildMaterial("G4_Cu");


// Vacuum
new G4Material("Galactic", z=1., a=1.01*g/mole,density=
universe_mean_density,
kStateGas, 2.73*kelvin, 3.e-18*pascal);
```

```
G4VPhysicalVolume* B4DetectorConstruction::DefineVolumes()
{

  //world parameters
    G4double worldWidth = 500.*cm;
    G4double worldLength = 500.*cm;
    G4double worldHeight = 500.*cm;

  //rpc parameters
    G4double width = 30.*cm;
    G4double length = 50.*cm;
    G4double thickness = 10.*mm;

  // Get materials
  auto defaultMaterial = G4Material::GetMaterial("Galactic");
  auto absorberMaterial = G4Material::GetMaterial("G4_Cu");

......

// World

  auto worldS
    = new G4Box("World",// its name
     worldWidth, worldLength, worldHeight); // its size

  auto worldLV
    = new G4LogicalVolume(
                 worldS,           // its solid
                 defaultMaterial,  // its material
                 "World");         // its name
```

```
  auto worldPV
    = new G4PVPlacement(
                  0,                  // no rotation
                  G4ThreeVector(),    // at (0,0,0)
                  worldLV,            // its logical volume
                  "World",            // its name
                  0,                  // its mother  volume
                  false,              // no boolean operation
                  0,                  // copy number
                  fCheckOverlaps);    // checking overlaps

//RPC

  auto rpcS
    = new G4Box("rpc", // its name
         width, length, thickness); // its size

  auto rpcLV
    = new G4LogicalVolume(
                  rpcS,             // its solid
                  absorberMaterial,  // its material
                  "rpc");           // its name
  rpcPV
       = new G4PVPlacement(
                  0,
                  G4ThreeVector(),  // at (0,0,0)
                  rpcLV,            // its logical volume
                  "rpc",            // its name
                  worldLV,            // its mother
                  false,             //
```

```
                0,          // number of replica
                fCheckOverlaps);  // witdth of replica

}

......


/// \file B4PrimaryGeneratorAction.cc
/// \brief Implementation of the
B4PrimaryGeneratorAction class

#include "B4PrimaryGeneratorAction.hh"

#include "G4RunManager.hh"
#include "G4LogicalVolumeStore.hh"
#include "G4LogicalVolume.hh"
#include "G4Box.hh"
#include "G4Event.hh"
#include "G4ParticleGun.hh"
#include "G4ParticleTable.hh"
#include "G4ParticleDefinition.hh"
#include "G4SystemOfUnits.hh"
#include "Randomize.hh"


B4PrimaryGeneratorAction::B4PrimaryGeneratorAction()
 : G4VUserPrimaryGeneratorAction(),
   fParticleGun(nullptr)
{
  G4int nofParticles = 1;
```

```
  fParticleGun = new G4ParticleGun(nofParticles);

  // default particle kinematic
  //
auto particleDefinition
= G4ParticleTable::GetParticleTable()->FindParticle("mu+");
fParticleGun->SetParticleDefinition(particleDefinition);
fParticleGun->
SetParticleMomentumDirection(G4ThreeVector(0.,0.,1.));
fParticleGun->SetParticleEnergy(300.*MeV);
}
......

// Set gun position
G4double pos=-11.*cm;
fParticleGun
->SetParticlePosition(G4ThreeVector(0., 0., pos));

fParticleGun->GeneratePrimaryVertex(anEvent);
}


/// \file B4RunAction.cc
/// \brief Implementation of the B4RunAction class

#include "B4RunAction.hh"
#include "B4Analysis.hh"

#include "G4Run.hh"
#include "G4RunManager.hh"
#include "G4UnitsTable.hh"
```

```
#include "G4SystemOfUnits.hh"

B4RunAction::B4RunAction()
 : G4UserRunAction()
{
// set printing event number per each event
G4RunManager::GetRunManager()->SetPrintProgress(1);

// Create analysis manager
// The choice of analysis technology
 is done via selection of a namespace
// in B4Analysis.hh
auto analysisManager = G4AnalysisManager::Instance();
G4cout << "Using "<< analysisManager->GetType() << G4endl;

// Create directories
//analysisManager->SetHistoDirectoryName("histograms");
//analysisManager->SetNtupleDirectoryName("ntuple");
analysisManager->SetVerboseLevel(1);
analysisManager->SetNtupleMerging(true);
// Note: merging ntuples is available only with Root output

  // Book histograms, ntuple
  //

// Creating histograms
analysisManager->CreateH1("Erpc",
"Edep in rpc",300, 0.,300*MeV);
analysisManager->CreateH1("Lrpc",
"trackL in rpc",100,0.,10*cm);
```

```
// Creating ntuple

analysisManager->CreateNtuple("B4", "Edep and TrackL");
analysisManager->CreateNtupleDColumn("Erpc");
analysisManager->CreateNtupleDColumn("Lrpc");
analysisManager->FinishNtuple();
}


B4RunAction::~B4RunAction()
{
  delete G4AnalysisManager::Instance();
}

void B4RunAction::BeginOfRunAction(const G4Run* /*run*/)
{
//inform the runManager to save random number seed
//G4RunManager::GetRunManager()
->SetRandomNumberStore(true);

// Get analysis manager
auto analysisManager = G4AnalysisManager::Instance();

// Open an output file
//
G4String fileName = "B4";
analysisManager->OpenFile(fileName);
}
.....

}
```

```
// save histograms & ntuple
//
analysisManager->Write();
analysisManager->CloseFile();
}


// \file B4aEventAction.cc
// \brief Implementation of
the B4aEventAction class

#include "B4aEventAction.hh"
#include "B4RunAction.hh"
#include "B4Analysis.hh"

#include "G4RunManager.hh"
#include "G4Event.hh"
#include "G4UnitsTable.hh"

#include "Randomize.hh"
#include <iomanip>

B4aEventAction::B4aEventAction()
 : G4UserEventAction(),
   fEnergyrpc(0.),
   fTrackLrpc(0.)

{}

B4aEventAction::~B4aEventAction()
```

```
{}

void B4aEventAction::BeginOfEventAction
(const G4Event* /*event*/)
{
  // initialisation per event
  fEnergyrpc = 0.;
  fTrackLrpc = 0.;

}

void B4aEventAction::EndOfEventAction
(const G4Event* event)
{
// Accumulate statistics

// get analysis manager
auto analysisManager = G4AnalysisManager::Instance();

// fill histograms
analysisManager->FillH1(0, fEnergyrpc);
analysisManager->FillH1(1, fTrackLrpc);


// fill ntuple
analysisManager->FillNtupleDColumn(0, fEnergyrpc);
analysisManager->FillNtupleDColumn(1, fTrackLrpc);
analysisManager->AddNtupleRow();
 ....
  }
}
```